MECHANISMS OF METASTATIC LATENCY AND OUTGROWTH IN HER2+ BREAST CANCER

by

Danilo Reynaldo Galindez Macalinao

A Dissertation

Presented to the Faculty of the Louis V. Gerstner, Jr.

Graduate School of Biomedical Sciences,

Memorial Sloan Kettering Cancer Center

In Partial Fulfillment of the Requirements

for the Degree of Doctor of Philosophy

New York, New York

December, 2017

_____ _____

Joan Massagué, PhD Date

Dissertation Mentor

Abstract

Metastasis accounts for a majority of mortalities in cancer, and can frequently develop many years after the initial diagnosis and treatment of the primary tumor. Patients with HER2+ disease, who have experienced remarkable gains in disease management owing to HER2-targeted therapies, are susceptible to developing metastases after a protracted period of being disease-free. Notably, progression in HER2+ breast cancer is frequently seen in the brain, with up to 50% of patients developing CNS metastases. We derived HER2+ latency competent cancer (LCC) cells and brain-tropic metastatic (BrM) cells and defined mechanisms that shed light on metastatic latency and brain metastatic outgrowth. LCC cells are stem-like, express Sox transcription factors, and actively enforce quiescence to evade immune-mediated clearance by NK cells. BrM cells with the competency to initiate brain metastatic outgrowth secrete extracellular matrix component factors upon entry into the brain, providing them a niche that promotes their outgrowth and mediates the exclusion of reactive microglia. Collectively, these studies help elucidate how HER2 cancer cells might be able to stay latent for long periods of time in host organs, and the traits required by these cells upon exit from latency to initiate brain metastatic outgrowth.

Acknowledgements

My first round of thanks is owed to my thesis mentor, Dr. Joan Massagué, who has been instrumental to my growth as a scientist these past six years. To have been able to think about and approach science with you these past few years has been an absolute honor and privilege. You gave me the freedom to think critically and independently about my project, challenged me to go deeper into my work, and provided direction and guidance when the project seemed to hit a dead-end. I am thankful for these formative years in your lab and for your friendship.

Second, I am thankful for the support of my fellow lab mates – you are all an outstanding group of scientists, and I was so lucky to have been able to learn from all of you. Your drive, dedication and passion for science was infectious! In particular, I thank Dr. Srinivas Malladi, now with his own lab at UT Southwestern, for his mentorship during my first few years in the lab – working with you on the metastatic latency project was an important learning experience for me. I look forward to reading about your future accomplishments!

Third, I would like to thank my thesis committee – Dr. Richard White and Dr. Robert Benezra, for being with me on this journey these past few years, and for Dr. Luis Parada and Dr. Nancy Du, who join my examining committee as Chair and external adviser, respectively. I thank you for your time and advice throughout these years.

Fourth, I thank the Gerstner Sloan Kettering Graduate School community – staff and students past and present, who have molded and guided this program to be what it is today. I am lucky to have found a home at GSK.

Fifth, I cannot thank enough the friends I've made outside of the lab, who have kept me grounded while here in New York City! In a special way, my community of friends at the Church of St. Paul the Apostle, and the Paulist Fathers, have been an integral component of my experience here in New York City.

Lastly, I thank my family – for their unconditional support throughout these years. Thanks to my two siblings Laura and RG for being some of my biggest advocates. I especially thank mom and dad, Danny and Agnes, who 13 years ago let a then 17-year old high school student leave home and fly 8,500 miles away to pursue his dreams. I cannot ever thank you enough for your confidence and trust in me.

Table of Contents

Table of Figures

Chapter 1: Introduction

1.1 Breast Cancer Subtype Specification

Breast cancer remains to be the most frequently diagnosed cancer in women in the United States, with over 250,000 estimated new cases each year, and is the second deadliest cancer in women, next only to lung cancer (Siegel et al., 2017). A majority of breast cancer patients can be sub-classified based on the expression of Estrogen Receptor (ER), Progesterone Receptor (PR) and Human Epidermal growth factor Receptor 2 (HER2). The expression pattern of these receptors informs the standard-of-care regimens to use, a patient's response to treatment, and is predictive of clinical outcomes (Inwald et al., 2015; Onitilo et al., 2009). The advent of whole genome expression methodologies extends these classification criteria to reveal five molecular subtypes – basal-like (ER-, PR-, HER2-), luminal A (ER+, PR+/-, HER2-), luminal B (ER+, PR+/-, HER2+/-), HER2-enriched (ER-, PR-, HER2+), and normal-like (Perou et al., 2000; Sørlie, 2004). The existence of these intrinsic breast cancer subtypes in ductal carcinoma in situ (DCIS), the non-oblate precursor stage to invasive breast cancer, suggests that different breast cancer subtypes likely undergo different paths towards malignancy (Clark et al., 2011; Lesurf et al., 2016; Muggerud et al., 2010).

Luminal breast cancers (luminal A and luminal B) are the most frequently diagnosed of the different subtypes, and represent roughly two-thirds of all breast cancer cases (Carey et al., 2006). Almost all luminal breast cancers express estrogen receptor, and require signaling mediated through this pathway for their

growth and survival. As such, they are uniquely sensitive to hormone therapy, which acts by competing against estrogen for binding with the estrogen receptor (ex. tamoxifen), or by impeding estrogen production through the use of aromatase inhibitors (ex. letrozole) (Fisher et al., 1996; Goss et al., 2003). Prognosis for patients with early stage luminal breast cancer is relatively good, with a 5-year disease free survival of up to 90% (Goss et al., 2016).

Basal breast cancer is typically exemplified by the absence of ER, PR and HER2 expression, and is reported to occur in 10-20% of breast cancer patients. To date, no known molecular targets exist for this subtype of breast cancer, making it difficult to completely eradicate cells that have disseminated from the primary tumor site (Sørlie, 2004). While patients see a benefit from the general standard-of-care regimen for breast cancer (surgery, chemotherapy, radiation), the lack of targeted therapeutics inevitably leads to a high rate of local relapse and metastatic disease (Cleator et al., 2007).

HER2-enriched breast cancers overexpress human epidermal growth factor receptor 2 (HER2). In general, 20-30% of breast cancer patients show expression for the HER2 receptor (Roskoski, 2014). Stimulation of the proliferative and pro-survival PI3K and MAPK pathways by HER2 signaling is a main driver of cancer progression in this disease setting (Junttila et al., 2009). Targeted therapies developed against HER2 have resulted in remarkable gains in the survival of patients living with this disease (Slamon et al., 2011). There is a paucity of

treatment options for patients whose disease relapses, because the disease becomes refractory to targeted therapies, or metastasizes to a site that is particularly difficult to treat, such as the brain (Brufsky et al., 2011a). Upwards of 50% of HER2+ breast cancer patients have central nervous system metastases, making this the final frontier for this disease (Leyland-Jones, 2009).

1.2 HER2+ Breast Cancer Biology

1.2.1 ErbB/HER Receptor Signaling Pathway

The ErbB/HER family of receptor protein-tyrosine kinases is composed of four family members – HER1/EGFR, HER2/ErbB2, HER3/ErbB3, HER4/ErbB4 (Lemmon and Schlessinger, 2010). Each of these ErbB receptors are structured in a similar manner, consisting of an extracellular region, a single transmembrane spanning domain, a tyrosine kinase domain, and a C-terminal terminal region containing tyrosine residues. Whereas EGFR and HER4 have both active ligand binding domain and tyrosine kinase domain, HER2 lacks ligand binding ability, and HER3 possesses an inactive tyrosine kinase domain (Hynes and Lane, 2005). Structural studies of HER2 demonstrate that the receptor is in a constitutively active conformation (Garrett et al., 2003), making it poised for dimerization with other ErbB family members.

Ligand binding to the extracellular region induces dimerization of receptors, which allows the transactivation of tyrosine kinase domains, leading to the phosphorylation of residues on the cytoplasmic tail. Because the cytoplasmic tails of each ErbB receptor is different, it allows for the diversification of downstream

signaling pathways. Specific ErbB receptor pairs largely dictate the outcome of downstream signaling pathways (Yarden and Sliwkowski, 2001; Yarden and Pines, 2012), with the ErbB2/ErbB3 receptor pair being the strongest mediator of downstream signaling (Moasser, 2007). The phosphorylation of tyrosine residues on the cytoplasmic tail of ErbB3 is recognized by the regulatory subunit of PI3K (p85), leading to the activation of the PI3K/Akt pathway (Wilson et al., 2009). Phosphorylation of tyrosine residues on the cytoplasmic tail of ErbB2 leads to ERK1/2 MAPK pathway activation. Phosphorylated tyrosine residues on the cytoplasmic tail of ErbB2 are bound to by the adaptor proteins Grb2 or Shc, leading to the activation of the ERK1/2 MAP kinase activity. The downstream pathways activated by ErbB2/ErbB3 signaling lead to enhanced proliferation and survival of cells (Alimandi et al., 1995; Wallasch et al., 1995).

1.2.2 ErbB2 receptor function in normal development

ErbB receptors are expressed in a wide range of tissues, and are important for organismal development, as null mutation of any family member leads to embryonic lethality in mice (Roskoski, 2014; Wieduwilt and Moasser, 2008). The role of ErbB2 in cardiac development has been widely studied. ErbB2 expression is localized to cardiac myocytes in developing mouse embryos. In ErbB2-mutant mice, ventricular trabeculation is impaired, which is responsible for maintaining proper blood flow during heart morphogenesis (Lee et al., 1995). Restricted deletion of ErbB2 in cardiac tissues using Cre-lox methods revealed marked dilation of heart chambers and decreased contractility (Crone et al., 2002). ErbB2

has also been implicated in neural development. In addition to cardiac abnormalities, ErbB2 mutant mouse embryos had defects in the development of the nervous system, with impairment of trigeminal and facial motor nerve formation (Lee et al., 1995). Lastly, ErbB2 has been shown to be important for Schwann cell expansion and myelination (Garratt et al., 2000).

1.2.3 Prevalence of ErbB2 amplification and overexpression in cancer

ErbB2 was first discovered in 1985 as a novel oncogene that shared homology with the EGF receptor (Yamamoto and Semba, 2011). Amplification and overexpression of ErbB2 is prominent in breast, gastrointestinal and bladder cancers (Yarden and Pines, 2012). Its role in breast cancer is the most widely studied; 20 – 30% of breast cancer patients overexpress HER2 (Baselga and Swain, 2009). Historically aggressive, patients with HER2+ breast cancer are at greater risk for disease progression, owing to the ability of HER2 to engage potent survival and proliferation signals through PI3K and MAPK pathway activation (Yarden and Sliwkowski, 2001). Several genetically engineered mouse models have been generated to study ErbB2 breast cancer. Mice carrying an activated transgene for the rat equivalent of ErbB2, c-*neu*, driven under the transcriptional control of the mouse mammary tumor virus promoter, rapidly generated mammary tumors, suggesting the sufficiency of ErbB2 overexpression in tumorigenesis (Muller et al., 1988). These tumors are ‘addicted’ to ErbB2 expression; withdrawal of ErbB2 signaling in a model where ErbB2 expression is conditionally activated resulted in the regression of already established tumors (Moody et al., 2002). ErbB2 overexpression is also prevalent in advanced gastric cancers and predictive

of poorer survival, with approximately 20% of patients showing positivity for HER2 expression (Gravalos and Jimeno, 2008). The use of next generation sequencing technologies has highlighted the presence of ErbB2 activating mutations in a spectrum of cancers – most notably lung cancer, which has a relative paucity of HER2 amplification (Peters and Zimmermann, 2014).

1.2.4 Targeted Therapies against HER2

The heavy reliance of HER2+ breast cancer on signaling through the HER2 receptor signaling cascade has made targeting HER2 a potent strategy in stunting the growth of cancer cells. Over the last few decades, several different targeted therapies against HER2 have become part of the standard-of-care regimen for patients with HER2 disease.

In 1989, the lab of Axel Ullrich demonstrated that a monoclonal antibody developed against the extracellular domain of the HER2 receptor potently inhibited proliferation of HER2-expressing breast cancer cells *in vitro* (Hudziak et al., 1989). This served as basis for the development of the recombinant humanized monoclonal antibody Herceptin (trastuzumab), which showed remarkable ability to inhibit orthotopic tumor growth of HER2+ human cancer cell lines in athymic nude mice (Baselga et al., 1998). Herceptin binds to domain IV of the extracellular region of the HER2 receptor, resulting in the downregulation of proliferative AKT signaling. Several mechanisms of action exist for Herceptin, each contributing to its remarkable anti-tumorigenic effect. Herceptin has been shown to prevent the promiscuous dimerization of ligand-independent HER2-HER3 complexes,

effectively blunting AKT activation (Junttila et al., 2009). Furthermore, an increasing body of literature supports the contribution of the immune compartment in eliciting the anti-tumorigenic properties of monoclonal antibodies. Antibody-dependent cell-mediated cytotoxicity has been demonstrated in preclinical models of HER2+ breast cancer, where cell lines resistant to Herceptin *in vitro* are sensitive when implanted *in vivo* (Barok et al., 2007; Kute et al., 2009). More recently, antibody-drug conjugates have been demonstrated to be efficacious, with the commercialization of the fusion trastuzumab-DM1, where an anti-microtubule agent (DM1) is fused to the HER2 monoclonal antibody. Internalization of the antibody-drug conjugate directly delivers the chemotherapy agent directly to cells overexpressing HER2 (Austin et al., 2004). In addition to trastuzumab, other antibody modalities have been developed to complement the arsenal of HER2 targeted therapies. One such example, pertuzumab, binds to domain II of the extracellular region, sterically preventing HER2 dimerization (Capelan et al., 2013).

Other strategies have also been developed that target other regions of HER2 – small molecule inhibitors target the cytoplasmic tyrosine kinase domain which mitigates the critical phosphorylation events that lead to downstream signaling. These small molecules preferentially bind to the ATP-binding site, preventing the activation of the tyrosine kinase and subsequent phosphorylation of the C-terminal tails. As such, this strategy prevents the recruitment of PI3K and MAPK components to the C-terminal tails, leading to the attenuation of pro-survival and

growth pathways mediated by ErbB signaling. On this front, Tykerb (lapatinib) has been demonstrated to be a powerful TKI against both HER2 and EGFR, and is currently indicated for use in advanced stage HER2+ breast cancer in conjunction with the chemotherapy drug capecitabine (Geyer et al., 2006).

1.3 Metastatic Latency and Outbreak

1.3.1 The Metastatic Cascade

A majority of cancer patients who die succumb to their disease because of metastases, the colonization of distant organs away from the primary tumor site. The process of metastatic colonization is extremely inefficient, with studies suggesting that less than 1% of disseminated tumor cells are capable of forming metastatic foci (Fidler, 1970; Luzzi et al., 1998). Metastasis is a multi-faceted cascade, in order to succesfully colonize distant organ sites, cancer cells must acquire traits and functions that make them successful at each step of the process (Gupta and Massagué, 2006). There are functions required for departure from the primary tumor site and intravasation into the vasculature, survival in circulation, and extravasation into a distant organ site (Obenauf and Massagué, 2015).

Arrival at a distant organ site is particularly hostile, as this microenvironment is completely new and foreign to cancer cells that may want to colonize it. Although a majority of cells die, those that survive the journey likely sit in a latent state for protracted periods of time to avoid demise. Clinical observations support the notion that cells that leave the primary tumor are capable of initiating metastatic outgrowth months to years after initial treatment (Demicheli et al., 2005). Ultimately, overt

outgrowth requires the ability of cancer cells to integrate signals in its new microenvironment to elicit their growth. Because organ sites are all different, each will likely possess a unique set of barriers that cancer cells must overcome to become successful at colonization.

1.3.2 Latency Phase of Metastasis

Our ability to successfully treat primary tumors has led to an increase in favorable prognosis for cancer patients (Siegel et al., 2017). Accompanying this, however, is the relapse of cancer patients with metastatic disease after successful treatment of their primary cancer, sometimes long after the completion of their treatment regimen (Meng et al., 2004). There is a growing body of literature examining the mechanisms that cancer cells engage to remain latent in host tissues.

A prevailing model for how dormant cancer cells maintain their inactive state is through the action of inhibitory signals derived from the microenvironment. In a model for head and neck squamous cell carcinoma (HNSCC), TGFβ2 signaling derived from the bone marrow serves as a dormancy cue for these cells, activating p38 in cancer cells, which in turn allows for the downregulation of CDK4 and maintenance of the dormancy state (Bragado et al., 2013). Similarly, bone morphogenetic protein 7 (BMP7), a member of the TGFβ family, has been shown to induce dormancy of prostate cancer cells that home to the bone, by similar mechanisms of p38 activation (Kobayashi et al., 2011). The microvasculature has also been implicated in promoting quiescence, with endothelial-cell derived

thrombospondin-1 as being able to sustain the dormancy of breast cancer cells (Ghajar et al., 2013).

The role of the immune system in the latency phase is also coming into vogue and being appreciated, especially with the renewed interest in immune-modulating therapies. The cancer immune-editing concept describes three distinct phases that describe the interaction of cancer cells with the immune system – elimination, equilibrium, and escape (Schreiber et al., 2011). In the elimination phase, the immune system is competent at recognizing and killing cancer cells, resulting in successful and complete eradication of malignant cells. Cancer cells that successfully circumvent elimination enter the equilibrium phase – whereby overt cancer cell outgrowth is kept in check by immunity, but not completely eliminated. Mice treated with a low-dose carcinogen to induce carcinogenesis harbored undetectable cancer cells, which were only made apparent when the immune system was ablated by monoclonal antibodies (Koebel et al., 2007). This notion is reinforced in case reports of donor-derived cancer being transferred from the organ donor to an immunocompromised organ transplant recipient (MacKie et al., 2003). In one case report, kidneys from a cadaver donor were transplanted into two immunocompromised recipients, who both developed melanoma shortly after transplant, only to find out that 16 years prior to the harvest of the kidneys, the donor had previously been diagnosed and treated successfully for melanoma (MacKie et al., 2003). Cancer cells that successfully enter latency must be able to evade immune mediated clearance.

How cancer cells re-awaken from immune-mediated latency remains poorly understood. Given the probable role of the immune system in mediating the latent phase, cancer cells must find ways of evading immune–mediated clearance in order to exit latency. In addition, cells that exit latency must come equipped to integrate the signals in their microenvironment to allow for their survival and growth. The acquisition of these traits seem unlikely if latent cancer cells were kept quiescent indefinitely in organ sites, suggesting that our model of the latent phase of metastasis needs to be refined to account for the evolution necessary for cells to acquire such traits.

1.3.3 Metastatic Outgrowth Phase in the Brain

In the context of HER2+ breast cancer, targeted therapies against HER2 have resulted in remarkable control of disease progression (Swain et al., 2015). Despite this, patients are still at risk of metastasis, even after years of being disease-free. In the post-targeted therapy era, the development of central nervous system metastases has been a particular area of unmet need in this disease setting, with up to 50% of HER2+ patients developing metastases in the CNS during the course of their lifetime (Leyland-Jones, 2009; Lin and Winer, 2007). Like many tumors in the brain, no good treatment modality exists when malignant cells reach this site (Brufsky et al., 2011b). The prognosis is dismal for patients with metastatic disease

to the brain, with median survival time between 3 months to 2 years (Azim and Azim, 2012).

Numerous mediators of different steps in brain metastasis have been identified in triple negative and lung cancer models (Boire et al., 2017; Bos et al., 2009; Sevenich et al., 2014; Valiente et al., 2014). The blood-brain barrier makes it particularly difficult for foreign agents, including cancer cells, from accessing the brain parenchyma, requiring specialized processes to facilitate this. ST6GALNAC5, a brain sialyltransferase, helps promote cancer cell adhesion to brain endothelial cells and their traversing of the blood-brain barrier (BBB) (Bos et al., 2009). Cathepsin S has also been shown to be important in migrating through the BBB via cleavage of the junctional adhesion molecule (JAM-B) (Sevenich et al., 2014). Upon successful extravasation, metastatic cancer cells must be able to interact with the resident cell types in the brain. Breast and lung cancer cells engage the cell adhesion molecule L1CAM for vascular cooption, and expression of serpins to neutralize astrocyte-induced cell death (Valiente et al., 2014). In the end, cancer cells ultimately subvert these stromal components for their advantage, making once anti-metastatic stromal cells into cooperators in metastasis promotion. Gap junction formation with astrocytes promotes brain metastasis through enhancement of STAT1 and NF-kB signaling (Chen et al., 2016).

There is a dearth of mechanistic understanding of brain metastasis in the context of HER2+ disease. The rising incidence of brain metastasis in this disease

setting makes it an important area of investigation. This thesis aims to shed light on aspects of metastatic latency and metastatic outgrowth from HER2+ breast cancer.

Chapter 2: Materials and Methods

2.1 Molecular and Cell Biology

2.1.1. Cell Lines and Maintenance

MDA-MB-231, MMTV-Erbb2, and JIMT-1 cell lines were cultured in Dulbecco's Modified Eagle's (DME) High Glucose (HG) media (MSKCC Media Core), supplemented with 10% Fetal Bovine Serum (FBS) (Sigma Aldrich Cat: F2442), 2mM L-Glutamine (Glu) (Thermo Fisher Scientific Cat: 25030081), 100 IU/ml Penicillin/Streptomycin (P/S) (Thermo Fisher Scientific Cat: 15140122), and 1ug/ml Ampothericin B (ampoB) (Gemini Bio-Products Cat: 400-104). HCC1954 was maintained in Roswell Park Memorial Institute (RPMI) media, supplemented with 10% FBS, 2mM Glu, 100 IU/ml P/S, and 1 ug/ml ampoB. We defined mitogen rich media (MRM) as media containing full 10% FBS supplement, and mitogen low media (MLM) as media containing 2% or 0.2% FBS supplement. Cells were maintained in 5% CO_2 at 37º C, and fed every 2-3 days.

2.1.2 Gene Expression Analysis by quantitative real-time PCR (qRT-PCR)

Cells grown to approximately 80% confluence on a 10cm plate were harvested for whole RNA using the PrepEase RNA Spin Kit (Affymetrix) according to the manufacturer's instructions. Total extracted RNA was quantified using a NanoDrop (Thermo Fisher Scientific). 1ug of total RNA was used for cDNA synthesis using the Transcriptor First Strand cDNA synthesis kit (Roche Cat: 04379012001) using random hexamer primers. A ViiA7 Real-Time PCR system (Life Technologies) was used for quantitative PCR. The following Taqman primers were used in these studies: SOX2, SOX9, COL4A1, TNC, and DKK1. B2M or ACTB gene were used

as reference controls to calculate relative gene expression. We employed the standard protocol for comparative relative expression using Taqman primers, using the following thermocycler parameters – hold 50º C for 2 minutes, 95º C for 10 minutes, and 40 cycles of 95º C for 15 seconds, and 60º C for 1 minute.

2.1.3 Immunoblotting

Cells cultured on a 10cm plate in experimental culture conditions (MRM or MLM) for 2-3 days were washed with ice-cold 1X Phosphate Buffered Saline (PBS, Sigma Aldrich Cat: P4417), and directly lysed using RIPA cell lysis buffer (CST Cat: 9806) supplemented with protease (cOmplete mini tablet, Roche Cat: 11836153001) and phosphatase (Halt Phosphatase Inhibitor Cocktail, Thermo Fisher Scientific Cat: 78427) inhibitors. Samples were prepared using 4X NuPage LDS sample buffer (Thermo Fisher Scientific Cat: NP00007), 1/10 NuPage sample reducing agent (Thermo Fisher Scientific Cat: NP0004), in water. Samples were heated to 70º C in a heat block for 10 minutes, cooled on ice, and loaded onto a NuPage NOVEX 4-12% Bis-Tris Gel (Thermo Fisher Scientific Cat: NP0335). Proteins were separated in 1X MOPS buffer (Thermo Fisher Scientific Cat: NP0001) at constant 120-140V. Separated proteins were transferred onto nitrocellulose membrane (Bio-Rad Cat: 1620115) by running in 1X NuPAGE Transfer Buffer (Thermo Fisher Scientific Cat: NP0006) for 1.5 hours at 0.3A constant while on ice. Transfer was assessed by Ponceau stain.

Nitrocellulose membranes were blocked for one hour in Odyssey Blocking Buffer (Li-Cor Cat: 927-50000) and 1X TBS at 1:1 dilution (blocking buffer), and

immunoblotted overnight on a rocker platform at 4º C with primary antibodies diluted in blocking buffer supplemented with 0.01% Tween-20. The following primary antibodies were used at 1:1000: Sox2 (CST Cat: 3579S), Sox9 (CST Cat: 82630S), p-p38 (CST Cat: 4511), p38 (CST Cat: 8690), ERK (CST Cat: 4695), p-ERK (CST Cat: 4370). We used beta-tubulin (Sigma Aldrich Cat: T8328) at 1:10,000 as our loading control. Membranes were washed 4x in TBS-T for 5 minutes each at room temperature, and immunoblotted with near-infrared secondary antibodies at 1:20,000 (Li-Cor) for 1 hour at room temperature. Membranes were washed 4x with TBS-T, and then 2x with TBS to remove residual Tween-20. We imaged our blots on an Odyssey Imager (Li-Cor).

2.1. Cell Proliferation and Viability Assays

Cancer cells were seeded in 96-well tissue culture treated plates in 200ul of culture media. At indicated time points, 100ul of media was removed and replaced with 100ul CellTiter-Glo (CTG) (Promega Cat: G7572). Cells were allowed to incubate in CTG for at least 5 minutes at 37º C, after which 180ul was transferred onto white solid opaque 96-well plates. Luminescence was measured using a Synergy H1 hybrid multi-mode plate reader (BioTek).

2.1. shRNA knockdown of target genes

Knockdown HCC1954 lines were generated using the optimized “miR-E” backbone vector. The DSIR algorithm was previously used to predict candidate shRNA hairpins (Fellmann et al., 2013; Vert et al., 2006). We followed the protocol as previously described (Fellmann et al., 2013). Briefly, 97mer oligonucleotides

bearing candidate shRNA hairpins were synthesized (IDT DNA) and cloned into the lentiviral SGEN (pRRL) vector using an EcoRI/XhoI approach. *Stbl3* competent *E. coli* (Thermo Fisher Scientific Cat: C737303) were transformed, and clones were picked and sequenced.

Gene	97mer oligo sequence
SOX9.2234	TGCTGTTGACAGTGAGCGCTCGTGTGATCAGTGTGCTAAATAGTGAAGCCACAGAT GTATTTAGCACACTGATCACACGATTGCCTACTGCCTCGGA
SOX9.2532	TGCTGTTGACAGTGAGCGCTCCTGTTGTATTAACATTTAATAGTGAAGCCACAGAT GTATTAAATGTTAATACAACAGGATTGCCTACTGCCTCGGA
TNC.3039	TGCTGTTGACAGTGAGCGACAGAGGTGACATGTCAAGCAATAGTGAAGCCACAGAT GTATTGCTTGACATGTCACCTCTGCTGCCTACTGCCTCGGA
TNC.3164	TGCTGTTGACAGTGAGCGACAGCTATTGACAGTTACAGAATAGTGAAGCCACAGAT GTATTCTGTAACTGTCAATAGCTGCTGCCTACTGCCTCGGA
DKK1.1640	TGCTGTTGACAGTGAGCGCCAGAGAAAAGACAGTGTCTAATAGTGAAGCCACAGAT GTATTAGACACTGTCTTTTCTCTGATGCCTACTGCCTCGGA
COL4A1.848	TGCTGTTGACAGTGAGCGCCCAGGACAAGCTCAAGTTCAATAGTGAAGCCACAGAT GTATTGAACTTGAGCTTGTCCTGGTTGCCTACTGCCTCGGA
COL4A1.986	TGCTGTTGACAGTGAGCGCCCCGGAAAAGATGGTGACAAATAGTGAAGCCACAGAT GTATTTGTCACCATCTTTTCCGGGTTGCCTACTGCCTCGGA

To generate lentiviral viral particles for infection, we seeded 293T cells in a 10cm plate to 70% confluency in transfection media (DME HG supplemented with 10% FBS, 1% Sodium Pyruvate, 1% L-Glutamine). In a polystyrene tube, 80ul lipofectamine 2000 (Thermo Fisher Scientific Cat: 11668019) was incubated together with packaging and targeting vectors (pmd2g at 2.46 ug, pspax2 at 6.56 ug, SGEN at 7.38 ug) in 2ml of Opti-MEM media for 25 minutes to generate liposomal particles. Liposome-containing media was pipetted onto 293T cells to allow for transfection. Viral-particle containing media was collected at the 48hr and 72hr time point, and concentrated using Lenti-X Concentrator (Clontech Cat: 631231) according to the manufacturer's instructions.

Target cells were seeded overnight at a density of 1.25 x 10^5 cells on a 6-well plate, and infected the next day at a ratio of 1:5 dilution (virus:media) supplemented with 8 ug/ml of polybrene. Cells were infected overnight, and recovered for 24 hours in normal growth media. Selection was done under 500ug/mL of G418 (Thermo Fisher Scientific Cat: 10131035) until a plate of negative control cells was completely eliminated.

2.1. Oncosphere and Matrigel Assays

Oncospheres were generated by growing 500 – 1,000 freshly trypsinized single suspension cells in oncosphere media (RPMI 1640 media supplemented with 20 ng/ml EGF (Life Technologies Cat: PHG0311), 20 ng/ml bFGF (StemCell Cat: 02634) and 1x B-27 supplement (Life Technologies Cat: 17504-001). Cells were allowed to grow for at least 7 days undisturbed.

3D matrigel-on-top culture conditions were followed as previously described (Shibue et al., 2012) with the following modifications. 8-well chamber glass slides (Thermo Fisher Scientific Cat: 134534) were coated with matrigel (Corning Cat: 356237), and allowed to solidify at 37º C. 1,000 freshly trypsinized cells were placed on top of the matrigel layer, resuspended in normal growth media supplemented with 10% matrigel.

2.1. Immunofluorescence and Confocal Microscopy Analyses

Free-floating tissue sections that were previously archived in anti-freezing solution were washed thoroughly in 1X PBS three times to remove residual cryoprotectant.

Sections were permeabilized in PBS containing 0.25% Triton X-100 (PBS-T). Blocking was done for 1 hour at room temperature in blocking buffer (10% normal goat serum, Life Technologies Cat: 50-062Z, 2% BSA, and 0.25% Triton X-100). After blocking, sections were incubated in primary antibodies diluted in blocking buffer overnight at 4º C. To remove primary antibodies, sections were washed for six times in PBS-T at room temperature. Secondary antibody incubation was done using respective Alexa-Flour conjugated antibodies raised in goat (Life Technologies) at 1:500 dilution for 2 hours. Sections were washed three times in PBS-T, followed by three washes in PBS. To counter-stain nuclei, we incubated sections in 1:10,000 DAPI or Hoechst 33342 for 5 minutes, followed by two washes in PBS. Sections were transferred onto glass slides and allowed to air dry until translucent, followed by mounting using ProLong Gold or Diamond antifade mountant (Life Technologies, Cat. P36970). Slides were cured overnight at room temperature, and placed at -20º to +4º C for long-term storage.

Micrographs were captured using a TCS SP5 Confocal Microscope (Leica Microsystems) or an Imager.Z1 with Apotome.2 optical sectioning module (Zeiss). Captured images were processed using FIJI, an implementation of ImageJ, an imaging processing program developed at the NIH.

To generate Euclidian distance maps, we split multi-fluorescence channels to their component channels, and used the blur function to aid in the automated processing of the images. A thresholded image was generated for each channel

(ex. DAPI, GFP and Collagen IV), converted to a binary mask. To determine cancer cells in a given field, we watershed the DAPI mask to obtain individual nuclei, and computed the overlap of the GFP and DAPI channel using the 'and' operator in FIJI. ROIs were generated using the analyze particles function. To understand the relationship of these cells to the underlying vasculature, we converted the vessel mask into a Euclidian distance map, and computed the distance of each nuclei to its nearest vessel.

2.1. *Ex vivo* brain slice assays

We adapted a protocol previously described for the short-term culture of explanted brain slices (Polleux and Ghosh, 2002; Valiente et al., 2014). We obtained fresh brains from mice euthanized by cervical-dislocation, and embedded in 4% low-melting point agarose (Lonza) pre-heated to 37º C. Freshly-embedded brains were immersed into a bath of Hank's Balanced Salt Solution (HBSS) supplemented with HEPES (pH 7.4, 2.5mM), D-glucose (30mM), $CaCl_2$ (1 mM), $MgSO_4$ (1 mM), $NaHCO_3$ (4 mM) attached to a vibratome (Leica Microsystems). 250 μm sections of living brain slices were cut by the vibratome into the bath, and we collected sections from the bregma to approximately 3 mm in. Sections were cut into half at the midline, and placed onto 0.8 micron polycarbonate pore membranes (Thermo Fisher Scientific Cat: 09-300-66) free-floating in slice culture media (DME HG media supplemented with complete HBSS, 1mM Glu, 5% FBS, 100 IU/ml P/S). Explant brain slices were allowed to equilibrate in a 37º C incubator at 5% CO_2, after which 1.0 – 3.0 x 10^4 cancer cells were carefully pipetted on top of brain slices in a volume of 2 μl. Brain slices were allowed to incubate undisturbed for 72 hours.

Fixation was done with 4% paraformaldehyde overnight at 4º C, and free-floating immunofluorescence done as described above.

2.1. NK Cell Cytotoxicity Assays

We obtained single-cell splenocyte suspensions using a spleen dissociation protocol that utilizes a combination of enzymatic digestion (Miltenyi Biotec Cat: 130-095-926) and gentle mechanical disruption (Miltenyi Biotec Cat: 130-093-237). NK cells were purified from single cell suspensions by magnetic depletion of non-NK cells with a cocktail of antibodies against non-NK cells using a commercially-available NK Cell Isolation Kit (Miltenyi Biotec Cat: 130-115-818). Purified NK cells were cultured in RPMI 1640 media supplemented with 10% FBS, β-2ME, nonessential amino acids, 10mM HEPES, 0.5 mM sodium pyruvate, 2 mM Glu, and 10 IU/ml P/S. NK cells were activated by addition of 1000 U/ml recombinant IL-2 (PeproTech Cat: 200-02) overnight.

For cytotoxicity assays, we incubated target cancer cells labeled with eflour670 dye in the presence or absence of NK cells (effector:target ratio of 1:5) at 37º C for 3 hours, after which cytotoxicity was assessed by flow cytometry.

2.1 Atomic Force Microscopy

Previously sectioned free-floating sections of brain tissues were rinsed three times in PBS, and immobilized onto 30mm tissue culture dishes. Immobilized tissues were submerged in PBS to prevent dehydration. Brightfield and fluorescent images of brain tissues were acquired using an inverted Axio Observer.Z1 microscope (Zeiss) as the Atomic Force Microscopy (AFM) base. An MFP-3D-BIO Atomic

Force Microscope (Asylum Research) was used to collect force maps from brain tissue. A CP CONT-BSG-C (NanoAndMore.com) probe with a 20 μm borosilicate glass bead was used for all measurements. The Asylum Research GetReal calibration method was utilized for the determination of the spring constant (~.2 N/m). Each force map sampled a 90 μm x 90 μm region, in a 15x15 grid under fluid conditions (PBS). The trigger point was set to 100 nN. The force-indentation curves were fit to the Hertz model for spherical tips utilizing the Asylum Research Software to determine the Young's Modulus, with an assumed Poisson's ratio value of 0.45 for the sample (Chen et al., 1996). Force maps of stiffness along with individual stiffness values for each measured point were then exported from the Asylum Research Software for further analysis.

2.2 Animal Studies

2.2.1 Mouse Models

All animal experiments were conducted in accordance with the guidelines set forth by the MSKCC Institutional Animal Care and Use Committee (IACUC) as well as the Research Animal Resource Center (RARC). Female athymic nude (Envigo Stock: 069) or NOD-scid gamma (Jackson Laboratory Stock: 005557) mice used for *in vivo* xenograft studies were between 4 to 8 weeks of age. FVB.Tg(MMTVneu)$^{202Mul/J}$/FVB.Tg(MMTV-Erbb2) (Jackson Laboratory Stock: 002376) and FVB.N-Tg(MMTV-PyVT)$^{634Mul/J}$/FVB.Tg(MMTV-PyMT) (Jackson Laboratory Stock: 002374) mice were used as spontaneous models of mammary tumorigenesis. All mice were housed at the vivarium under a 12 light/12 dark hour

cycle, under controlled temperature and humidity. Mice had access to food pellets and water *ad libitum*.

2.2.2 Orthotopic Tumor and Experimental Metastasis Assays

To model metastatic dissemination through blood circulation, 0.5 – 1.0 x 10^6 cells were resuspended in 1.0ml cold sterile PBS. Mice were anaesthetized with an intraperitoneal injection of a cocktail of ketamine (100 mg/kg) and xylazine (10mg/kg) diluted in water. Upon confirmation of an appropriate plane of anesthesia, mice were secured onto a sterile surface with tape, and abdomen exposed. 100 ul of cell suspension was loaded onto a sterile slip tip syringe fitted with a 26G needle (BD), and injected intracardially into the left ventricle of the mouse heart. Pulsating red blood flow into the syringe indicates correct entry into the left ventricle. Baseline tumor burden was immediately assessed by retro-orbital injection of 100 ul of D-luciferin into the orbital plexus of the mouse eye using a sterile insulin syringe (BD), and imaging using an IVIS Spectrum *in vivo* imaging system (PerkinElmer).

Experimental lung metastases assays were undertaken using an intravenous tail-vein injection approach. Mouse tail veins were dilated by briefly placing mice underneath a 100 watt heating lamp. 100 ul of cell suspension was loaded onto a sterile slip tip syringe fitted with a 27G needle (BD), and mice were immobilized using a mouse strainer (Braintree Scientific Cat: TV-150 STD). With the needle tip bevel pointing downward, the needle is inserted near parallel to the tail of the mouse. Successful entry into the tail vein is indicated by entry of red blood into the

syringe, and little resistance as the cell suspension is dispensed into the vein. Baseline lung burden was assessed as previously described.

To simulate *de novo* growth at the primary site, we orthotopically implanted cells into the mammary fat pad (MFP) of mice. Cell suspensions were prepared by diluting the requisite number of cells into cold sterile PBS such that the amount of cells to be injected into the mammary fat pad were in a volume of 25 ul. Mice were anaesthetized using a cocktail of ketamine/xylazine (previously described), and the skin surrounding the fourth and fifth nipple (near the hind leg) disinfected with alternating swabs of 70% ethanol and povidone-iodine (Betadine) solution. A small incision was made using sterilized scissors between the fourth and fifth nipple to expose the mammary gland underneath, taking care so as not to puncture the peritoneum. Immediately prior to injection, cold matrigel was added to the cell suspension at 1:1 ratio, and 50ul loaded onto a pre-chilled insulin syringe. Proper injection of cells into the MFP was ascertained by clear swelling of the MFP site with no signs of leaking. The incision site was closed using 7mm steel reflex wound clips (Braintree Scientific Cat: RF7). Bupivacaine and Buprenorphine were administered post-operatively as analgesia. Wound clips were removed 7-14 days after surgery.

Metastatic burden was recorded weekly or bi-weekly by bioluminescent (BLI) imaging. Orthotopic tumors were monitored by measurement using a digital caliper

(VWR Cat: 62739-531). Tumor volumes were computed using the formula $(\pi LW^2)/6$ as previously described.

2.2.3 Sectioning of organ tissues

Harvested organs were immersed in 4% aqueous paraformaldehyde (Electron Microscopy Sciences Cat: T15710) overnight at 4º C, and rinsed in PBS. This was followed by an overnight immersion in 30% sucrose solution at 4º C to cryo-protect tissues. Organs were mounted onto freezing platform of a sliding microtome (Thermo Fisher Scientific Cat: HM450) using Tissue-Tek OCT compound (Sakura Cat: 4583), and frozen to -30º C. 80-micron thick sections were obtained and serially stored (1:10) in 2.0ml vials containing anti-freezing solution (30% polyethylene glycol, 30% glycerol, in PBS) and stored at -20º C. Because sections were stored sequentially, each vial was representative of the entire organ of interest.

2.2.4 *In vivo* depletion of NK cells

We depleted NK cells by intraperitoneal injection of 100 μl of anti asialo-GM1 (Wako Chemicals Cat: 98610001) every 5 days from the experimental start date. To confirm NK cell depletion, we isolated peripheral blood from untreated and anti asialo-GM1 treated mice, lysed red blood cells using ACK lysis buffer (Lonza Cat: 10-548E). Cells that remained post-RBC lysis were resuspended in flow buffer (2% FBS, 0.25mM EDTA, 1X PBS) and stained with anti-NK1.1-PE antibody (Miltenyi Biotec Cat: 130-102-991) for 30 minutes. Cells were washed in flow buffer, and analyzed on a Fortressa flow cytometer (BD).

2.2.5 Microglia inhibition by Minocycline

Minocycline inhibition of microglial activation was followed as previously described (Kobayashi et al., 2013). Athymic nude mice injected with 1.0 x 10^5 cancer cells were either treated with minocycline (Sigma Aldrich Cat: M9511) at 50 mg/kg by intraperitoneal injection, or mock saline. Treatment was done every day for 14 days, after which mice were euthanized and organs harvested. Free-floating frozen sections from harvested tissues were obtained as previously described.

2.3 Bioinformatic and Statistical Analyses

2.3.1 RNA-Seq and Downstream Data Analyses

Total RNA was isolated from cancer cells growing *in vitro* in described conditions using PrepEase RNA Spin Kit (Affymetrix) according to the manufacturer's instructions. RNA quality was checked and samples with an integrity number of greater than 9.5 were used for RNA-Seq experiments. Libraries were constructed using either TruSeq RNA Sample Prep Kit v2 (Illumina Cat: RS-122-2001) or NEBNext Ultra RNA Library Prep Kit (New England Biolabs Cat: E7530S). Libraries were sequenced on a HiSeq 2500 high-throughput sequencing system (Illumina) at a depth of 25-50 million reads per sample. Raw FASTQ reads were quality-checked and mapped to a reference human (hg19) or mouse (mm9) genome using Tophat2 (2.2.4) (Langmead and Salzberg, 2012). The number of unique reads per gene were counted using HTSeq (0.6.1p1) (Anders et al., 2015). Downstream bioinformatics analyses were done in RStudio (1.0.153) implementing R (3.4.1), or using tools publicly available online (DAVID, GSEA). To

determine differentially expressed genes between two given conditions, we implemented the DESeq2 package (Love et al., 2014) in R using default settings. Differentially expressed genes were defined as genes that met the threshold of q <0.05, a fold change > 2.0 or < -2.0, and a mean read count of >10. Principal Component Analyses (PCA) were done using the prcomp function in R. Heatmap and PCA plots were generated using the gplots and ggplot2 packages in R. Pathway signature scores were computed using sum of z-score or gene-set variation analysis methods using previously curated gene signatures (Bild et al., 2005; Gatza et al., 2010; Hänzelmann et al., 2013; Nguyen et al., 2009; Zhang et al., 2013).

To identify enriched gene ontology (GO) terms, we employed the web-based tool Database for Annotation, Visualization and Integrated Discovery (DAVID v6.8) (Huang et al., 2009a). DAVID computes enrichment scores for a target set of genes vis-à-vis a curated list of GO terms, to determine over-represented terms present in a target gene set.

2.3. Statistical Analyses

Statistical testing on all data were performed using Prism 5 or 6 software (Graphpad). P values were computed using a two-tailed Mann-Whitney Test unless otherwise noted. Quantitative data were expressed as mean +/- the standard error of the mean.

2.3. Accession Numbers

RNA-Seq and ChIP-Seq data were deposited in the Gene Expression Omnibus database under accession numbers GSE72956 and GSE83132.

Chapter 3: Immune Evasion and Metastatic Latency

3.1 Introduction

Most cancer patients often succumb because of metastatic disease – patients whose primary disease have been successfully treated frequently relapse with metastasis at distant organ sites many years later. At the point at which primary tumors are detectable, these tumors are likely shedding disseminated tumor cells into the circulation. Disseminated tumor cells are frequently detected in the peripheral blood of patients with detectable primary disease (Cristofanilli et al., 2004). Although a majority of dispersed cells perish in the bloodstream or soon after infiltrating distant organs, a minority may survive as latent seeds in host tissues, as single cells or small micrometastases that are not visible even with the most sensitive of detection techniques. As a result, patients who are putatively considered disease-free in the clinic after cancer treatment may carry thousands of disseminated tumor cells (DTCs) in the bone marrow or other organs (Braun et al., 2005). Despite being a major concern in the clinic, there is a paucity in our understanding of latent metastasis. Little is known about the nature of dormant DTCs and the mechanisms that permit these cells to remain quiescent, evade immunity, retain tumor-initiating capacity, and progress into aggressive metastasis (Massagué and Obenauf, 2016).

When we think of latent disease, a leading hypothesis posits that dormant DTCs are tumorigenic cells that enter quiescence in a paracrine manner by the action of growth inhibitory signals derived from the host tissue stroma (Sosa et al.,

2014). Recent studies have identified stromal TGF-β and BMP as inhibitors of DTC growth (Bragado et al., 2013; Gao et al., 2012; Kobayashi et al., 2011). However, many organs where DTCs have been detected, such as the bone marrow, liver and lungs, support cell proliferation as part of their normal tissue homeostasis and regenerative processes, making it unlikely that constant exposure to stroma-derived inhibitors explain the long-term latency of DTCs.

Furthermore, the role of the immune system in metastasis has re-emerged as an important concept and an area of active research interest. The dynamic interplay between immune cells and cancer cells plays an important role in the evolution of cancer (Eyles et al., 2010; Schreiber et al., 2011). Case reports of immunosuppressed organ transplant recipients developing donor-derived metastasis from organs donated by donors who had been considered cured of melanoma, or glioblastoma, considered a non-metastatic tumor, highlight the role of immune surveillance in preventing the outgrowth of dormant DTCs (MacKie et al., 2003; Xiao et al., 2013). Dormant DTCs likely need to engage mechanisms to prevent their decimation by the immune system.

Our understanding of the molecular basis for latent metastasis has been limited by the scarcity of preclinical models that recapitulate key features of this metastatic stage (Massagué and Obenauf, 2016). We isolated latency competent cancer (LCC) cells by *in vivo* selection of human tumor cell populations in mice. Using these models, we show that LCC cells express SOX transcription factors,

and have stem cell-like features that prime their ability to enter quiescence and evade innate immunity. These cells can actively self-impose a slow-cycling state by producing DKK1, an inhibitor of the WNT signaling pathway. We propose a quiescence-linked mechanism for evasion of NK-cell mediated clearance, allowing for the long-term survival and eventual evolution of these latent metastasis-initiating cells.

3.2 Results

3.2.1 Latency Competent Cancer Cells Isolation from Early Stage Breast and Lung Cancers

We isolated cancer cells with the competency to seed distant organs with latent metastasis (latency competent cancer cells, LCC cells) from two sources – H2087, an established lung cancer cell line derived from stage I lung adenocarcinoma (Gazdar and Minna, 1996), and HCC1954, a breast cancer cell line derived from the primary tumor of a stage IIA HER2+ patient (Gazdar et al., 1998) (Figure 3-1). Stage I lung adenocarcinoma patients who had their primary cancers surgically resected are still at risk of developing relapse, suggesting the presence of latent disseminated disease (IELCAP Investigators et al., 2006; Maeda et al., 2010). In addition, HER2+ breast cancer patients whose overall prognosis have greatly improved from anti-HER2 therapies are now experiencing a marked increase in the incidence of brain metastasis (Duchnowska et al., 2009). Both cancer types are important sources of latent metastasis in the clinic, and serve as suitable models for studying this disease pre-clinically.

H2087 and HCC1954 parental cells transduced with a GFP-luciferase reporter and antibiotic resistance vectors (Ponomarev et al., 2004) were intracardially injected into the arterial circulation of athymic nude (FOXN1^{nu}) mice (Kozlowski et al., 1984). We non-invasively monitored mice for signs of metastatic growth by BLI. After 3 months, mice with no discernible metastatic outgrowth were euthanized and organs harvested and dissociated into single cell suspensions *in vitro* to recover antibiotic-resistant cancer cells from the lungs and kidneys of mice injected

with H2087 or from the brains of mice injected with HCC1954 (Figure 3-1). We orthotopically injected LCC cells and find that their tumorigenic activity is similar to that of parental populations (Figure 3-2), suggesting that these LCC cells retain tumor-initiating potential after months of latency in mouse tissues.

Of 20 athymic nude mice injected H2087-LCC cells, one developed overt metastases, one with spinal metastasis after 4 months that did not progress, two developed incipient lesions after 7 months, and 16 remained metastasis-free for over 8 months. Only one mouse injected with HCC1954-LCC1 developed overt metastasis in 4 months (Figure 3-3, Figure 3-4). In comparison, aggressive breast (MDA-MB-231) or lung adenocarcinoma (H2030) metastatic lines readily formed extensive metastases within 3-4 weeks.

3.2.2 LCC Cell Localization in Infiltrated Organs

Two weeks post-inoculation, we find that ~20% of disseminated GFP+ HCC1954 cells in the brain were found in small micrometastases (>10 cells), and the rest of events as single cells (Figure 3-5). Looking at long-term latent populations (1 month and 2 months post-inoculation), the same trend is exhibited, with a majority of GFP+ cancer cells found as single disseminated cells (Figure 3-5). In the brain, HCC1954 LCC cells were closely associated with the vasculature. Aggressive brain metastatic cells rapidly spread over the abluminal surface of cerebral microcapillaries and this spreading is required for their metastatic outgrowth (Valiente et al., 2014). In contrast, LCC cells infiltrating the brain parenchyma initially spread along capillaries transiently, and subsequently adopt a rounded

morphology (Figure 3-6). H2087 cancer cells were detected in the kidney between the renal tubules, adjacent to capillaries, or within glomeruli. In the lungs, these cells were found within alveolar walls (Figure 3-7). Similar to HCC1954 LCC cells, these cells were associated with blood capillaries. We do not find any evidence of cancer cells persisting away from blood vessels.

3.2.3 LCC Cells Are Prone to Enter Quiescence

To monitor proliferation in the first days post-inoculation, we labeled LCC cells with 5-ethynyl-2'-deoxyuridine (EdU) prior to intravenous injection into athymic mice. Proliferation would dilute the amount of EdU retained in these cells. After 14 days, ~60% of LCC cells in the lungs retained EdU versus 15-25% in parental population, indicating that LCC cells were able to stay in quiescence more readily (Figure 3-8). When we interrogate LCC cells several months post inoculation, we find that many of these cells are negative for the proliferation marker Ki67+. Ki67+ LCC cells were largely confined to cell clusters (Figure 3-9).

We mimicked the stress that these cells likely face upon entry into a distant organ site by depleting them of mitogens in culture. To determine the effect of a mitogen-poor environment, we cultured LCC cells in mitogen-low media (MLM) containing reduced serum conditions, or mitogen-rich media (MRM) containing normal serum conditions. Under MLM conditions, LCC cells underwent a rapid decrease in proliferation, as evidenced by their ability to retain EdU in culture (Figure 3-10), dye retention (Figure 3-11), and CellTiter-Glo assays (Figure 3-12), whereas the

parental line showed little or no decrease in proliferation in MLM conditions. LCC cells accumulated at the G0/G1 phase by DNA content analysis (Figure 3-13), with no change in apoptosis as determined by Caspase-Glo 3/7 assay (Figure 3-14). In sum, LCC cells recapitulate key features of the latent metastatic state, including a propensity to enter proliferative quiescence, an ability to survive as latent seeds in relevant organs for months, and retention of tumorigenic and metastasis initiating capacity.

3.2.4 LCC Cells Molecularly Cluster with Stem/Progenitor Cells

We performed genome-wide bulk RNA sequencing (RNA-Seq) of HCC1954 and H2087 derivatives grown under MRM or MLM culture conditions to understand the transcriptomic landscape of these cells (Figure 3-15). Gene set enrichment analysis (GSEA) of differentially expressed genes in HCC1954 LCC cells versus parental cells identified a mammary stem cell signature (MaSC) as a top-scoring gene set, under both MLM and MRM conditions (Figure 3-16). Principal component analyses revealed clustering of HCC1954 LCC cells with human and mouse mammary stem and progenitor cells, away from more mature luminal and stromal compartments (Figure 3-17) (Lim et al., 2010). Moreover, HCC1954 LCC cells were enriched for the surface marker profile $CD44^{hi}/CD24^{low}$, which is akin of human breast cancer stem cells (Figure 3-18) (Al-Hajj and Wicha, 2003). In H2087 derivatives, we find that H2087 LCC cells clustered with stem-like alveolar type I and bipotent progenitor (BP) cells, while H2087 parental cells clustered with alveolar type II and Clara cell lineages in both MRM and MLM conditions (data not

shown). In limiting dilution assays, LCC cells showed a four-fold increase in tumor-initiating capacity compared to parental cells (Figure 3-19). Together, these data suggest that LCC cells are enriched for cancer cells with stem-like/progenitor cell features.

3.2.5 Sox2 and Sox9 Association with the LCC Phenotype

Progenitor cell identity is determined by lineage-specific transcription factors. Notably, two master regulators of stem and progenitor cell identity, SOX2 (Arnold et al., 2011) and SOX9 (Guo et al., 2012), ranked high among transcription factors whose expression was prominently associated with the LCC phenotype. HCC1954 LCC cells were high in SOX9 expression, but expressed low levels of SOX2 at both the RNA (Figure 3-20, Figure 3-21) and protein (Figure 3-22) level. In contrast, SOX2 expression was predominant in H2087 LCC cells (Figure 3-21, Figure 3-22). Expression of SOX and SOX9 in LCC cells was also confirmed by immunofluorescence staining of LCC cells sitting *in situ* in the brain or lungs (Figure 3-23). We find Sox expression in single disseminated LCC cells and also small micrometastases clusters. LCC cell metastatic lesions that have outgrown had variegated expression of Sox2 and Sox9 by immunofluorescence (Figure 3-24). As normal mammary cell or breast cancer cell populations divide, the $CD44^{hi}/CD24^{lo}$ compartment dilutes out, as progeny acquire CD24 content, demonstrating the plasticity of this population (Liu et al., 2014). HCC1954-LCC2 cells sorted by CD24 content show enrichment for SOX9 when CD24 content was low (Figure 3-25). We transduced H2087 LCC cells and HCC1954 LCC cells with short hairpin RNAs (shRNA) targeting SOX2 and SOX9 respectively. We

inoculated LCC cells into athymic mice by tail vein or intracardiac inoculation and monitored colonization of the lung or brain by whole body BLI imaging for 60 days. Histologic analysis of lungs (H2087 LCC) or brains (HCC1954 LCC1) demonstrated a marked decrease in the number of metastatic seeders when Sox2 or Sox9 are depleted in LCC cells (Figure 3-26). Colony formation by oncosphere growth in suspension has been demonstrated as a surrogate *in vitro* assay to determine tumorigenic potential (Dontu et al., 2003). LCC cells formed the same number of oncospheres as their parental counterparts, although LCC oncospheres were smaller (Figure 3-27). Knockdown of either SOX2 or SOX9 resulted in inhibited oncosphere formation in LCC cells but not in their parental lines (Figure 3-28). Taken together, LCC cells are likely a distinct subpopulation of stem-like cancer cells characterized by high SOX2 or SOX9 and a dependence on these transcription factors for growth under restrictive conditions *in vitro* and seeding of latent metastasis in mice.

3.2.6 Metastatic Latency Balanced by NK Cell Immune Surveillance

Only a fraction of LCC cells seed organs with latent disease, suggesting that they suffer massive decimation in athymic mice. Although the elimination of disseminated cancer cells may be due to metabolic and mechanical stresses (Goss and Chambers, 2010; Sosa et al., 2014), the immune system may also be a contributing factor to the demise of these cells (Dunn et al., 2004). Although athymic nude mice are thought of as an immunocompromised mouse model, these mice retain functional components of innate immunity such as NK cells, raising the

possibility that immune surveillance restricts the expansion of LCC cells in these mice. To test this possibility, we inoculated LCC cells into a more thoroughly immunocompromised mouse model, NOD.Cg-*Prkdc*^{scid} *Il2rg*^{tm1Wjl}*/SzJ* (NOD/SCID Gamma, NSG), which is defective for both adaptive and innate immune responses (Shultz et al., 2005). Strikingly, HC2087-LCC and HCC1954 cells formed overt metastases with high penetrance (Figure 3-29) in multiple organs (Figure 3-30).

To test NK cells as candidate inhibitors of LCC expansion, we depleted athymic mice of NK cells by administration of polyclonal anti-asialo GM1 antibody or anti-NK1.1 monoclonal antibody PK136 (Sun and Lanier, 2008) (Figure 3-31). NK cell depletion strategies resulted in permissive outgrowth of HCC1954-LCC1 cells, as shown by marked increase in whole-body BLI signal, and an increase in metastatic burden in the brain (Figure 3-32, Figure 3-33). Similar results were observed in NK cell depletion in H2087 LCC lines, with outgrowth observed in bones (Figure 3-34). To investigate the role of NK cells in immunocompetent mouse models, we used lung adenocarcinoma cell lines derived from tumor-bearing KRAS^{G12D}/p53^{Del} mice (Winslow et al., 2011). The 482T1 (T-Met) cell line readily metastasizes to the liver when injected into the spleen of syngeneic B6129SF1/J mice, whereas the 368T1 (T-nonMet) line does not. NK cell depletion with anti-asialo-GM1 antibody resulted in a 100-fold increase in the liver metastatic activity of T-nonMet cells, reaching a level that was comparable to that of T-Met cells. In a second model, we used 4T07 cells, a non-metastatic cell line derived from a spontaneous BALB/c mouse mammary tumor (Aslakson and Miller, 1992). NK cell depletion of recipient BALB/c

mice significantly increased the overall metastatic activity of 4T07 (Figure 3-35). Notably, treatment of athymic mice with anti-asialo-GM1 antibody 40 days after inoculation of H2087 LCC or HCC1954 LCC cells triggered an increase in metastatic burden compared to mice with intact NK cells (Figure 3-36).

These results demonstrated the ability of latent LCC cells to stochastically initiate outgrowth when NK cell surveillance in lifted. Collectively, the evidence suggests that LCC cells can proliferate after infiltrating distant organs, but NK cell immune surveillance prevents overt outgrowth, sparing LCC cells that entered quiescence. Latent LCC cells remain competent to initiate metastatic outgrowth and abruptly manifest this competence if NK cell surveillance ends.

3.2.7 Downregulation of NK Cell Activators in Quiescent LCC Cells

A balance of activating and inhibitory signals regulates the ability of NK cells to target cancer cells (Vesely et al., 2011; Wu and Lanier, 2003). In order to evade immune surveillance, cancer cells engage mechanisms to evade NK cell-mediated recognition (Ljunggren and Malmberg, 2007). As LCC cells survived NK cell surveillance in athymic mice, we queried LCC gene expression profiles for potential mechanisms of immune evasion. We examined gene expression signatures associated with immune recognition by macrophages, T, B, or NK cells. The expression of NK cytotoxicity signatures was specifically decreased in LCC cells relative to parental cells (Figure 3-37). Moreover, slow-cycling MLM conditions induced further changes in the expression of NK cell ligands in LCC cells (Figure 3-38). These changes include specific genes involved in mediating

anti-tumor responses (UL16-binding proteins (ULBP; also known as retinoic acid early transcript, RAET) ULBP2, ULBP3, ULBP5, which bind to the NK activating receptor NKG2D/CD314(Lanier, 2015), and PVR/CD155, a ligand for the cancer cell killing NK cell receptor CD226/DNA-1 (DNAX accessory molecule-1) (Martinet and Smyth, 2015). In addition, pro-apoptotic cytokine receptors FAS and TRAILR (Bradley et al., 1998; Takeda et al., 2001), which are important for NK-cell mediated target killing, were also downregulated in LCC cells under MLM conditions (Figure 3-39). We confirmed downregulation of CD155 and ULBPs by flow cytometry analysis (Figure 3-40).

To determine whether LCC cells entering quiescence are intrinsically resistant to the cytotoxic action of NK cells, we incubated parental and LCC cells in MLM culture conditions and then added freshly isolated, IL-2-activated mouse spleen NK cells to cultures *in vitro*. Compared to parental populations, LCC cells were more resistant to NK-cell mediated cytolysis *in vitro* (Figure 3-41). Thus, LCC cells that are induced to enter quiescence undergo a striking downregulation of NK cell activators and acquire heightened resistance to NK-cell mediated killing.

3.2.8 Attenuated WNT Signaling is Associated with LCC Quiescence

To identify what primes LCC cells to enter this immune evasive quiescent state, we applied signaling pathway classifier analysis to the transcriptomic datasets. Under quiescence MLM conditions, H2087 LCC cells showed a reduction in WNT, MYC and NF-kB signaling, and an increase in TGF-β signaling. We found that WNT signaling was also attenuated in HCC1954 LCC cells under these conditions

(Figure 3-42). The drop in WNT signaling in LCC cells that entered quiescence was intriguing. WNT is a potent mitogen for stem and progenitor cells and is implicated in the metastatic outgrowth of lung adenocarcinoma (Nguyen et al., 2009) and breast cancer stem cells (Malanchi et al., 2011; Oskarsson et al., 2011). In HCC1954 LCC cells, we assessed WNT activity by *in vivo* immunostaining for active β-catenin, a marker for canonical WNT pathway activation. We detected higher levels of active β-catenin in proliferating LCC cell clusters than in single disseminated LCC cells in the brain (Figure 3-43). H2087 LCC cells in MLM conditions showed resistance to pathway activation by WNT3A addition, as determined by AXIN2 expression and TCF transcriptional reporter activation (data not shown, Malladi). These data suggest that LCC cells have a propensity to resist WNT pathway activation.

3.2.9 Involvement of autocrine DKK1 expression in enforcing a quiescent, immune evasive state

These results raised the possibility that LCC cells might express WNT inhibitors as they enter quiescence. We observed that WNT inhibitor dickkopf-related protein 1 (DKK1) was highly expressed in LCC cell lines by mRNA expression and ELISA (Figure 3-44). ChIP-seq analyses showed a clear increase in activating H3K27ac and Pol II peaks at the DKK1 locus in both LCC models, compared to parental lines (Figure 3-45). We confirmed DKK1 expression in LCC cells *in vivo* by immunofluorescence staining (Figure 3-46). DKK1 knockdown stimulated the proliferation of LCC cells under MLM culture conditions by CellTiter-Glo (Figure 3-47). If autocrine DKK1 helps prime LCC cells to adopt a slow-cycling state, which aids evasion of NK cell mediated clearance, a plausible hypothesis would be that

DKK1 protects LCC cells from elimination in athymic mice. To this end, we exposed LCC cells depleted of DKK1 by shRNA and find that these cells are more susceptible to NK-cell mediated cytotoxicity (Figure 3-48). DKK1 knockdown increased the metastatic growth of H2087 and HCC1954 LCC cells in NSG mice (Figure 3-49). DKK1 knockdown in H2087 LCC cells increased the expression of NK cell activating ligands, and decreased the accumulation of LCC cells in lungs of inoculated athymic nude mice (data not shown, Malladi). As a corollary, depletion of SOX2 in H2087 LCC or SOX9 in HCC1954 LCC cells attenuates the metastatic ability of these cells even in the permissive condition sof NSG mice (Figure 3-50). Thus, these data support the importance of SOX transcription factors for metastatic growth of LCC cells regardless of the permissivity of the microenvironment, and the important role of NK cells in mediating the restraint of LCC cell outgrowth.

3.3 Conclusions and Discussion

Our results show that cancer cell populations selected from lung and breast cancer cell lines for their competence to establish latent metastasis have high expression of stem/progenitor markers. They also have a capacity to enter immune evasive quiescence while retaining metastasis-initiating capabilities. Although many LCC cells are decimated as they proceed to infiltrate distant organs, these cells can stochastically enter a slow-cycling quiescent state, which leads to downregulation of NK cell ligands for evasion of immune surveillance. NK cells kill dividing LCC cells but spare LCC cells in quiescence. As a result, cancer cells in these models can persist long-term as latent seeds in different organs (Figure 3-51).

Growth inhibitory signals from the host microenvironment and the perivascular niche, including TGF-β and BMP, can contribute to metastatic dormancy (Sosa et al., 2014). However, disseminated cancer cells are likely exposed to mitogenic signals during the course of latency *in situ*, as perivascular niches in host organs support normal tissue homeostasis and regeneration through stromal WNT and other proliferative signals. Our results demonstrate an innate ability of LCC cells to self-impose a slow cycling state in this context. This ability is based in part on the expression of the WNT inhibitor DKK1, which prevents activation of b-Catenin and LCC cell proliferation. We show that autocrine DKK1 helps disseminated LCC cells enter quiescence, and that cells that lose DKK1 are more proliferative. In the model, self-imposed quiescence likely counterbalances the action of stromal WNT signals to preserve the viability of residual LCC cells in the host tissue.

Proliferative quiescence protects LCC cells from NK cell-mediated killing. Upon

entering a quiescent state, LCC cells downregulate cell surface ULBP activators of NK cell-mediated cytotoxicity and receptors for cell death signals. In mice with an active innate immune system, LCC cells are mostly found as quiescent single cells. LCC cell clusters observed under these conditions contain actively proliferating cells, but may be fated to undergo NK-mediated clearance. Depletion of NK cells by in different mouse models led to aggressive metastatic outgrowth of LCC cells, arguing that quiescent LCC cells stochastically enter the cell cycle, and that proliferative clusters will progress to macrometastases if immune surveillance is relaxed. The ability to undergo periodic bursts of proliferation and elimination, with a small fraction of the progeny entering quiescence and surviving after each round, would allow disseminated cancer cells to evolve additional metastatic traits, such as active immunosuppression and organ-specific colonization traits, for an eventual macrometastatic outbreak. Metastatic evolution would be less likely in a permanently quiescent cancer cell population.

Our observations in latent metastasis are in line with the role of immune surveillance in restricting malignant cell proliferation in other contexts. Clinically, the presence of NK cell infiltrates in primary colorectal, gastric, and lung cancer correlates with better patient survival outcomes, consistent with an ability of NK to keep metastases in check (Finak et al., 2008; Jin et al., 2014; Villegas et al., 2002). Because NK cells have the ability to limit LCC cell outgrowth, a drop in NK cytotoxicity index in disease-free cancer patients might serve as a prognostic indicator of disease relapse. The possibility of treating residual disease by inducing proliferation in order to re-sensitize cancer cells to adjuvant cytotoxic

chemotherapy would entail the risk of triggering metastasis while trying to prevent it. Our findings raise the possibility of selectively reactivating NK cell ligands in quiescent metastatic cells in order to trigger the immunologic elimination of latent metastasis.

Chapter 4: Metastatic Outgrowth through Immune Exclusion

Chapter 4.1 Introduction

Breast cancer remains to be a leading cause of death in women (Siegel et al., 2016). Of the four major subtypes of breast cancer (Luminal A, Luminal B, Triple-Negative, HER2+), approximately one in five patients with breast cancer are positive for overexpression of the HER2/ERBB2 receptor (Slamon et al., 2001). HER2+ breast cancer was historically a harbinger of dismal prognosis and poor survival (Sørlie, 2004), as expression of HER2 elicits strong activation of pro-survival and proliferation pathways such as AKT and MAPK (Hudis, 2007; Lin and Winer, 2007). The reliance of these cancer cells on HER2 expression presents with a liability of being addicted to its expression (Pagliarini et al., 2015). Targeted therapies developed against HER2 provide significant benefit in controlling the disease, resulting in remarkable gains in the prognosis of HER2+ breast cancer patients (Geyer et al., 2006; Slamon et al., 2001; Swain et al., 2015). These therapies are now currently being tested in cancer settings outside of breast cancer where HER2 pathway activation is becoming more frequently detected (Bang et al., 2010; Hecht et al., 2015; Noh et al., 2014).

Despite this marked improvement in patient survival, many patients still succumb to disease burden. The development of CNS metastases has come to forefront of clinical practice in HER2+ breast cancer, with up to 50% of HER2+ patients reported to develop CNS metastases (Leyland-Jones, 2009; Lin and Winer, 2007). None of our current standard-of-care treatments for brain metastatic disease are curative (Brufsky et al., 2011a). HER2+ breast cancer will be a significant

contributor to CNS metastases for the foreseeable future, making it imperative that we understand the underlying traits that allow for their success.

The increase in incidence for CNS metastases in HER2+ breast cancer has been previously attributed to the highly variable ability of current targeted therapies such as lapatinib or trastuzumab in crossing the blood brain barrier (Morikawa et al., 2014). Cancer cell induction of blood brain barrier leakiness has been attributed to the ability of lapatinib and trastuzumab to cross the blood brain barrier, albeit at concentrations 10-20% that of extracranial spaces (Taskar et al., 2011). Retrospective reports from the *pre*-trastuzumab era suggest that HER2 positivity itself contributes to the proclivity for successful colonization of the brain, with HER2+ breast cancer patients being 2 – 4 times more likely to develop CNS metastases compared to HER2- cohorts. Emerging evidence in the literature has demonstrated increased HER2 activity in CNS metastases in otherwise HER2 negative primary cancers.

The brain microenvironment is replete with numerous native immune cell types, all poised to quickly eliminate foreign threats that might infiltrate the brain, making it a particularly hostile environment for invaders such as metastatic cancer cells (Quail and Joyce, 2017). Our lab and others have previously characterized important properties that aid the ability of cancer cells to circumvent their elimination in the brain parenchyma or the leptomeningeal space (Boire et al., 2017; Bos et al., 2009; Valiente et al., 2014). Given the propensity of HER2+ breast cancer for developing CNS metastases, and its emerging role in providing brain-tropic propensity, we wondered how HER2+ CNS metastases might be different, and if so, what properties might protect them from killing.

Our previous work highlighted the importance of initial vascular cooption for the successful outgrowth of brain metastases in models of triple-negative breast and lung cancers (Valiente et al., 2014). In this chapter, we describe the remarkable ability of HER2+ cancer cells to quickly disengage vascular-cooptive growth in favor of spheroidal growth, a type of growth where cancer cells are configured into tightly-adhering cell clusters *in vivo*. This configuration is aided by the secretion of a milieu of extracellular matrix (ECM) factors, such as COL4A1 and TNC, and ablation of these factors re-permits cancer cells to coopt the vasculature. Surprisingly, we provide evidence to demonstrate that prolonged engagement of vascular cooption by HER2+ cancer cells leads to their recognition and decimation by microglia, a major innate immune cell type in the brain.

Chapter 4.2 Results

4.2.1 HER2+ brain-tropic cancer cells adopt early spheroidal growth

To study HER2+ breast cancer brain metastases, we generated brain-tropic derivatives from several established human and mouse HER2+ cancer cell lines by inoculation of these GFP-luciferase labeled cell lines into the arterial circulation of athymic nude or background-matched (i.e. FVB/N) mice. Mice which presented with bioluminescent (BLI) signal in the head were indicative of cancer cells that successfully homed to the brain. Using the mouse as a living cell sorter, we harvested BLI-positive brains to derive our brain-tropic metastatic (BrM) derivatives. We repeated this process again to derive second-generation BrM derivatives **(**Figure 4-1**)**.

HER2+ BrM2 derivatives were enriched for their propensity to generate brain metastases *in* vivo as compared to their parental lines, with most mice exhibiting brain metastases at 30 days post-inoculation **(**Figure 4-2**).** *In vitro*, BrM lines displayed no marked increase in proliferation, suggesting that their increased propensity to develop brain metastases is not a byproduct of selecting a sub-population of cells with increased proliferation rates **(**Figure 4-3**)**.

We recently identified an important role for L1CAM-mediated vascular cooption in the colonization of the brain in the context models representative of triple negative breast cancer (MDA-231 BrM) and lung adenocarcinoma (H2030 BrM). As these cancer cells extravasate, their initial outgrowth requires intimate association with the underlying vasculature, facilitating their rapid proliferation and eventual graduation to overt metastatic lesions (Valiente et al., 2014). In these models, failure to coopt results in poor colonization of these cells, a finding we have since

extended to be a generalizable phenomenon of these cells (triple negative breast cancer, lung cancer, renal cancer) in their colonization of other organ sites (lung, liver, brain). We wanted to extend these findings in the context of HER2+ breast cancer brain metastases, and investigated the dynamics of these cells as they colonize the brain parenchyma.

In *in* vitro time lapse microscopy of HER2+ cancer cells on top of explant brain slices, we find these cells to be highly active **(**Figure 4-4**)**, with full competency to stretch on blood vessels and use them as tracks to move about. To our surprise, examination of HER2+ cancer cells *in vivo* in the brain at early time points reveal a majority of cells scored in the brain parenchyma to be found in cell clusters, with a largely spheroidal morphology (Figure 4-5**)**. This is in stark contrast to the vessel ensheathment we have previously characterized in triple negative breast cancer and lung adenocarcinoma brain metastases. We found 90% of incipient HER2+ metastastic lesions in brain coronal sections we examined to adopt a spheroidal growth pattern, which persisted for several weeks after extravasation into the brain parenchyma **(**Figure 4-6**)**. To quantitate the association of cancer cells to blood vessels, we converted isolectin-B4 labeled vasculature into a Euclidian distance map to measure how far cancer cells were to their nearest blood vessel. Whereas HER2- cancer cells predominantly placed themselves on blood vessels, 70% of HER2+ cancer cells were found more than a cell's distance from blood vessels, suggesting the ability of HER2+ cells to persist without the need for being in direct contact with blood vessels **(**Figure 4-6**)**. Cells at a distance from blood vessels are Ki67+, suggesting that direct contact with blood vessels is not required for their active proliferation **(**Figure 4-7**)**. We find prevalent evidence for spheroidal growth in other HER2+ models – we detect *in vivo* cell clusters in early metastatic lesions from mice intracardially seeded with human xenograft JIMT1 BrM2 and mouse

syngeneic MMTV-Erbb2 BrM2 **(**Figure 4-8). Furthermore, we harvested organs from transgenic FVB.MMTV-Erbb2 mice that develop spontaneous mammary tumors and find micrometastases in the lung and brain in the spheroidal configuration **(**Figure 4-8**)**. Finally, we find preliminary evidence for spheroidal growth in the primary breast cancer tumor of a HER2+ patient **(**Figure 4-8**)**. In parallel, we interrogated HER2+ and HER2- cancer cells in explant brain slice assays to determine if we can detect cell clustering in this context. HER2+ cancer cells readily aggregate with each another as they chemotact to blood vessels, whereas a majority of HER2- cancer cells chemotact directly onto blood vessels with little aggregation **(**Figure 4-9**).** We rendered fully-captured z-stacks in 3D to visualize that HER2+ cell clusters on brain slices were fully intercalated with the underlying vasculature, and not just aggregated on the surface of the brain parenchyma **(**Figure 4-9**)**. Collectively, these data demonstrate a remarkable ability for HER2+ brain-tropic metastatic cancer cells to adopt a spheroidal growth configuration as they begin colonization of the brain parenchyma.

4.2.2 Enrichment for extracellular matrix component factors in HER2+ breast cancer brain metastases

Struck by the spheroidal growth exhibited by HER2+ models, we wondered what might be driving this clustering phenotype and if this configuration conferred a survival advantage for the growth of these cells in the brain. We compared gene expression profiles between parental and brain-tropic metastatic derivatives from HER2+ and HER2- models to understand the spectrum of differentially expressed genes in brain metastases. In each setting, several hundred genes were identified as differentially expressed between parental and BrM derivatives **(**Figure 4-10**).** In order to deconvolute our datasets and prioritize candidate genes to study, we used a powerful bioinformatics tool called Database for Annotation, Visualization and

Integrated Discovery (DAVID) to identify over-represented gene ontology (GO) terms (Huang et al., 2009a; 2009b). Because the annotation GO terms to every known gene of the genome has been carefully curated, we can identify in an unbiased fashion molecular processes that might be over-represented in our DE genes. Interestingly, our analyses revealed an over-representation of Extracellular Matrix Organization genes in our HER2+ datasets HCC1954 and MMTV-Erbb2, which was not detected in our HER2- MDA-231 dataset **(**Figure 4-11**)**. In an orthologous manner, we used Gene Set Variation Analysis (GSVA), another bioinformatics analyses tool that computes the enrichment of a given set of genes in one sample vis-à-vis the other (Hänzelmann et al., 2013). We computed enrichment scores for our HER2+ and HER2- datasets using a previously described gene set that identifies the matrisome, the compendium of genes identified to be constituents of the extracellular matrix (Naba et al., 2012). Matrisome signature scores were heightened in HER2+ versus HER2- BrM derivatives **(**Figure 4-11).

Taken together, these strongly suggest the importance of extracellular matrix component genes in the behavior of HER2+ cancer cells in this setting. In order to identify specific candidate genes of interest, DE genes from both mouse and human HER2+ datasets were overlaid and a list of concordantly DE genes was generated **(**Figure 4-12). We further narrowed this down by integrating a clinical classifier into our filtering criteria. In an unbiased manner, we plotted relapse-free survival curves for each common DE gene using *kmplot*, which integrates microarray data and clinical information from previously published datasets (Lánczky et al., 2016). Our analysis reveals a subset of 18 genes that was predictive of poorer relapse-free survival in the HER2+ breast cancer subtype setting versus others **(**Figure 4-13, Figure 4-14**)**. In an unbiased manner, the four

upregulated genes in our analyses are constituent members of the matrisome, an ensemble of genes identified as being important for extracellular matrix and function (Naba et al., 2012). In particular, two of these genes, Tenascin C (TNC) and Collagen 4 alpha 1 (COL4A1), stand out as core components, a conserved assembly of 200 proteins integral for extracellular matrix integrity **(**Figure 4-15**)**. Given the membership of these two genes in the core compartment, we decided to investigate their functional role in HER2+ breast cancer brain metastasis.

4.2.3 Deposition of Extracellular Matrix by HER2+ Cancer Cells

How might TNC or COL4A1 help HER2+ breast cancer cells colonize the brain? The extracellular matrix is a dynamic environment whose tuning and composition can strongly influence cellular behavior (Liu et al., 2011). We looked at early time points to understand how HER2+ cells deposited their own extracellular matrix upon extravasation out of blood vessels. We noticed that as HER2+ cancer cells adopt early spheroidal growth, where less than 5-6 cell division have occurred, we readily find a deposition of cancer cell-derived TNC surrounding growing spheroids **(**Figure 4-16**)**. TNC deposition has been previously associated with increased matrix stiffness and correlates with aggressiveness in glioblastoma (Miroshnikova et al., 2016). We used atomic force microscopy in order to probe the stiffness of the brain parenchyma immediately surrounding incipient HER2+ or HER2- metastatic lesions in the brain. There was a marked increase in stiffer points found surrounding incipient HER2+ BrM spheroids compared to adjacent areas of the brain parenchyma that were not involved with metastatic cells, suggestive of changes to the extracellular matrix surrounding HER2+ cancer cells that result in stiffness increase **(**Figure 4-17**)**. In contrast, HER2- BrM cells growing in the brain parenchyma did not induce a significant change in stiffness compared to adjacent unaffected areas (Figure 4-17). TNC has been implicated as being involved in

propagation and maintenance of stem cell niches (Oskarsson et al., 2014). Given the role of TNC in maintaining stemness, we assayed HER2+ BrM cells, enriched in TNC and COL4A1 expression, for any enrichment in stemness traits. We orthotopically implanted HER2+ BrM cells versus parental cells into the mammary fat pad (MFP) of nude mice in limiting dilutions to assess the putative frequency of cancer stem cells. HER2+ BrM cells are four times more efficient at generating MFP tumors than their parental counterparts, with a putative tumor-initiating cell frequency in HER2+ BrM cells of 1/2600 versus parental cells at 1/9589 **(**Figure 4-18**)** (Hu and Smith 2009). We also find that HER2+ BrM cells are more robust at generating spheres in non-adherent oncosphere and matrigel conditions, suggestive of increased stemness capability **(**Figure 4-19**)**.

4.2.4 TNC or COL4A1 attenuation blunts metastatic outgrowth in the brain

To test the importance of TNC and COL4A1 deposition by HER2+ cancer cells, we knocked down TNC or COL4A1 in HER2+ cancer cells by shRNA and injected these into the arterial circulation of athymic nude mice. Brain metastatic outgrowth is attenuated with knockdown of either TNC or COL4A1, but does not affect lung colonization **(**Figure 4-20, Figure 4-21**)**. Attenuation of TNC or COL4A1 did not significantly change the outcome of orthotopic MFP tumor growth **(**Figure 4-22**)**. Knockdown of TNC in HER2- MDA-MB-231 metastatic cells were previously reported to be important in lung, but not in brain metastatic outgrowth in that setting (Oskarsson et al., 2011). Collectively, these data suggest a brain-tropic effect for COL4A1 or TNC knockdown in the HER2+ setting. In addition, TNC or COL4A1 knockdown blunt *in vitro* growth in oncosphere or matrigel conditions, suggesting a role for these extracellular matrix components for helping promote the stemness of these cells **(**Figure 4-23**)**. Given the striking spheroidal growth phenotype exhibited by HER2+ cancer cells as they colonize the brain, we wondered if TNC

or COL4A1 also help promote this phenotype. Although we found that TNC or COL4A1 knockdown results in a significant reduction in the number of incipient HER2+ spheroids scored at two weeks post inoculation (Figure 4-24), we were surprised to see no change in the number of vascular coopting cells**.** Puzzled, we decided to look earlier, at one-week post inoculation of these cells, and were surprised to find a preponderance of vascular cooption in HER2+ cells that had attenuated TNC or COL4A1 expression **(**Figure 4-25**)**. Taken together, this suggested to us that in the setting of HER2+ breast cancer brain metastases, prolonged vascular cooption might be detrimental to the survival of these cells, and that expression extracellular matrix component factors such as TNC or COL4A1 help HER2+ breast cancer cells maintain spheroidal morphology.

4.2.5 Extracellular Matrix Deposition Limits Immune Cell Infiltration

We posited that in the context of HER2+ breast cancer, prolonged vascular cooption might be deleterious, and serve as a means for immune cells to recognize and eliminate cancer cells. The brain is constantly surveilled for opportunistic intruders by resident and infiltrating immune cells, given its prominent role in the function of higher order organisms (Quail and Joyce, 2017). Given the hostile microenvironment of the brain, we examined if cancer cell growth induced immune cell recognition and infiltration. We stained for the major innate immune components of the stain, and found that astrocytes and microglia were strongly excluded from spheroidal-growing HER2+ metastatic lesions (Figure 4-26). In contrast, HER2- metastatic lesions that coopt and proliferate along blood vessels during their initial stages of colonization are intercalated by astrocytes and microglia (Figure 4-27). Indeed, we have previously shown that in HER2- breast and lung cancers, cells must first neutralize the detrimental effects of astrocyte interaction by secreting serpins (Valiente et al., 2014). Although HER2+ brain

tropic cells express slight levels of serpins compared to parental lines, the protective cluster configuration likely acts as a physical barrier that limits the engagement of immune sensors with growing HER2+ metastatic lesions. The core of HER2+ cell clusters are non-necrotic and are proliferative, as evidenced by Ki67 staining, a marker for proliferation **(**Figure 4-7**)**. Abrogating the ability of HER2+ cancer cells to deposit TNC or COL4A1 leads to a marked increase in the number of vascular coopting cells (Figure 4-25). CD68 has been previously described as a marker of activated microglia, usually in a state ready for phagocytosing of target cells (Fu et al., 2014; Walker and Lue, 2015). In cells that are unable to deposit TNC, we find an influx in the number of CD68+ cells surrounding cancer cells in the brain parenchyma (Figure 4-28), suggesting the decimation of these cancer cells at the hands of activated microglia. To provide evidence that CD68+ activated microglia were decimating HER2+ cancer cells that lack TNC or COL4A1 deposition, we injected TNC or COL4A1 knockdown cells and simultaneously treated mice with the microglia activation inhibitor minocycline (Fan et al., 2007; Kobayashi et al., 2013; Yrjänheikki et al., 1998). We hypothesized that if microglia were eliminating cells that lacked TNC or COL4A1 deposition, we would expect an increase in the outgrowth of vascular coopting cells. Short-term microglial inhibition by minocycline resulted in the observation of vascular-coopting cell outgrowth, which we do not typically observe at this early time point (Figure 4-29).

Collectively, our data suggest a model by which extracellular matrix deposition plays an active role in protecting HER2+ cancer cells from microglial-mediated decimation (Figure 4-30). HER2+ cancer cells predominantly adopt a spheroidal growth configuration as they generate incipient micrometastases in the brain, and this phenotype is protective for these cells. First, it acts as a physical barrier to prevent microglial access to cancer cells, which lead to their demise. Second, we

make a surprising finding that in the context of HER2+ cancer cells, prolonged engagement of vascular cooption, while important for initial metastatic outgrowth, can be detrimental to these cells because they become accessible to microglia. Inhibition of microglial activation by minocycline treatment results in the survival of vascular coopting HER2+ cells, and allows for their growth along blood vessels.

Chapter 4.3 Conclusions and Discussion

There is an immediate unmet need for understanding the progression of HER2+ breast cancer to the brain, the final frontier for patients living with this particular disease. Multiple lines of evidence from the literature are accompanied by the general belief from clinicians about HER2 being different from other breast cancers in their progress towards brain metastases, without being able to fully articulate what this difference might be.

Our results reveal a surprising finding of extracellular matrix deposition by HER2+ breast cancer cells as being a powerful mediator of the ability of these cells to colonize the brain. As disseminated cancer cells make their way to a new organ site, they must either arrive ready react to the new microenvironment, integrating the foreign signals they find there, or build their own niche to make the new environment their own (Tammela et al., 2017; Zhang et al., 2013). As HER2+ cancer cells arrive in the brain, tumor cell secretion of TNC and COL4A1 aid in their survival by promoting the adoption of a protective spheroidal configuration by these cells. In addition to acting as a physical barrier that minimizes the interaction of HER2+ cancer cells with immune cells such as microglia, we find that early adoption of spheroidal growth is preferential for HER2+ cancer cells because prolonged vascular cooption leads to their recognition by microglia and subsequent decimation.

Even cancer cells whose brain metastatic outgrowth relies on intimate association and proliferation along blood vessels need to deal with deleterious stromal signals (Valiente et al., 2014). In the context of triple negative breast and lung cancer, serpins serve as a defense against reactive stroma. HER2+ BrM cells have little to

no expression of serpins that have been implicated in helping to cope with damaging stromal signals, reinforcing the notion that they are unable to reap the benefits of prolonged vascular cooption because of their inability to deal with exposure to these deleterious stromal signals. In the context of spheroidal cell clusters, cells that are not in direct contact with the vasculature are proliferative and viable, suggesting that these cells are able to grow even in the incipient stages of metastatic outbreak without the need for contact with the vasculature. The growth configuration of HER2+ BrM cells is reminiscent of circulating tumor cell clusters, whereby clusters leave the primary tumor to seed distant organ sites (Aceto et al., 2014). Although cells were inoculated into mice as single cell suspensions, our studies reveal a strong affinity of HER2+ cells for one another when allowed to chemotact in *ex vivo* organotypic assays. Further examination of the behavior of HER2+ cancer cells in circulation will help determine if these cells are more likely to generate *de novo* clusters while in circulation.

Extracellular matrix (ECM) deposition by cancer cells, while not a novel concept in itself, has been relatively underappreciated when it comes to its impact on cancer cell biology, especially at the metastatic site(Pickup et al., 2014). Moreover, little is known about the influence of extracellular matrix composition on immune cells and their ability to recognize and kill cancer cells. In our studies, we find a remarkable ability for TNC and COL4A1 mediated shielding of cancer cells to avoid recognition and destruction by activated microglia. Although we attribute the increase in active microglia surrounding TNC or COL4A1 depleted HER2+ cancer cells to the recognition of these cells because of vascular cooption, we cannot rule out the possibility that TNC or COL4A1 have a direct role in influencing the behavior and activity immune cells. For example, in the context of the adaptive immune response, T-cell proliferation has been shown to be negatively affected by type I

collagen through engagement of the inhibitory collagen receptor LAIR-1 (Meyaard, 2008). Finally, our findings have been largely confined to understanding the role of activated microglia in HER2+ breast cancer brain metastases; a whole spectrum of immune cells are likely coordinated during metastatic outgrowth, whose contributions to the process warrant further investigation. Neutrophils, an innate immune cell not typically present in the brain, are actively recruited by brain metastatic cells to promote their growth (Liu et al., 2013). In line with this, neutrophil chemotaxis is an enriched GO term in our HER2+ BrM datasets. A more detailed analyses of the molecular underpinnings of the interplay between HER2+ cancer cells and innate immune cells may unravel novel immune modulators to pursue in the clinic.

AdenoCa	Cell Line	Source	Mutations	Lines (Organs)
Lung	H2087	Stage I Lymph Node	$NRAS^{Q61K}$ $BRAF^{L597V}$ $p53^{V157F}$	LCC1 (Lung) LCC2 (Kidney)
Breast	HCC1954	Stage IIA Ductal Lesion	$ERBB2^{Amp}$ $PI3K^{H1047R}$ $p53^{Y163C}$	LCC1 (Brain) LCC2 (Brain)

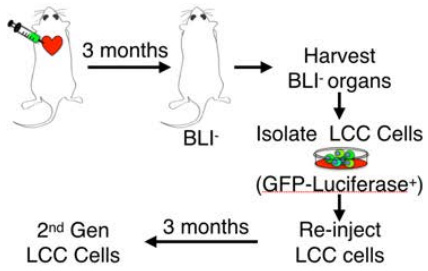

Figure 3-1. Characteristics of cancer cell lines used in these studies, and an overview of the *in vivo* selection strategy for the generation of LCC cells.

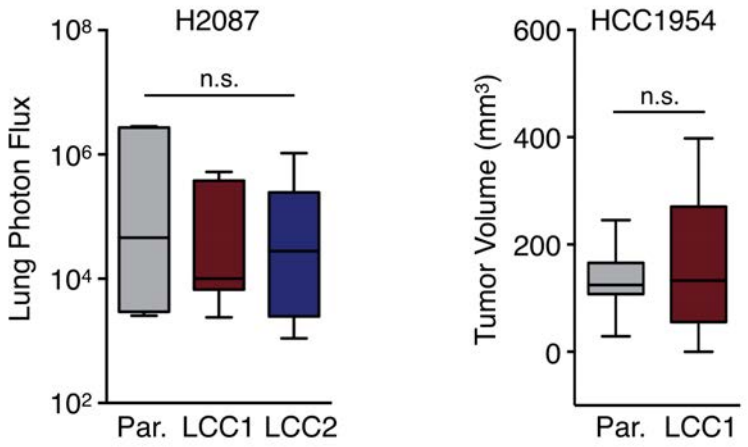

Figure 3-2. Orthotopic lung implantation of H2087 parental and LCC derivatives and orthotopic mammary fat pad implantation of HCC1954 parental and LCC derivatives.
Lung data are normalized photon flux 2 months post-injection.
N = 5 mice per group. H2087 data: Malladi
Mammary fat pad tumor volumes were measured by digital caliper measurement 44 days post-implantation.
N = 10 tumors per group. HCC1954 data: Macalinao
Whisker plots represent minimum and maximum values, n.s. = not significant

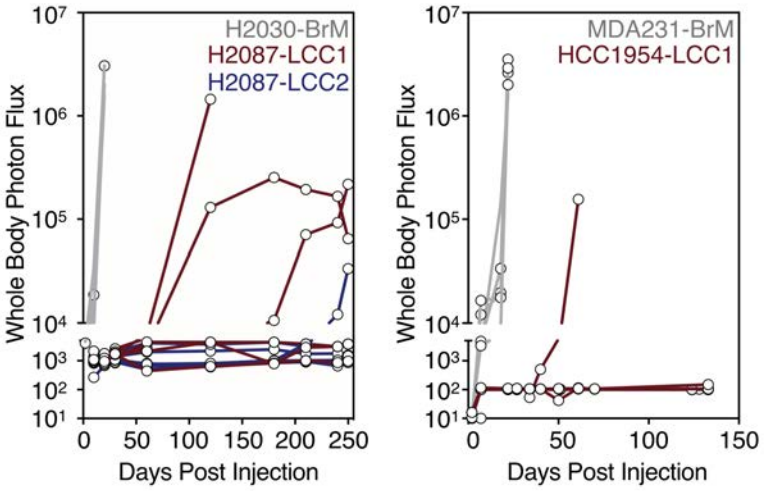

Figure 3-3. Bioluminescence imaging signal tracking of mice injected with the indicated cell lines. Each line represents an individual mouse.
H2087 LCC lines N = 20, HCC1954 LCC line N = 8
H2087 data: Malladi, HCC1954 data: Macalinao

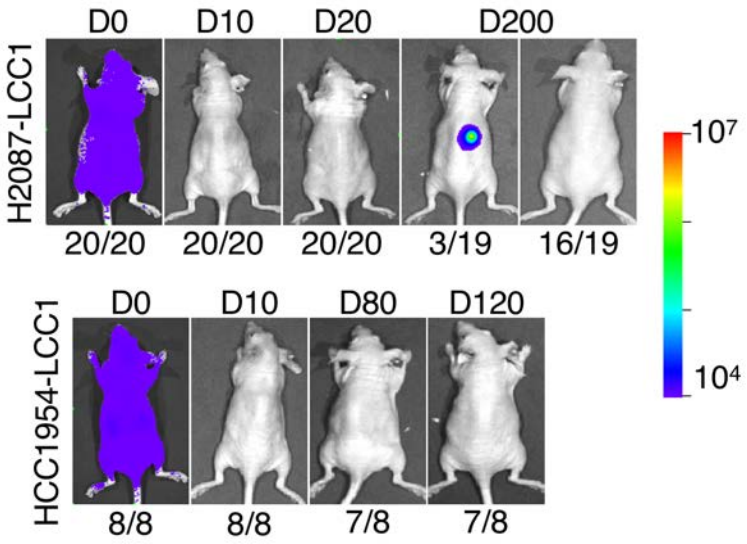

Figure 3-4. Representative BLI images of mice injected with H2087 or HCC1954 LCC cell lines.
H2087 data: Malladi, HCC1954 data: Macalinao

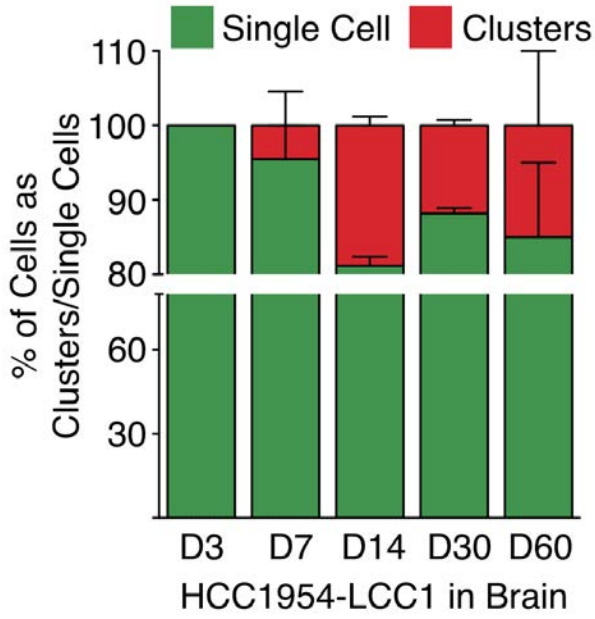

Figure 3-5. Quantification of HCC1954-LCC1 cancer cells in the brain found as single cells or in clusters over the indicated time period. Data are percentage of either single-cell or cell-cluster events per brain. N = 2 – 5 mice per group, scoring representative serial sections of the entire brain for each mouse.

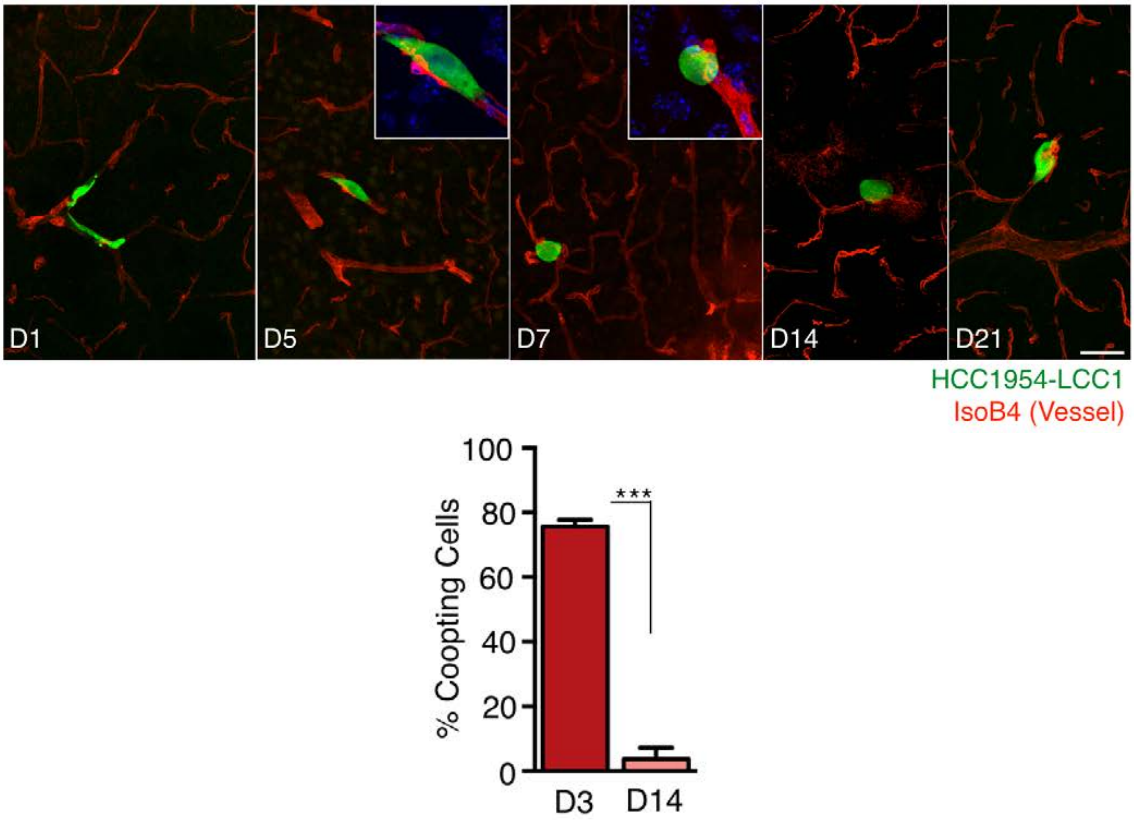

Figure 3-6. Analysis of HCC1954-LCC1 cell morphology (green) in the brain at indicated time points. Cancer cells associated with brain capillaries (red) as they extravasated and colonized the brain. Scale bar = 50um.
Quantification of HCC1954-LCC1 morphology are presented as mean percentage of coopting cells per brain. N = 3 mice per group, scoring representative serial sections of the entire brain for each mouse. *** $p < 0.001$, Student's t-test.

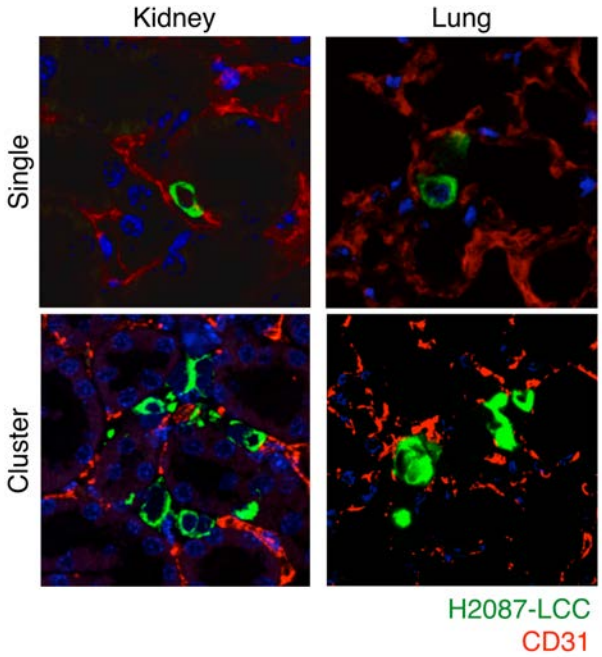

Figure 3-7. Morphology of H2087 LCC cells (green) in the kidney and the lung. Cancer cells are found to be associated with blood vessels (CD31, red) in either organ site. H2087 data: Malladi

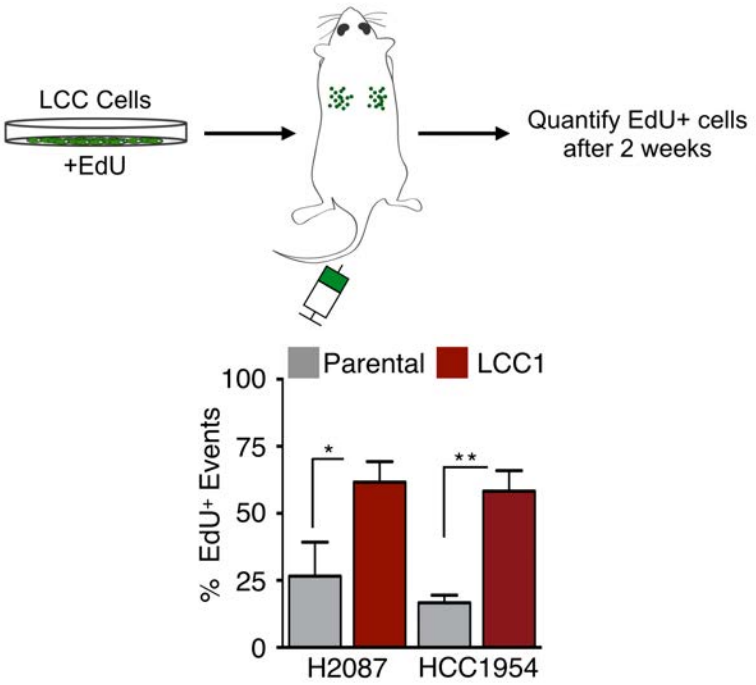

Figure 3-8. Experimental schema for EdU pulse-chase experiment. EdU labeled cells injected into the tail vein of athymic nude mice were allowed to sit for two weeks. Lungs were harvested and analyzed for the number of double positive EdU+/GFP+ cells in the lung. N = 3 mice per group, scoring representative serial sections for the entire lung of each mouse. * $p < 0.05$, ** $p < 0.01$
Data by Malladi and Macalinao

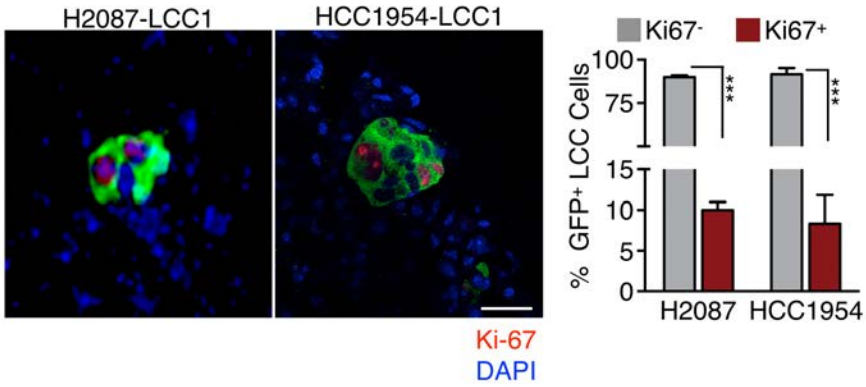

Figure 3-9. Quantification of Ki67+ proliferating LCC cells in the lung (H2087 LCC1) or brain (HCC1954 LCC1) of athymic mice 3 months post-injection. N = 5 mice per group, scoring representative serial sections of the entire organ of each mouse. *** $p < 0.001$. Scale bar = 15 um.
Data by Malladi and Macalinao

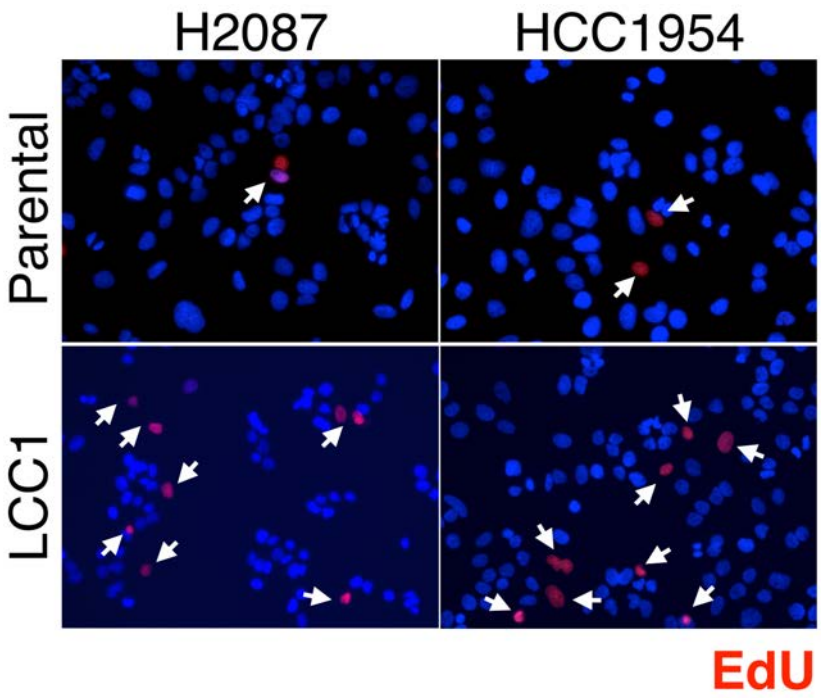

Figure 3-10. Micrographs of indicated cell lines in MLM culture 96 hours post EdU labeling. White arrows point to cells retaining EdU label.
Data by Malladi and Macalinao

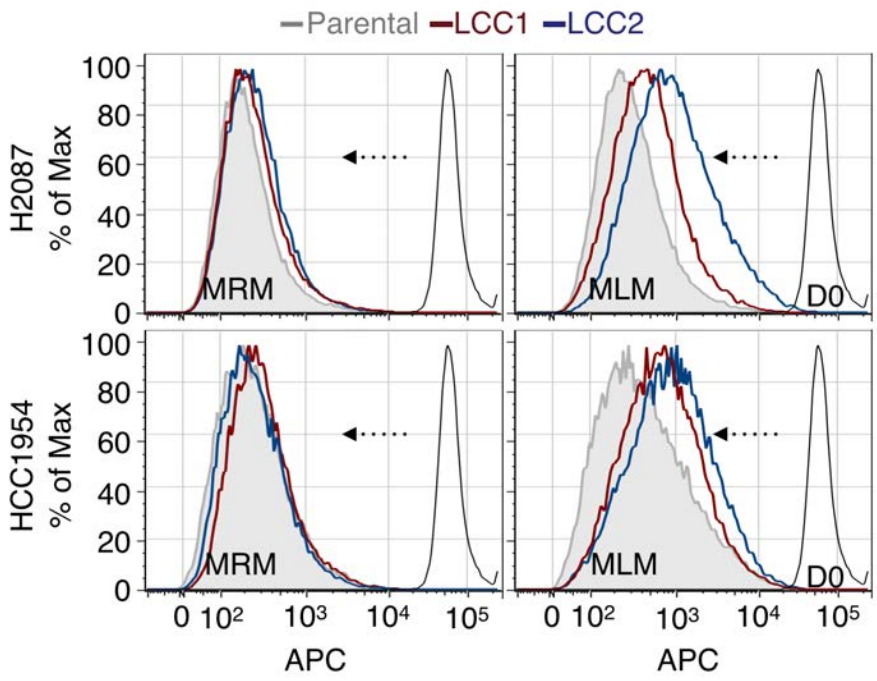

Figure 3-11. Dilution of Cell Proliferation Dye eFluor670 in indicated cancer cell lines after culture for 6 days in either mitogen rich media (MRM) or mitogen low media (MLM) culture conditions. Parental at 6 days indicated as grey shaded curve, with LCC lines superimposed on top as red or blue unshaded curves.
Data by Malladi and Macalinao

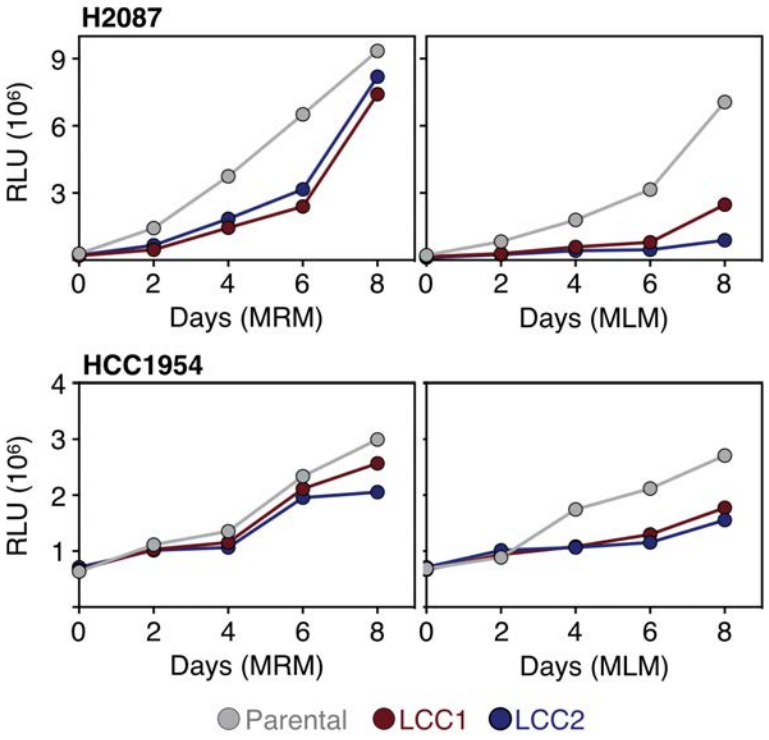

Figure 3-12. Proliferation of H2087 and HCC1954 derivatives by CellTiter-Glo over the course of 8 days under MRM or MLM culture conditions.
H2087 data: Malladi, HCC1954 data: Macalinao

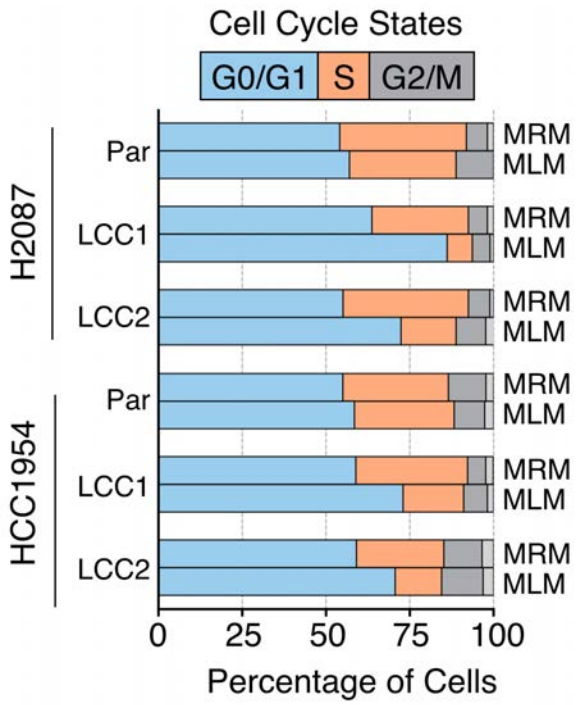

Figure 3-13. Cell-cycle analysis of the indicated cell lines by BrdU/APC after 3 days in MRM or MLM culture conditions.
Data by Malladi and Macalinao

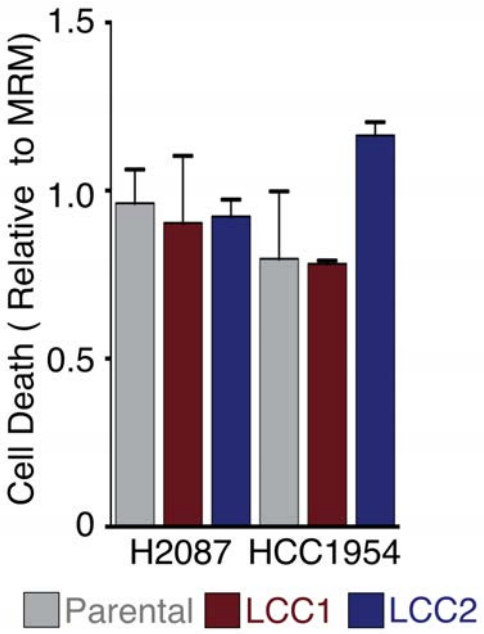

Figure 3-14. Quantification of cell death after 4 days of *in vitro* culture assayed by Caspase-Glo 3/7 in HCC1954 or H2087 derivatives grown in MLM or MRM growth conditions. Cell death ratio is MLM caspase-glo activity relative to MRM caspase-glo activity. n = 3 technical replicates.
Data by Malladi and Macalinao

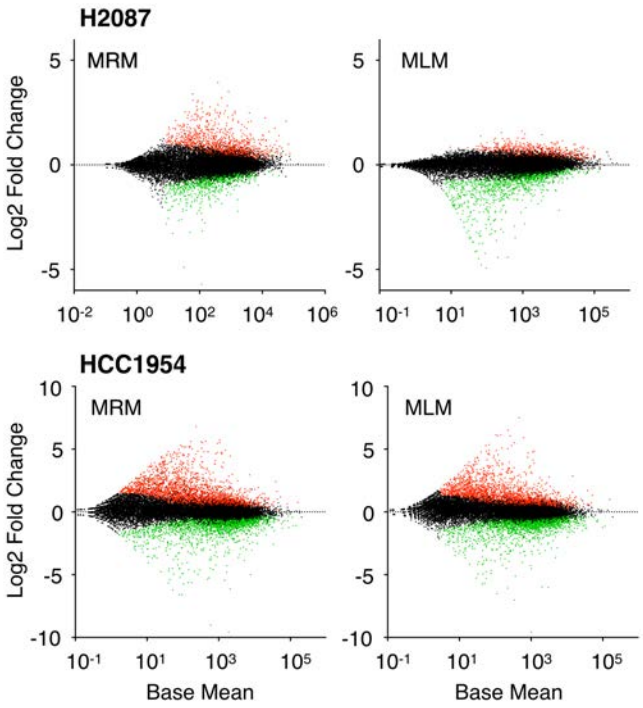

Figure 3-15. MA plot of $\log_2$ fold change and average base mean (normalized counts) in H2087 and HCC1954 LCC cells compared to parental populations under MRM and MLM culture conditions. H2087: 3 parental and 6 LCC cell samples profiled. HCC1954: 3 parental and 4 LCC cell samples were profiled.

Gene Set	N.E.S	FDR q-val
Br. Ca 20q12-q13	5.68	<0.0001
HCP - H3K27me3	4.37	<0.0001
Hu ES SUZ12 targets	3.9	<0.0001
Mammary Stem Cell	**3.89**	**<0.0001**
HCP - HK327me3	3.8	<0.0001
Colorectal Adenoma	3.7	<0.0001

Figure 3-16. Top-scoring gene sets enriched in HCC1954 LCC cells compared to parental cells by Gene Set Enrichment Analysis. NES = Normalized Enrichment Score.

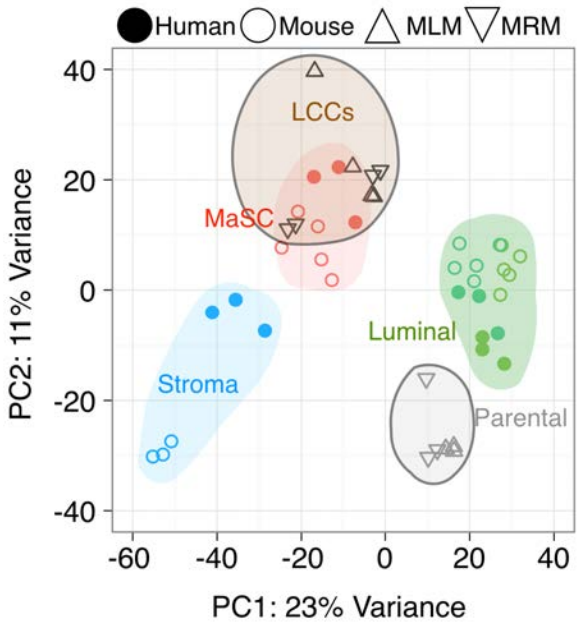

Figure 3-17. Principal Component Analyses (PCA) plot of HCC1954 derivatives under MLM or MRM conditions integrated with transcriptomic profiles derived from normal breast cell populations of human or mouse origin .
Data collected by Macalinao; PCA analyses by Jin, X.

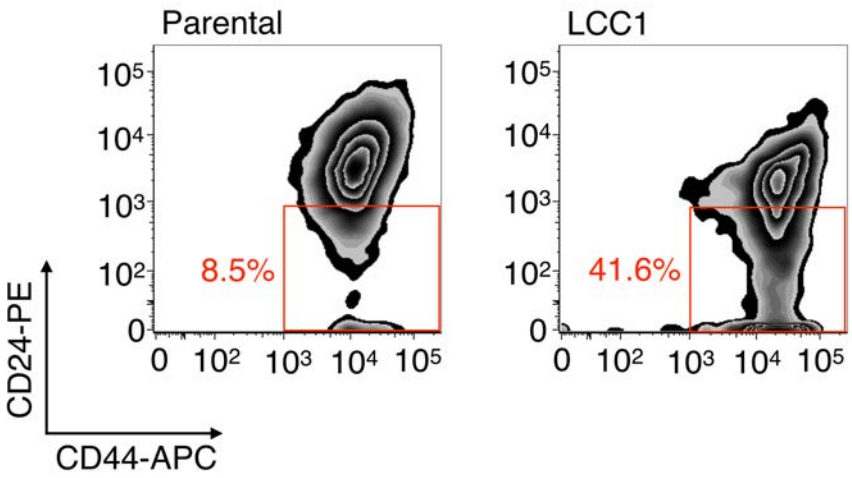

Figure 3-18. Flow cytometry analyses of CD24 (PE) and CD44 (APC) markers in HCC1954 derivatives. Red box highlights the putative $CD44^{hi}/CD24^{lo}$ population.

Cell Line	% Engraftment		
	Cells per injections		
	100K	10K	1K
H2087 - Par.	100	50.0	8.3
H2087 - LCC1	100	58.3	33.3
H2087 - LCC2	100	75.0	25.0
HCC1954 - Par.	100	33.3	0.0
HCC1954 - LCC1	100	66.7	16.7

Figure 3-19. H2087 and HCC1954 derivatives implanted into NSG mice. Percent engraftment in mice is indicated
H2087 data: Malladi, HCC1954 data: Macalinao

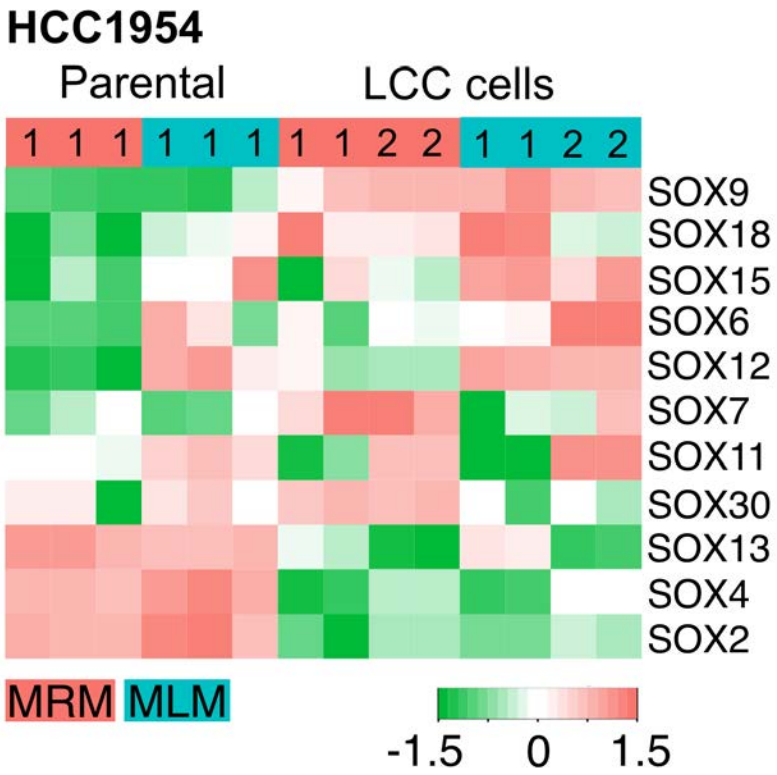

Figure 3-20. Expression of Sox family transcription factors in HCC1954 derivatives in MRM or MLM culture conditions by RNA-seq. N = 3 technical replicates of parental lines, and 2 technical replicates of LCC1 and LCC2.

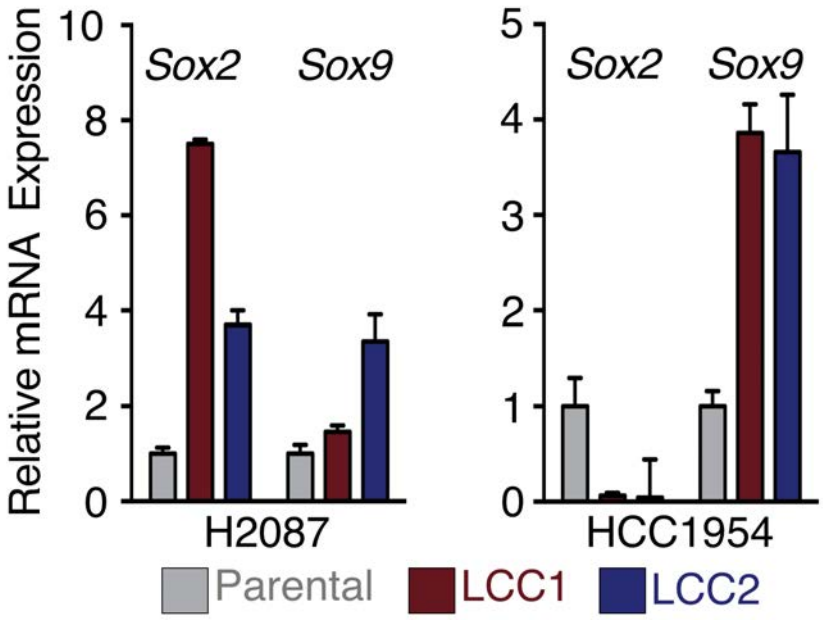

Figure 3-21. *Sox2* and *Sox9* expression mRNA expression by quantitative RT-PCR in H2087 and HCC1954 derivatives.
H2087 data: Malladi, HCC1954 data: Macalinao

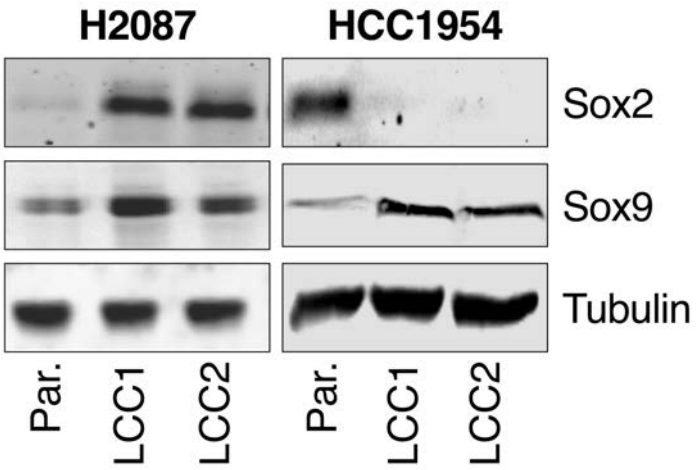

Figure 3-22. Sox2 and Sox9 protein expression in H2087 and HCC1954 derivatives. H2087 data: Malladi, HCC1954 data: Macalinao

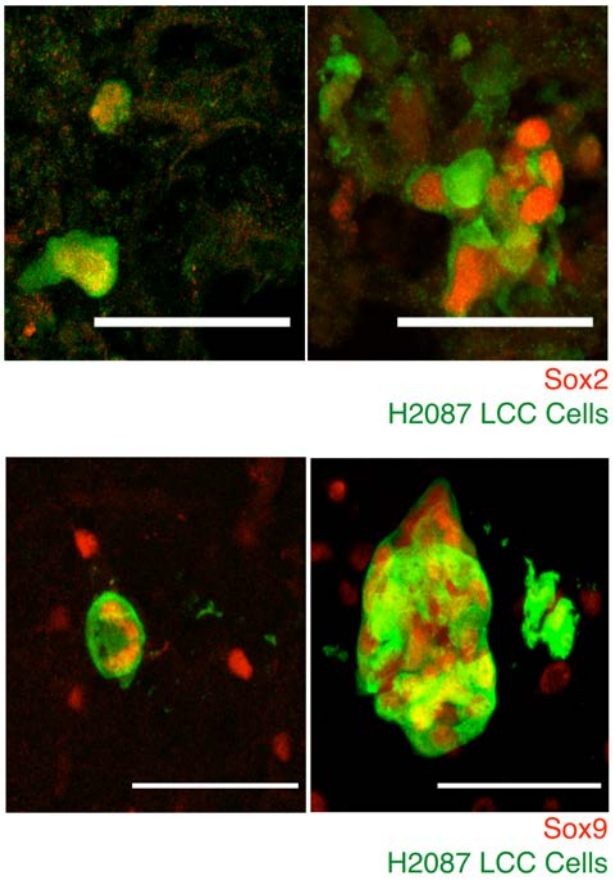

Figure 3-23. Representative single cell and micrometastatic cell cluster of SOX2+ H2087 LCC cells in the lung or SOX9+ HCC1954 LCC cells in the brain. Scale bars = 50um

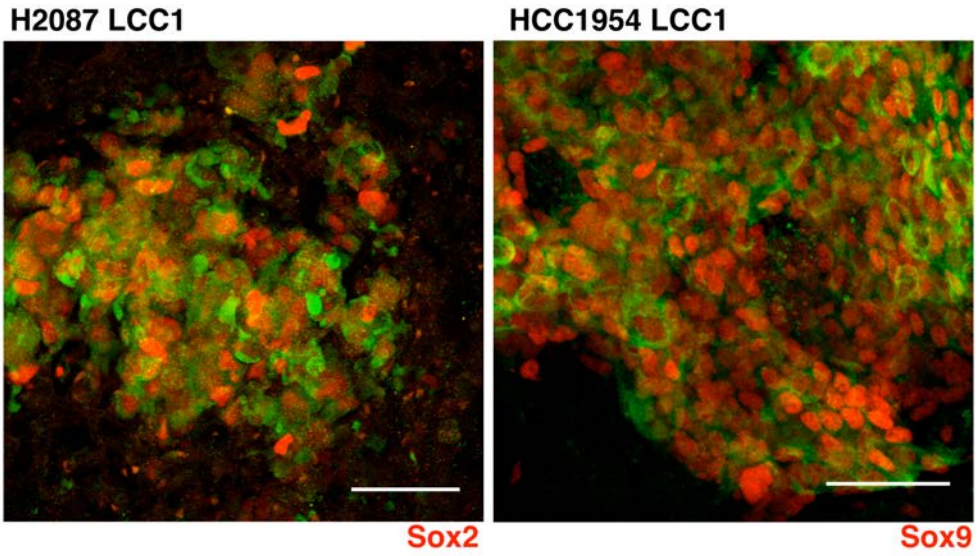

Figure 3-24. Representative Sox2 staining in the lung of NSG mice injected with H2087 LCC1; Representative Sox9 staining in the brain of NSG mice injected with HCC1954 LCC1. Scale bars = 50um

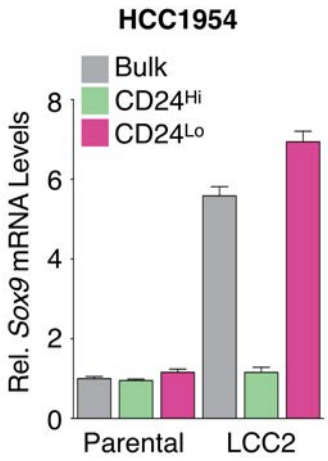

Figure 3-25. Relative Sox9 mRA expression in HCC1954 derivatives sorted for CD24 content by magnetic bead isolation. n = 4 technical replicates

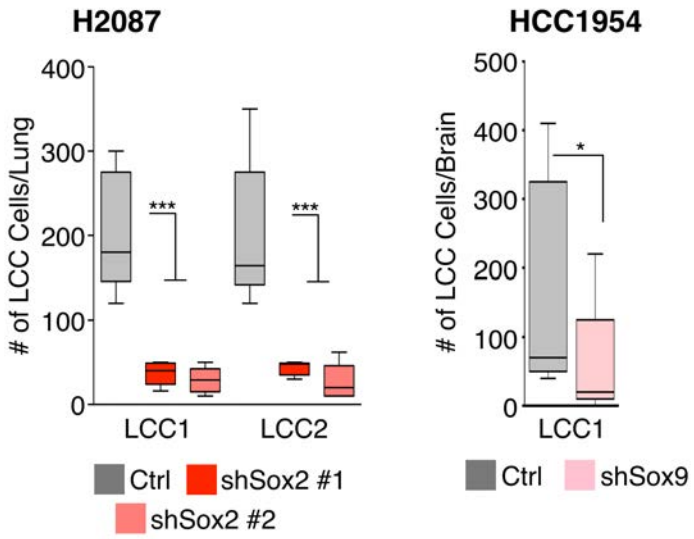

Figure 3-26. Sox2 (H2087) or Sox9 (HCC1954) depletion attenuates LCC cell survival in the lungs (H2087) and brains (HCC1954) of athymic nude mice. Data are total number of LCC cells scored in the lungs 3 months post-injection or in the brain 2 months post-injection. N = 5-6 mice, per group, scoring representative serial sections from each organ. * $p < 0.05$, *** $p < 0.001$
H2087 data: Malladi, HCC1954 data: Macalinao

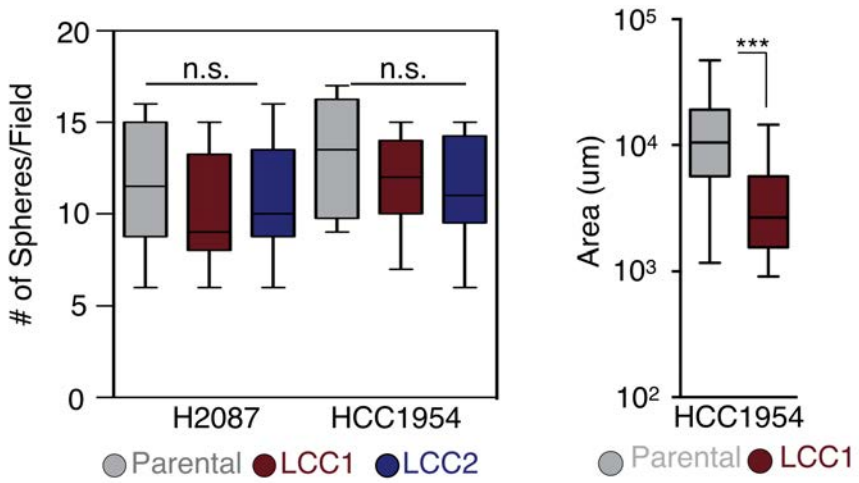

Figure 3-27. Left panel: Quantification of oncospheres generated by H2087 and HCC1954 derivatives after 14 days of growth *in vitro*. n.s. = not significant
Right panel: Oncosphere size quantification of HCC1954 parental and LCC1 cells after 2 weeks of growth *in vitro*. *** $p < 0.001$

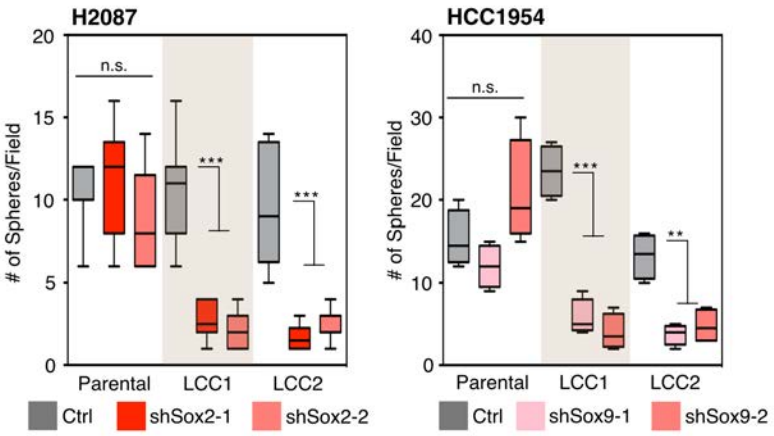

Figure 3-28. Oncosphere-forming ability of H2087 or HCC1954 derivatives after SOX2 or SOX9 depletion by shRNA respectively. n = 3 technical replicates per group
** p < 0.01, *** p <0.001, Student's t-test
H2087 data: Malladi, HCC1954 data: Macalinao

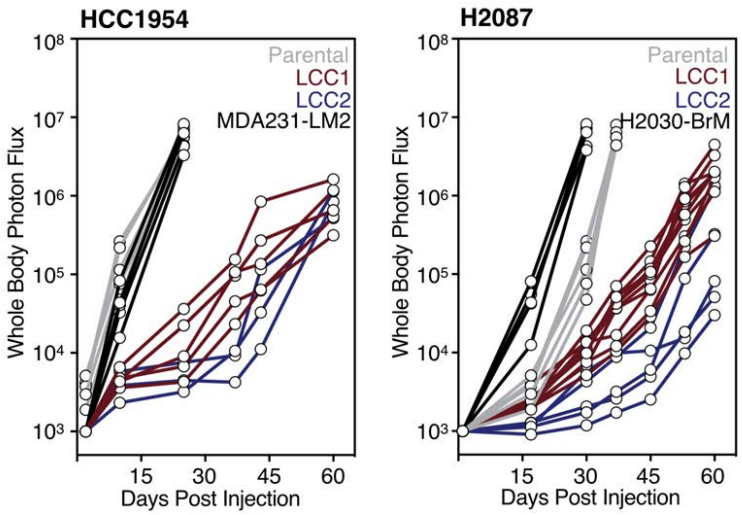

Figure 3-29. BLI tracking of NSG mice injected with indicated cell lines. Each line represents one mouse tracked over a period of 60 days.
N = 5 – 8 mice per indicated cell line
H2087 data: Malladi, HCC1954 data: Macalinao

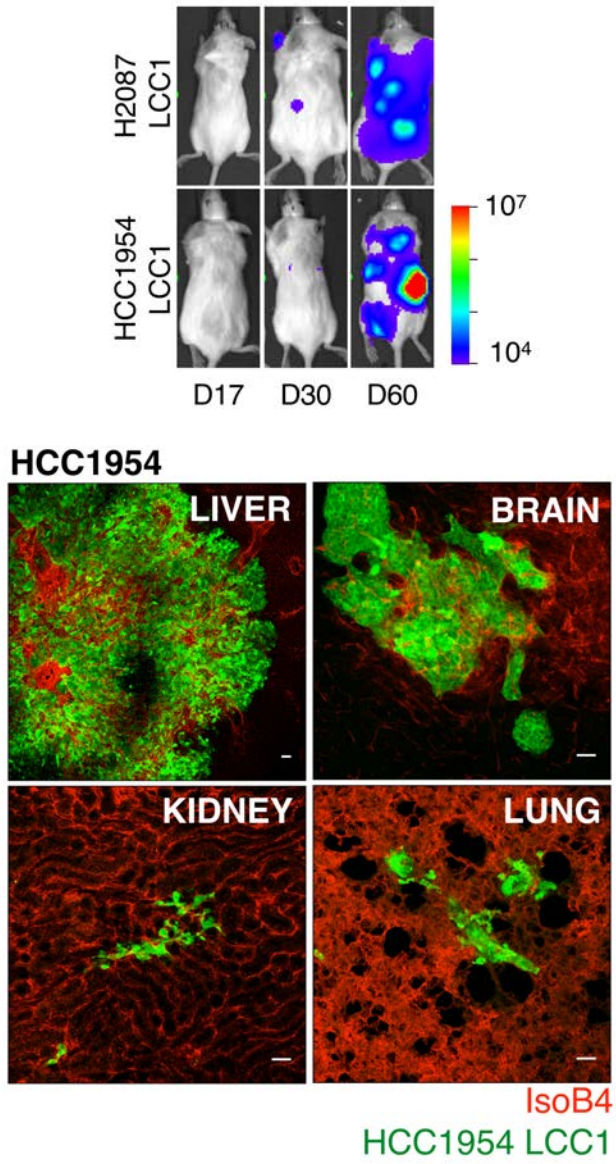

Figure 3-30. Left panel: Representative BLI images of NSG mice injected with LCC cells at indicated time points. Right panel: Representative micrographs of metastatic outgrowth in NSG mice injected with HCC1954 LCC1 in the brain, liver, kidney and lung. Vasculature labeled with Isolectin-B4 (IsoB4).
Scale bars = 100um

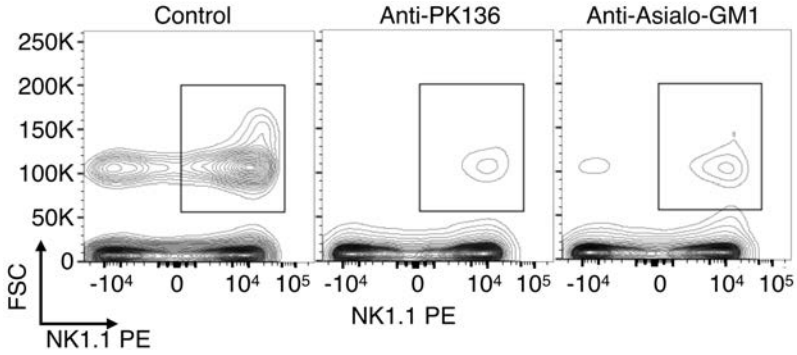

Figure 3-31. Flow cytometry analysis of lymphocytes collected from peripheral blood of control mice or those treated with NK-cell depletion regimen anti-PK136 or anti-asialo-GM1. Lymphocytes stained with NK1.1-PE.

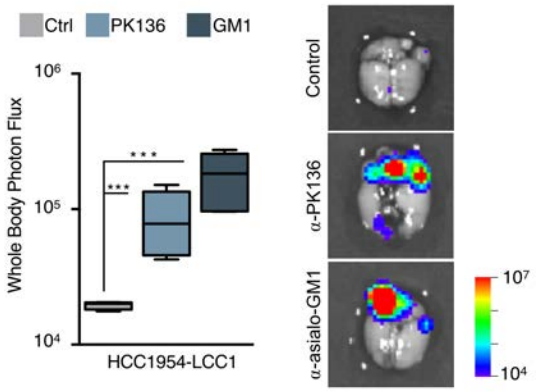

Figure 3-32. Left panel: Depletion of NK cells by either anti-NK1.1 (PK136) or anti-asialo-GM1 antibody regimen in athymic nude mice inoculated with HCC1954 LCC1 cells. Outgrowth quantified by whole body photon flux at 60 days post injection, with whisker plots representing minimum and maximum values. n = 5 -7 mice per group. *** $p < 0.001$.
Right panel: Representative BLI images of brains from mice treated with NK cell depletion regiments.

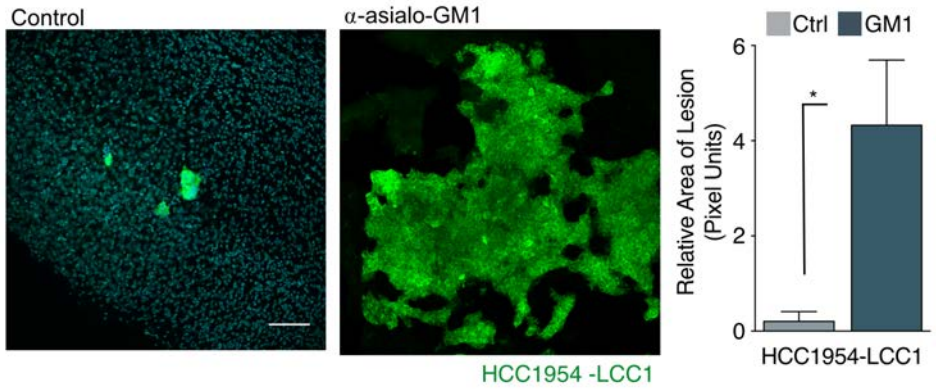

Figure 3-33. Left panel: Representative micrographs of HCC1954 LCC1 cells in the brains of mice with intact NK cells (Control) or treated with the NK depletion regimen anti-asialo-GM1. Right panel: Quantification of relative mean area of metastatic lesions. N = 3 mice per group, scoring representative serial sections of the entire brain for each mouse. * < p 0.05
Scale bar = 100um

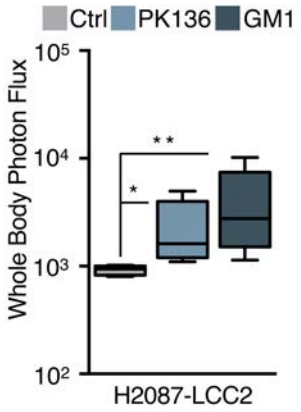

Figure 3-34. NK cell depletion in athymic nude mice injected with H2087 LCC cells. Whole body photon flux at 60 days post-inoculation, with whisker plots representing minimum and maximum values. n = 5 – 7 mice per group
* p< 0.05, ** p < 0.01
H2087 data: Malladi

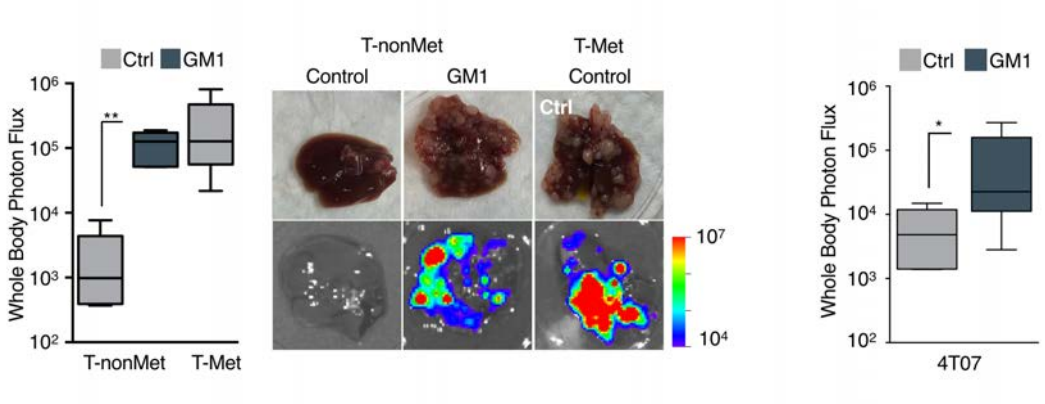

Figure 3-35. Left panel: NK cell depletion by anti-asialo GM1 in B6129SF1/J mice injected with T-nonMet lines. Outgrowth quantified by whole body photon flux 30 days post-injection. n = 5 -7 mice per group. Right panel: NK cell depletion by anti-asialo GM1 in BaLB/cJ mice injected with the non-metastatic cell line 4T07. Data are whole body photon flux 60 days post-injection. n = 5 mice per group
Whisker plots representing minimum and maximum values, * $p < 0.05$, ** $p < 0.01$
T-nonMet/T-Met data: Malladi, 4T07 data: Macalinao

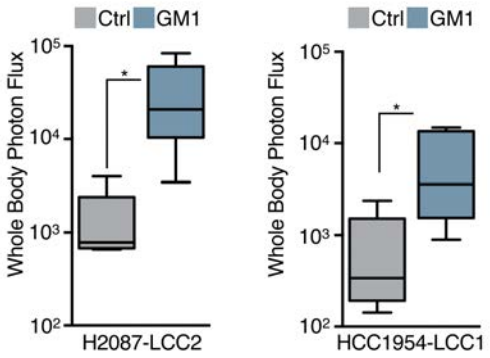

Figure 3-36. NK cell depletion regimen initiated 40 days post-inoculation of H2087 or HCC1954 LCC cells into athymic nude mice. Outgrowth quantified by whole body photon flux, with whisker plots representing minimum and maximum values.
n = 5 mice per group. * $p < 0.05$

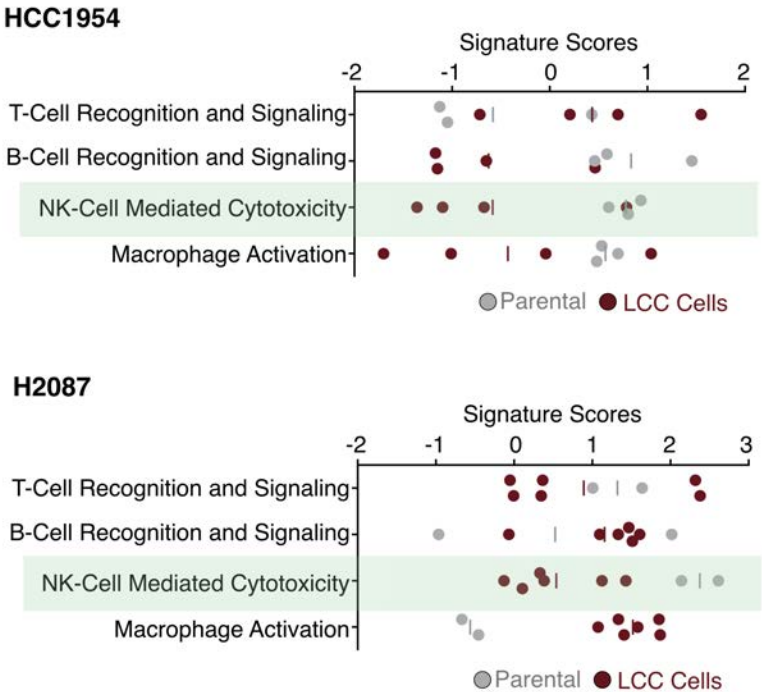

Figure 3-37. Immune-related signature scores computed by Gene Set Variation Analyses (GSVA) for HCC1954 and H2087 derivatives. HCC1954 n = 3 parental and 4 LCC cell line samples. H2087 n = 2 parental and 6 LCC cell line samples.

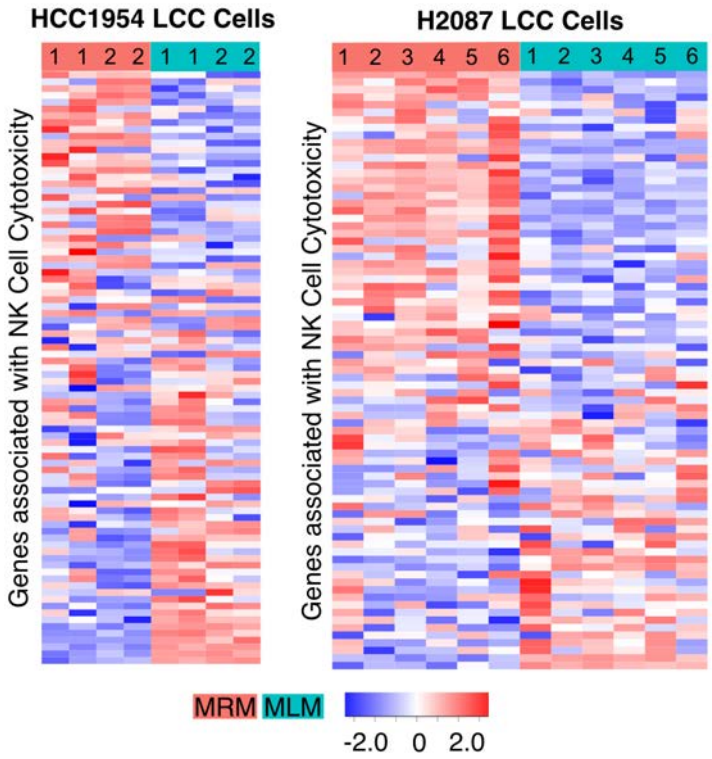

Figure 3-38. Heatmap of genes involved in NK cell mediated cytotoxicity in H2087 and HCC1954 LCC derivatives under MRM or MLM culture conditions.

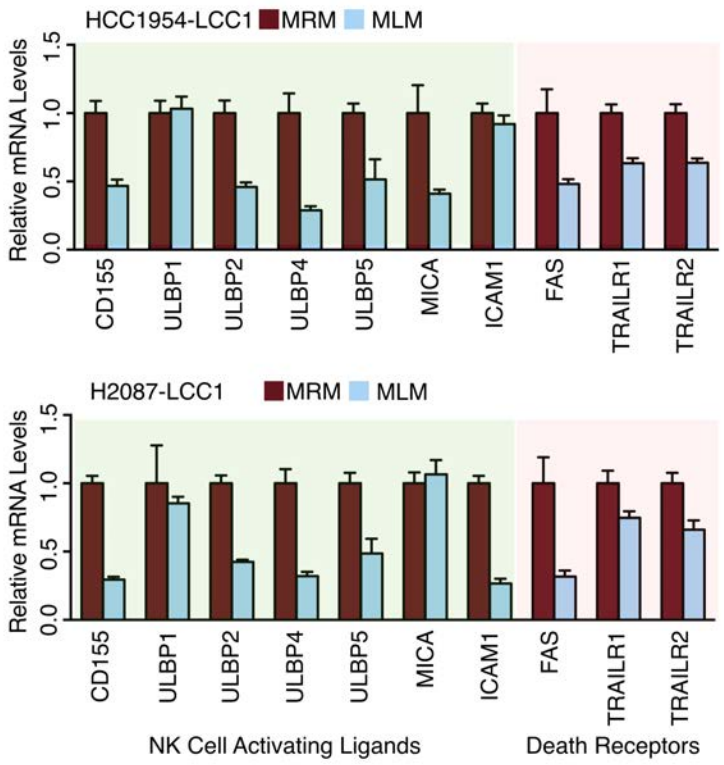

Figure 3-39. Quantitative PCR of genes important for NK cell recognition and cytotoxicity in HCC1954 or H2087 LCC cells when grown in MRM or MLM culture conditions.
H2087 data: Malladi, HCC1954 data: Macalinao

	% CD155+	
Cell lines	MRM	MLM
H2087-Par.	60.5	45.3
H2087-LCC1	45.3	**14.0**
HCC1954-Par.	41.0	38.2
HCC1954-LCC1	25.0	**11.3**

	% ULBP2/5/6+	
Cell lines	MRM	MLM
H2087-Par.	22.8	16.7
H2087-LCC1	17.8	**4.2**
HCC1954-Par.	20.5	16.0
HCC1954-LCC1	10.0	**4.8**

Figure 3-40. Cell surface expression of NK cell activating ligands CD155 and ULBP 2/5/6 in the indicated cell lines under MRM or MLM culture conditions.
Data by Malladi and Macalinao

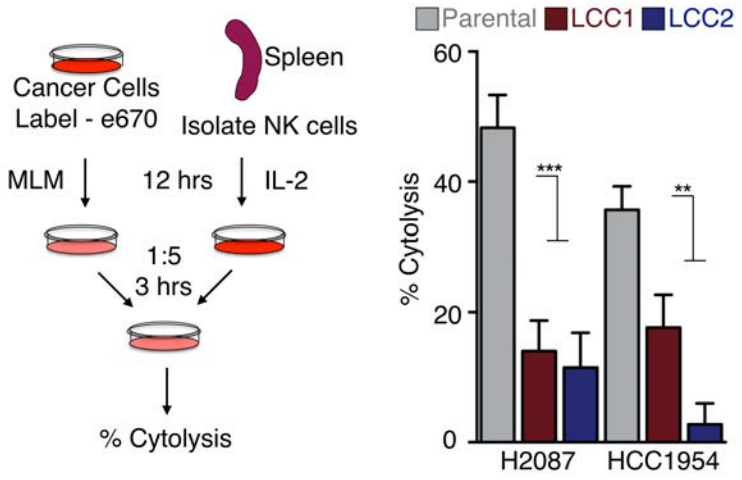

Figure 3-41. Left panel: Schematic for *in vitro* NK cell cytotoxicity assay. Right panel: Fraction of cancer cells lysed after *in vitro* co-culture with freshly activated NK cells. n = 3 technical replicates. ** $p < 0.01$, *** $p < 0.001$, by Student's t-test
Data by Malladi and Macalinao

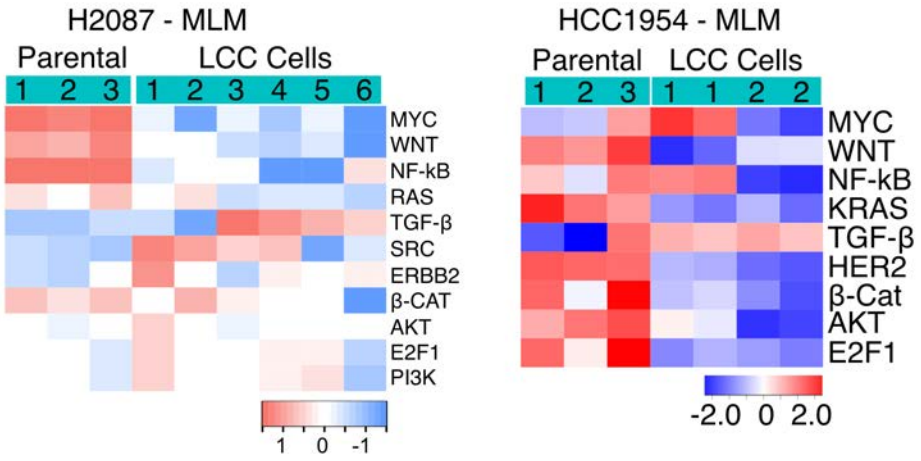

Figure 3-42. Signaling pathway classifier scores in H2087 or HCC1954 derivatives in MLM culture conditions.

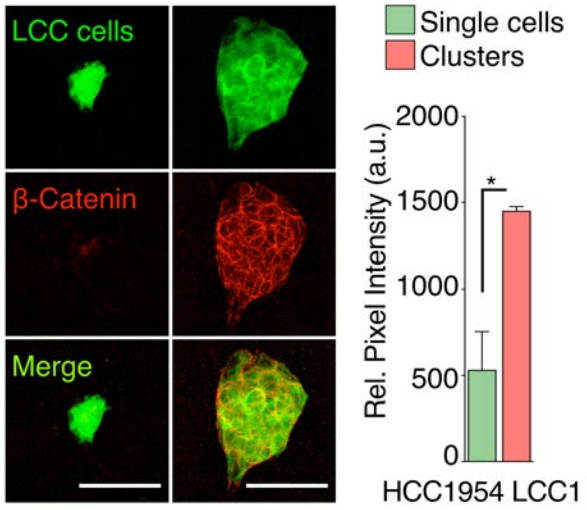

Figure 3-43. Representative immunofluorescence micrographs of single disseminated LCC cells or cell clusters in the brain stained for active β-catenin expression (red). n = 5 representative sections per condition. * $p < 0.05$, Student's t-test
Scale bars = 50 um

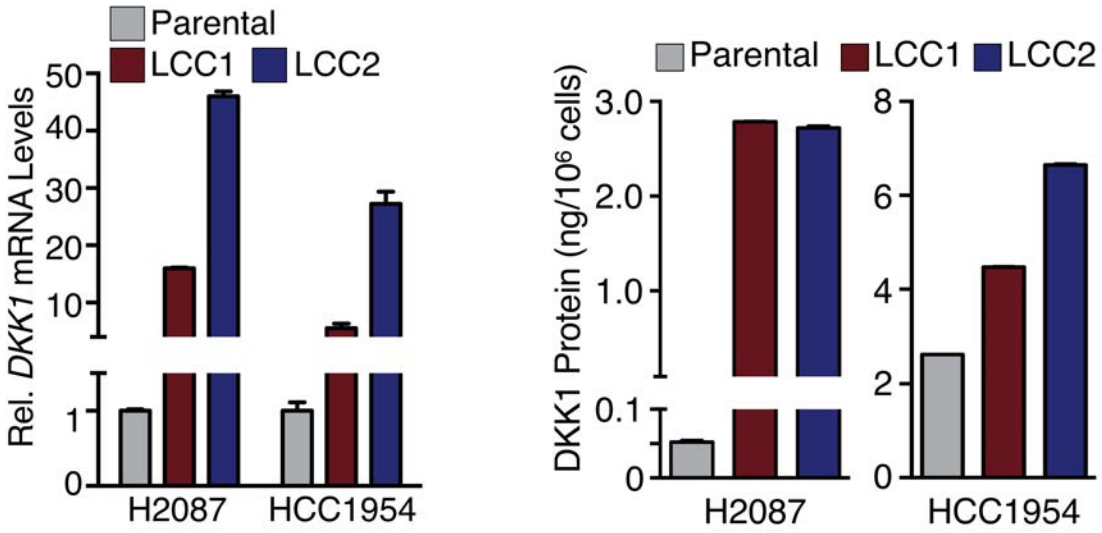

Figure 3-44. Left panel: Relative mRNA expression of DKK1 in H2087 and HCC1954 derivatives. Right panel: Detection of secreted DKK1 protein by H2087 and HCC1954 derivatives by ELISA. n = 3 technical replicates per group.
H2087 data: Malladi, HCC1954 data: Macalinao

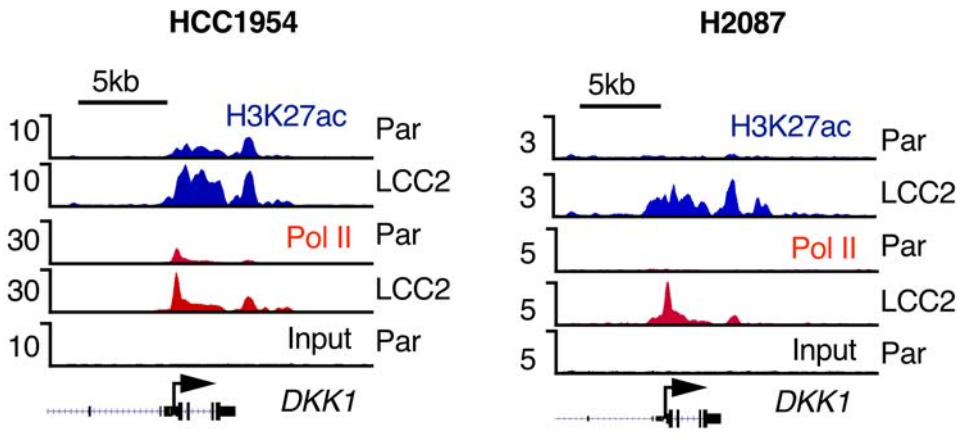

Figure 3-45. Gene track view for H3K27ac and Pol II ChIP-seq data at the DKK1 locus in HCC1954 and H2087 parental and LCC derivatives.
Data by Basnet and Zou

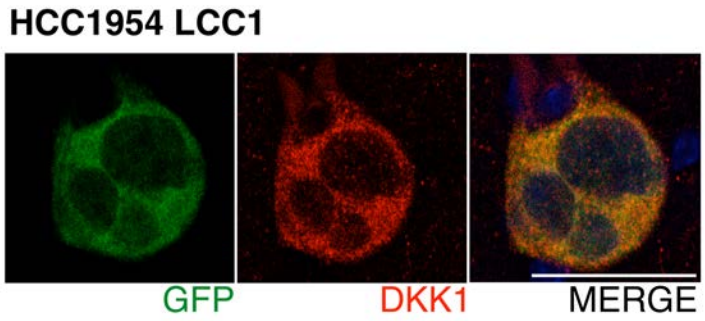

Figure 3-46. HCC1954 LCC1 cells detected in the brain parenchyma 1 month post-injection in athymic nude mic expressing DKK1 (red). Scale bar = 20um

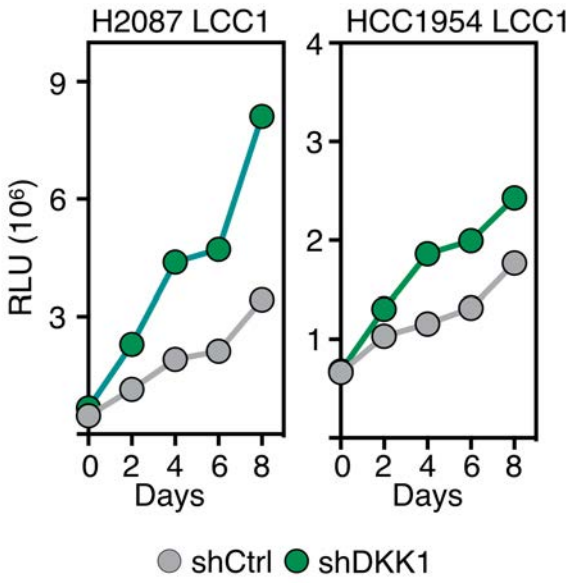

Figure 3-47. Proliferation of control or shDKK1 H2087 or HCC1954 LCC derivatives under MLM culture conditions.
H2087 data: Malladi, HCC1954: Macalinao

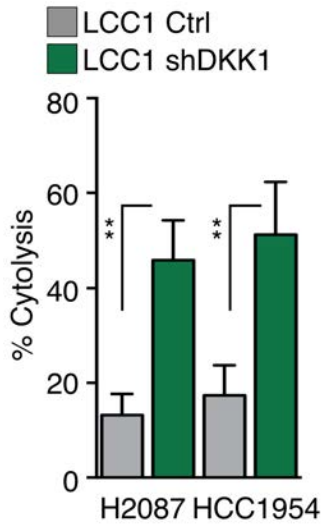

Figure 3-48. *In vitro* co-culture of activated NK cells with H2087 and HCC1954 LCC control or shDKK1 cells to determine NK cell mediated cytolysis. n = 3 replicates
** p <0.01
Data by Macalinao and Malladi

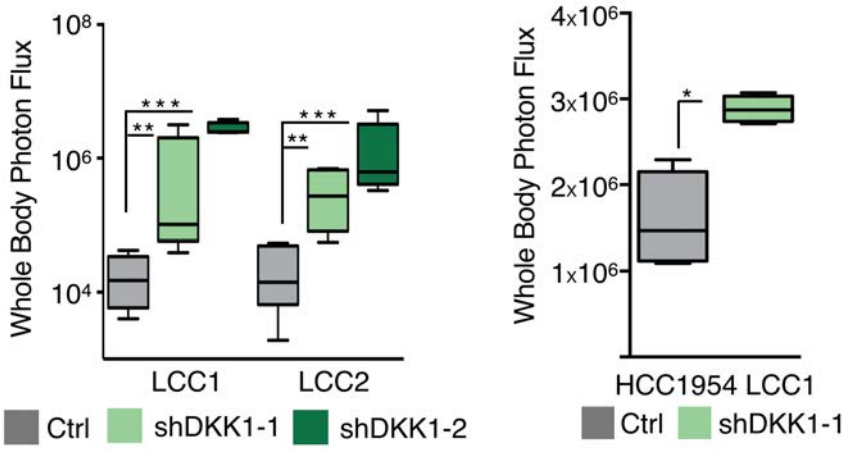

Figure 3-49. Growth of H2087 or HCC1954 LCC cells depleted of DKK1 in NSG mice. Whole body photon flux, 2 months post injection. n = 4 -6 mice per group.
* $p < 0.05$, ** $p < 0.01$, *** $p < 0.001$
Data by Macalinao and Malladi

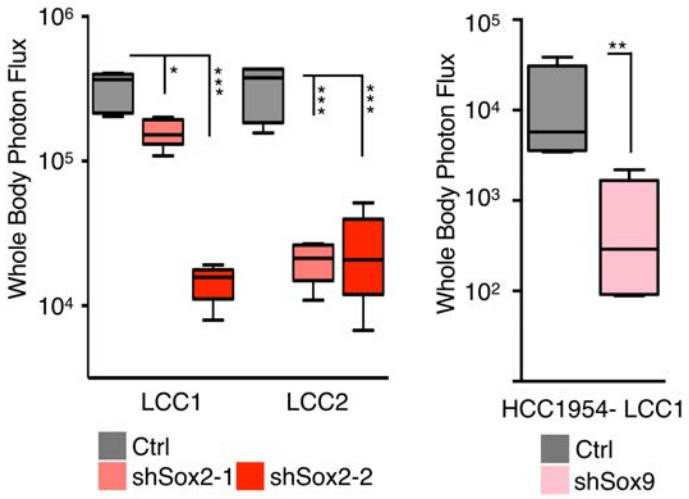

Figure 3-50. Growth of Sox2 depleted H2087 LCC cells or Sox9 depleted HCC1954 LCC cells in NSG mice. Whole body photon flux, 60 days post injection. n = 5 – 6 mice per group. * $p < 0.05$, ** $p < 0.01$, *** $p < 0.001$
H2087 data: Malladi, HCC1954 data: Macalinao

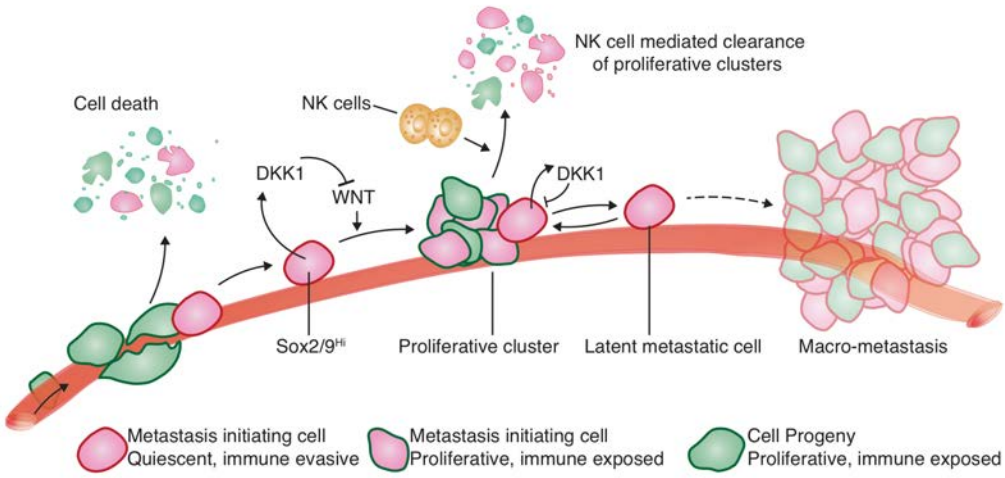

Figure 3-51. A model summarizing the central tenets of latency recapitulated in the present LCC cell models. As LCC cells attempt to infiltrate organ sites, they suffer decimation due to a myriad of factors, such as mechanical and metabolic stress, and immune surveillance. LCC cells associate with the vasculature, are enriched for Sox2/Sox9 stem-cell-like programs, stochastically enter proliferative quiescence, and are superior at seeding organs. LCC cells can proliferate in response to stimulatory microenvironmental cues after infiltrating distant organs, but NK-cell-dependent immune surveillance prevents accumulation of their progeny, sparing LCC cells that enter quiescence stochastically. Cells enriched for DKK1 are able to attenuate the proliferative response to local WNT signals, enter quiescence. Quiescent cells downregulate the expression of cell surface NK sensors to evade immune surveillance. Surviving latent metastatic cells may evolve, accumulating traits for eventual outbreak to form macrometastases.

Species	Cell Line	Ref.	Source	Mutations	Lines Derived
Human	HCC1954	Gazdar et al., 1998	Stage IIA (early) Primary Tumor	$TP53^{Y163R}$ $PIK3CA^{H1047R}$	Parental BrM2
Human	JIMT-1	Tanner et al., 2004	Stage IIIA (locally advanced) Pleural Effusion	$TP53^{R248W}$ $PIK3CA^{C420R}$	Parental BrM2
Mouse	MMTV-Erbb2	Muller et al., 1988	Primary Tumor	-	Parental BrM2

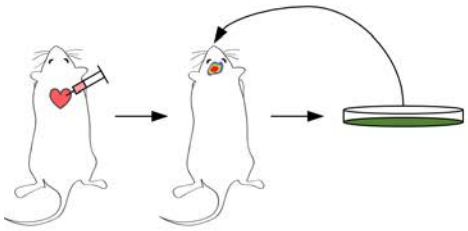

Figure 4-1. Characteristics of cancer cell lines used in these studies, and a general overview of the *in vivo* strategy to generate brain-tropic metastatic derivatives. Brain-tropic derivatives were derived by isolating *in vivo* populations of cancer cells that successfully colonized the brain and selecting for these cells *in vitro*.

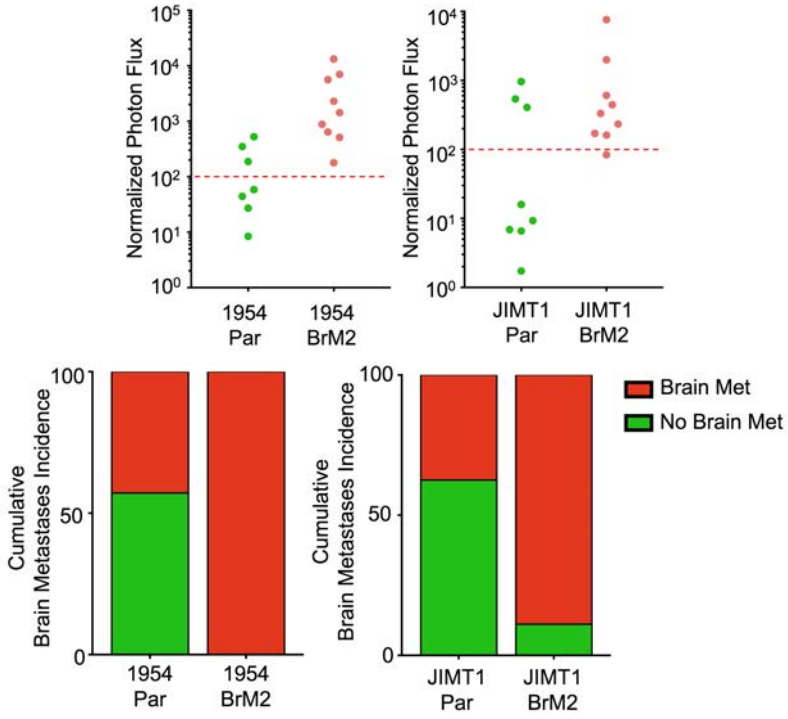

Figure 4-2. Summary of ability of brain-tropic derivatives to seed brain metastases.
Top panel: Whole body photon flux at 30 days post injection.
Bottom panel: Cumulative incidence of brain metastases at 30 days post injection.
n = 7 – 9 mice per group

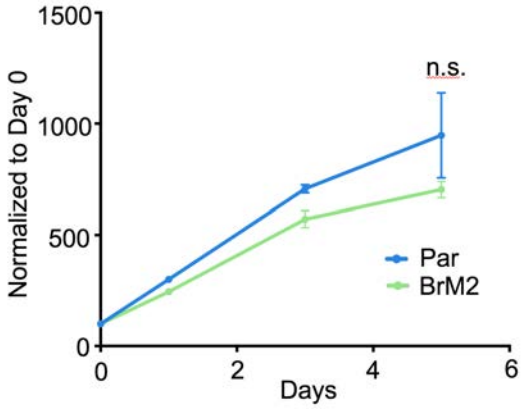

Figure 4-3. Cell Proliferation *in vitro* of indicated HCC1954 derivatives over the course of 6 days in normal culture conditions. n = 3 replicates
n.s. = not significant

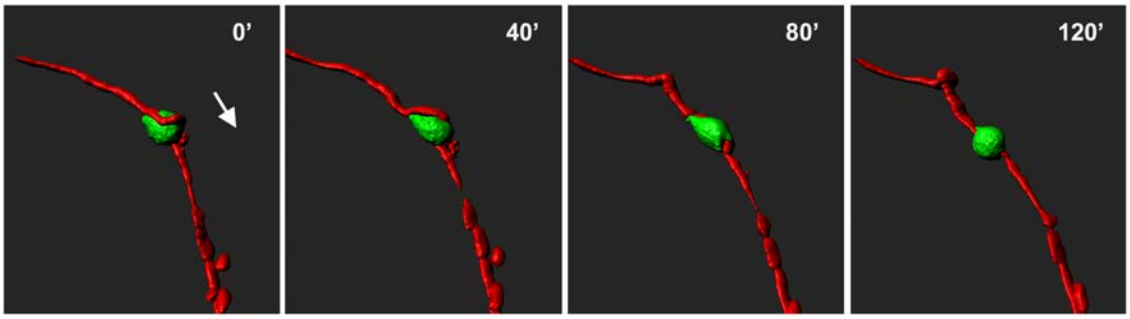

Figure 4-4. Live time-lapse microscopy of HCC1954 BrM2 cells on explant brain slices. Sample was imaged over the course of 2 hours.

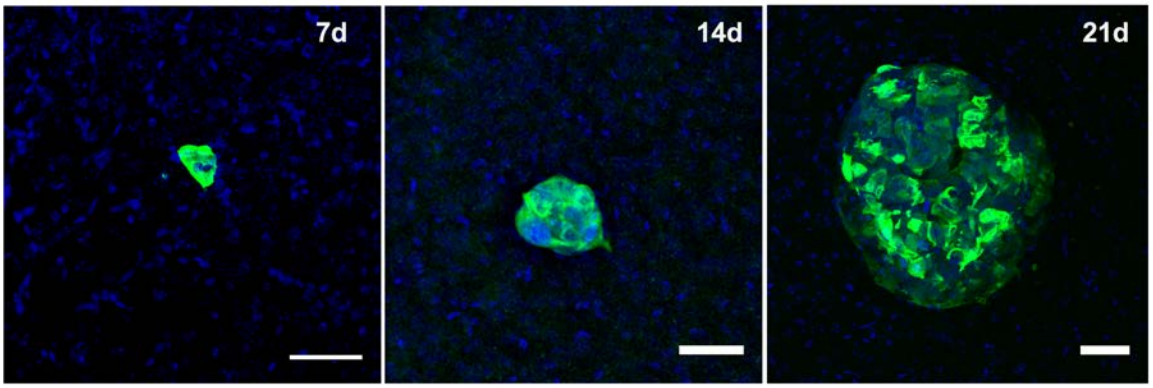

Figure 4-5. Representative micrographs at indicated timepoints of spheroidal growth configuration of HER2+ HCC1954 BrM in the brains of athymic nude mice. Counter-stained with DAPI (blue). Scale bars = 50 um

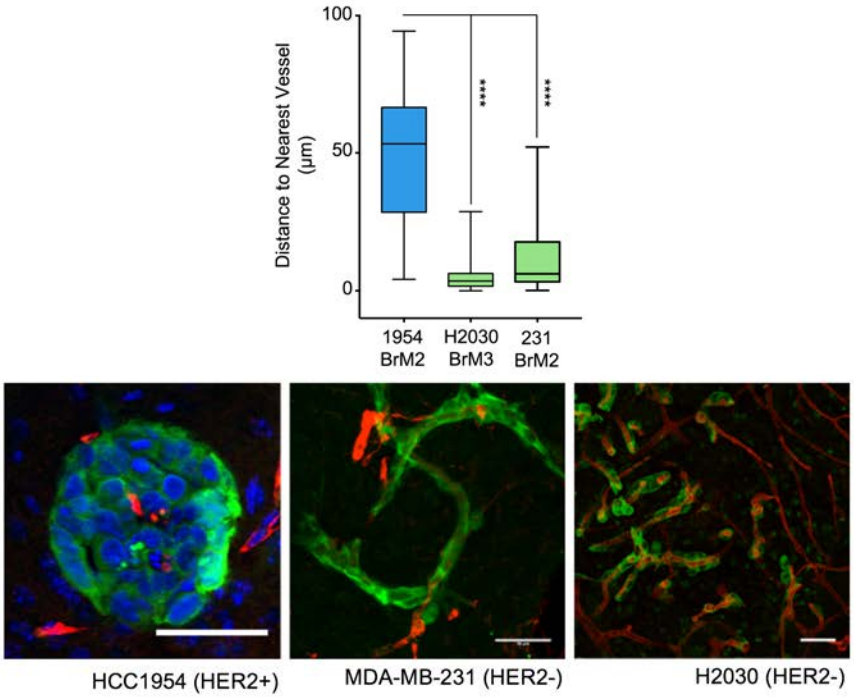

Figure 4-6. Distance measurement of cancer cells to their nearest blood vessel. n = 100 cells per group, **** $p < 0.001$

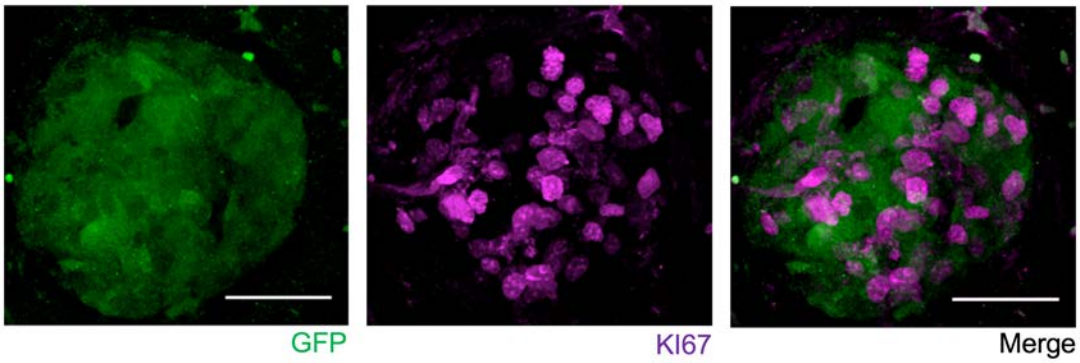

Figure 4-7. Staining of representative spheroidal HER2+ cell cluster with the proliferative marker Ki67+. Ki67+ cells are dispersed throughout the spheroidal cluster, including cancer cells that are putatively at a distance from blood vessels. Scale bars = 50 um

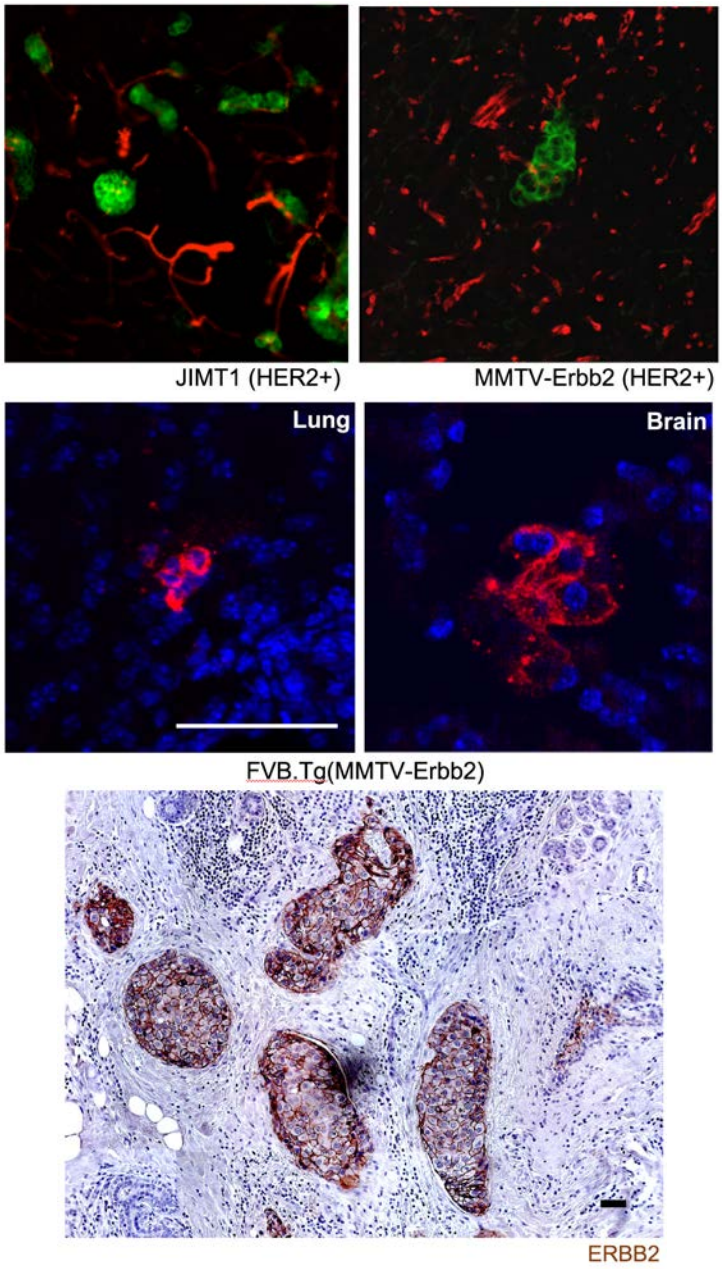

Figure 4-8. Evidence of spheroidal growth of growing metastatic lesions in multiple models of HER2+ breast cancer metastases.
Top Panel: Human JIMT1 (HER2+) or Mouse MMTV-Erbb2 (HER2+) cancer cells in the brains of athymic nude or syngeneic FVB mice respectively. Vasculature labeled with Collagen IV (red).
Middle Panel: Lung and brain micrometastases from mice that developed spontaneous mammary tumors. Cancer cells labeled with Erbb2 (red) and counter stained with DAPI (blue).
Bottom Panel: Preliminary evidence of spheroidal growth in the primary tumor of a HER2+ breast cancer patient. Paraffin sections labeled by immunohistochemistry with Erbb2 (brown).

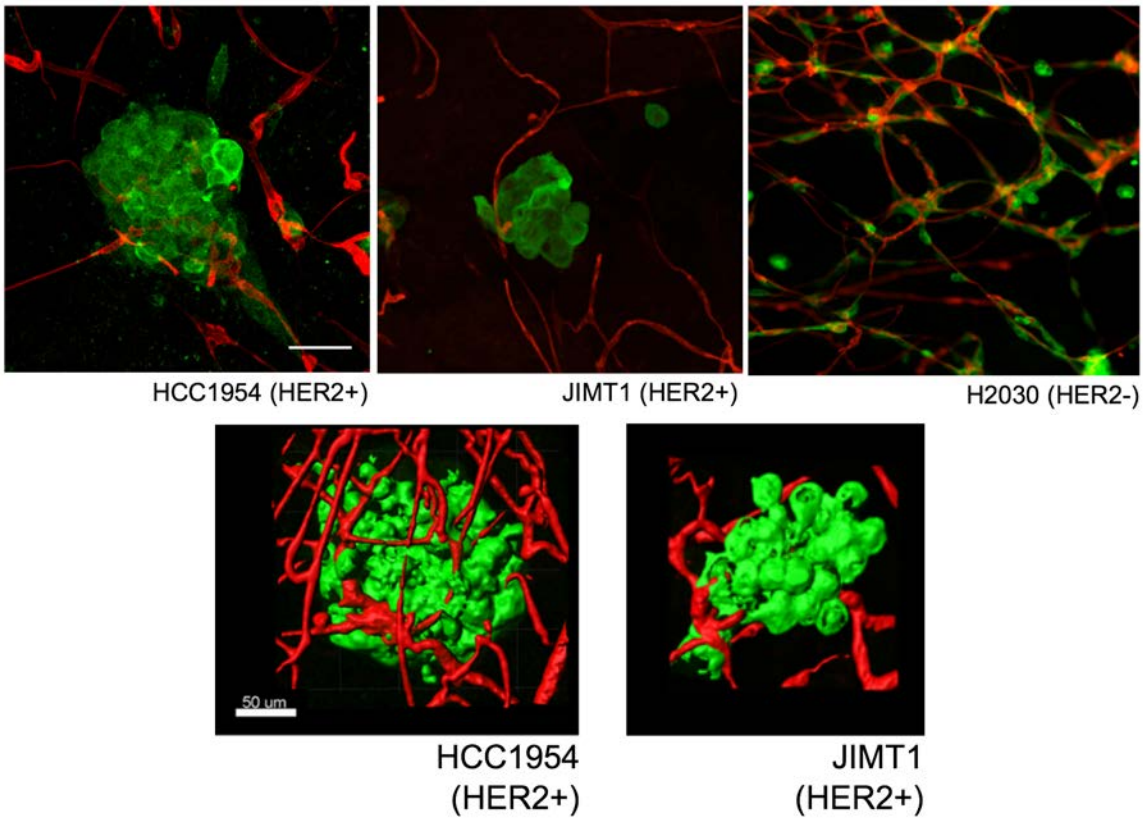

Figure 4-9. Top Panel: Representative micrographs of HER2+ or HER2- brain-tropic derivatives in explant brain slice assays. Cancer cell chemotaxis to form clusters apparent in HER2+ versus HER2- cancer cells. Vasculature labeled with Collagen IV (red).
Bottom Panel: 3D-rendering of HER2+ cancer cells in explant brain slice assays to show intercalation of these cell clusters with the underlying vasculature. Scale bars = 50 um

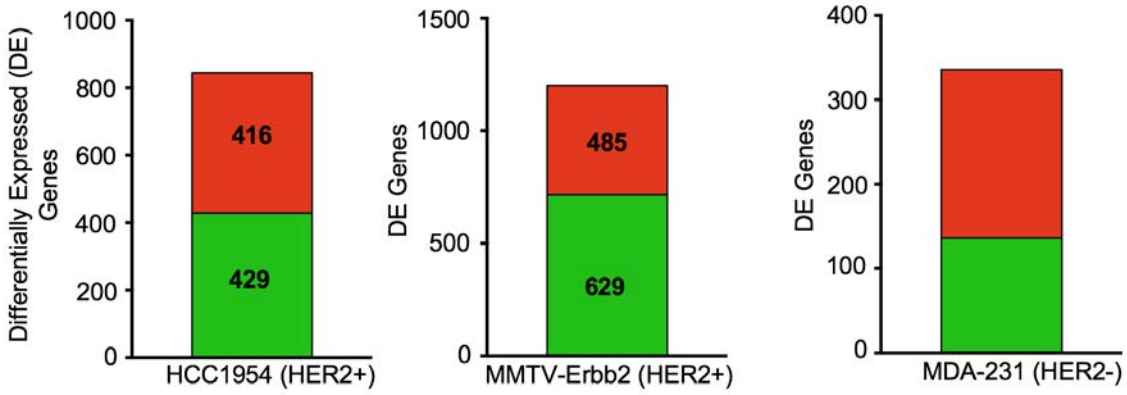

Figure 4-10. Summary of Differentially Expressed (DE) genes in HCC1954, MMTV-Erbb2, or MDA-MB-231 models comparing parental populations to brain-tropic metastatic (BrM) derivatives. HCC1954: 3 parental and 2 BrM samples profiled. MMTV-Erbb2: 3 parental and 3 BrM samples profiled. MDA-231: 3 parental and 3 BrM samples profiled. DE genes were defined as those with fold change > 2 or < -2, with an average baseMean count of 10, and FDR q < 0.05.

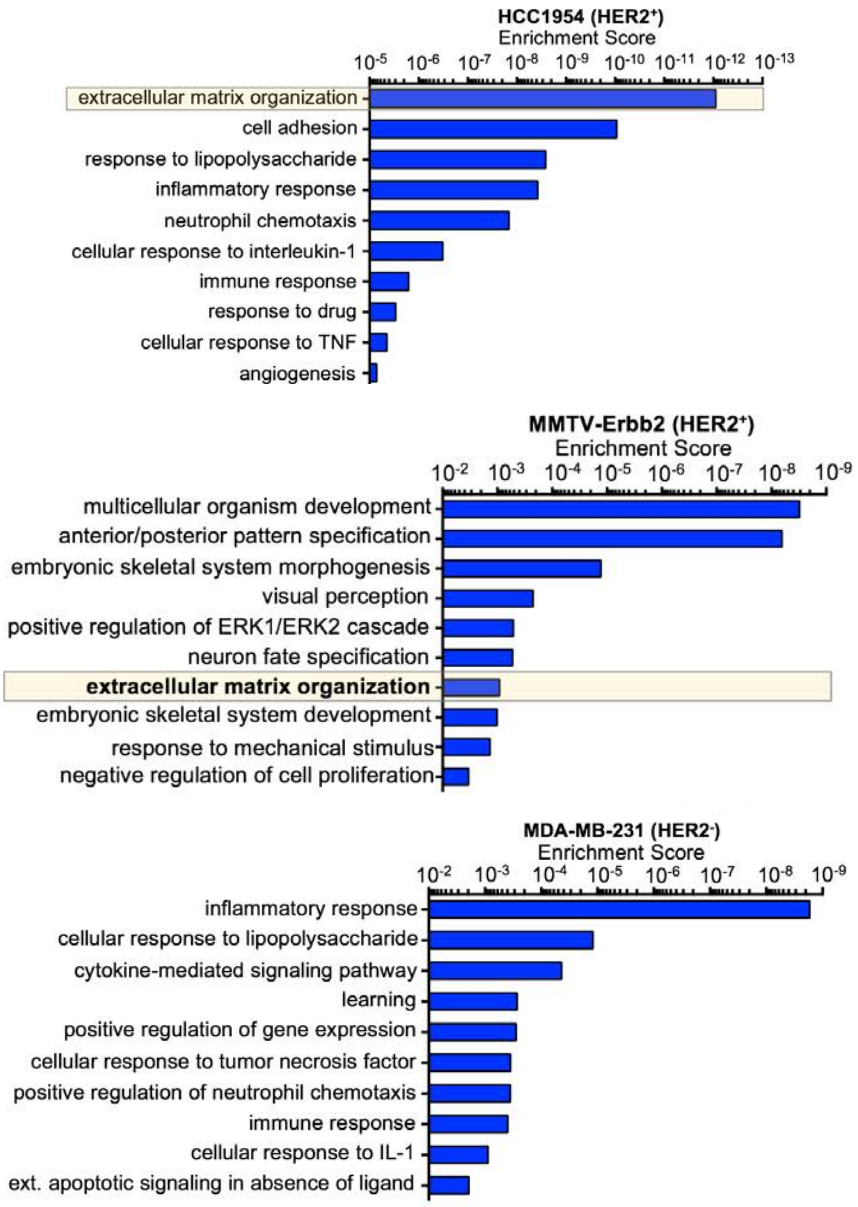

Figure 4-11. DAVID Gene Ontology Analyses of HCC1954, MMTV-Erbb2 and MDA-MB-231 derivatives comparing parental to BrM cell lines. Top-scoring gene sets are presented in an unbiased fashion.

Gene	MMTV-Erbb2 FC	HCC1954 FC
SEMA7A	27.91	3.44
KCNK2	24.33	2.97
BDKRB2	24.09	2.07
LAMC2	7.24	5.97
SPNS3	13.70	2.50
APCDD1	15.35	2.13
RASGRP1	3.50	6.48
EXOC3L4	6.35	3.30
NOS3	6.39	3.01
S100A7A	4.54	4.00
H2AFY2	3.94	4.47
IL24	8.05	2.09
TNC	6.87	4.45
B4GALNT3	4.81	2.80
CRIP2	5.66	2.32
PADI2	5.02	2.39
IRF8	5.57	2.14
DUSP5	3.58	3.13
GNAZ	3.20	2.99
PTPRE	2.99	3.11
IRS2	2.10	4.24
GYLTL1B	4.28	2.05
KLHL38	3.33	2.61
COL4A1	4.00	2.04
PIP5K1B	3.88	2.03
PDZD4	2.70	2.85
ERRFI1	2.34	2.61
CST6	2.79	2.11
SDPR	2.71	2.01
EEPD1	2.45	2.16
CSGALNACT1	2.38	2.18
HS3ST1	2.34	2.15

Gene	MMTV-Erbb2 FC	HCC1954 FC
CDC42EP5	-2.14	-2.11
TUSC1	-2.31	-2.02
SERINC5	-2.24	-2.09
UCP2	-2.23	-2.15
ENTPD2	-2.50	-2.03
PAK6	-2.51	-2.08
VWA5A	-2.26	-2.37
CSRP2	-2.63	-2.10
FKBP11	-2.07	-2.79
LPHN2	-3.02	-2.13
BTG2	-2.45	-2.70
NCAM1	-3.36	-2.08
ZSWIM6	-3.32	-2.20
HLX	-3.84	-2.07
MMP14	-2.76	-2.92
GSDMD	-3.75	-2.26
HCAR2	-4.26	-2.01
EGLN3	-3.86	-2.28
ZBTB7C	-4.53	-2.00
ABCA1	-3.95	-2.52
VSIG10L	-4.36	-2.46
SSBP2	-5.74	-2.21
SPP1	-2.35	-5.47
TGFB1	-3.08	-4.23
SEMA3A	-6.95	-2.05
EDAR	-4.85	-2.97
SEPP1	-4.94	-3.44
KRT14	-2.14	-8.32
LRRC75B	-3.90	-5.24
SEMA3D	-9.86	-2.09
CREB3L1	-6.17	-3.34
MEF2C	-6.74	-3.28
MUC15	-9.85	-2.33
PPP1R1B	-11.33	-2.11
IFITM10	-9.59	-2.60
IL1RN	-12.63	-2.15
ANGPTL4	-5.88	-4.68
WNT5A	-15.69	-2.13
HPSE	-14.03	-2.41
CCL5	-9.66	-4.72
PDGFD	-4.50	-14.93
PTGER2	-27.68	-2.64
OPLAH	-9.29	-8.92
MALL	-34.63	-3.16
BDH1	-62.87	-2.24
MYCL	-43.85	-3.51
NOV	-67.66	-2.36

Figure 4-12. Concordantly differentially expressed (DE) genes in HCC1954 and MMTV-Erbb2 HER2+ datasets, comparing parental to brain-tropic metastatic (BrM) derivatives.

Gene	Hazards Ratio	p-value
COL4A1	2.11	0.00034
IL24	1.74	0.035
TNC	1.6	0.038
SEMA7A	1.4	0.06
GSDMD	0.62	0.025
SEPP1	0.57	0.01
FKBP11	0.57	0.008
PAK6	0.57	0.032
ZSWIM6	0.55	0.013
MYCL	0.54	0.0058
EDAR	0.52	0.0087
VSIG10L	0.52	0.0082
CCL5	0.51	0.0013
PPP1R1B	0.51	0.0042
PTGER2	0.5	0.0038
IL1RN	0.49	0.0012
BTG2	0.4	0.000019
NOV	0.34	0.000083
HPSE	0.33	0.000028

Figure 4-13. Summary of differentially expressed genes in HER2+ datasets that were predictive of relapse free survival (RFS) in the HER2+ subtype setting as computed by *kmplot*. We excluded those that did not have a p-value < 0.05

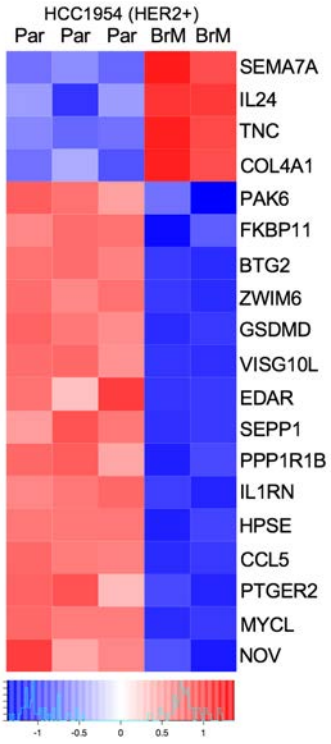

Figure 4-14. Heatmap of differentially expressed genes in HCC1954 (HER2+) which were also predictive of relapse free survival in HER2+ breast cancer patients by *kmplot*. 4 upregulated genes and 15 downregulated genes.

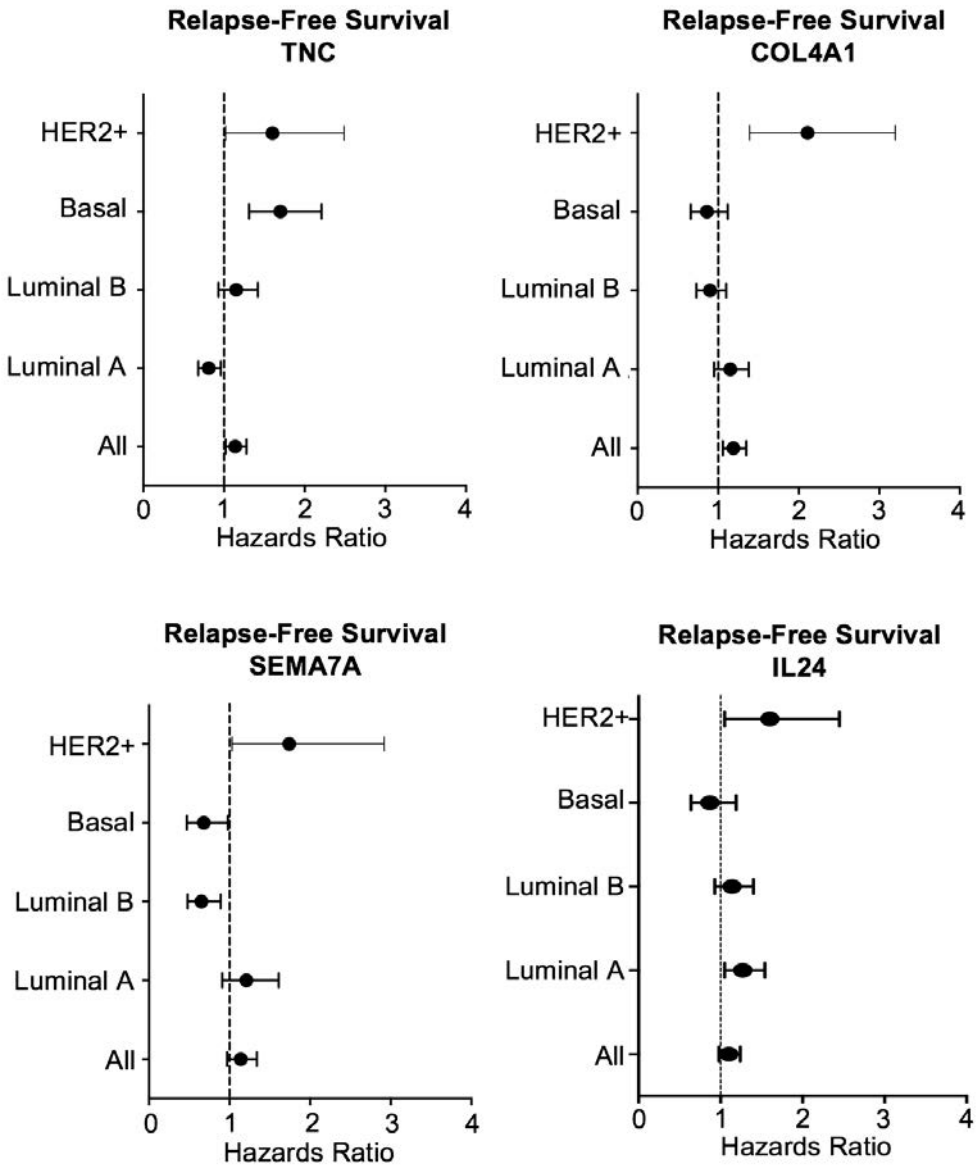

Figure 4-15. Hazards Ratio forest plots of the predictive ability of TNC, COL4A1, SEMA7A and IL24 in relapse free survival outcomes. In all cases, these genes were most predictive in the context of HER2+ disease, versus other breast cancer subtypes.

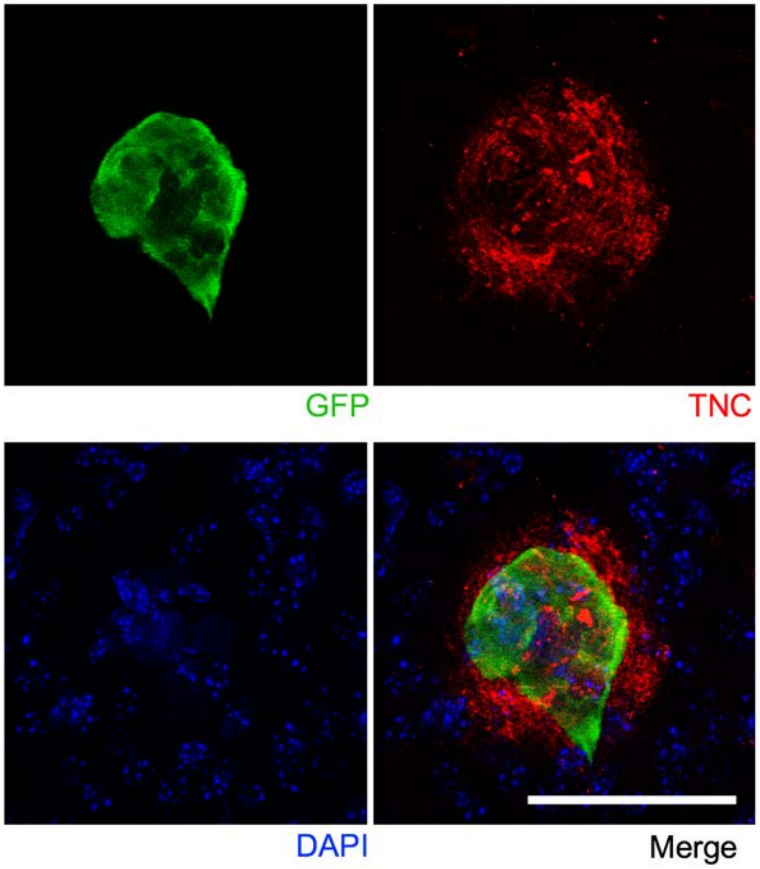

Figure 4-16. Immunofluorescence micrographs of representative incipient HER2+ spheroidal cell cluster in the brain of an athymic nude mouse 14 days post-inoculation. TNC deposition is visible in the periphery of the spheroidal cell cluster. Scale bar = 50 um

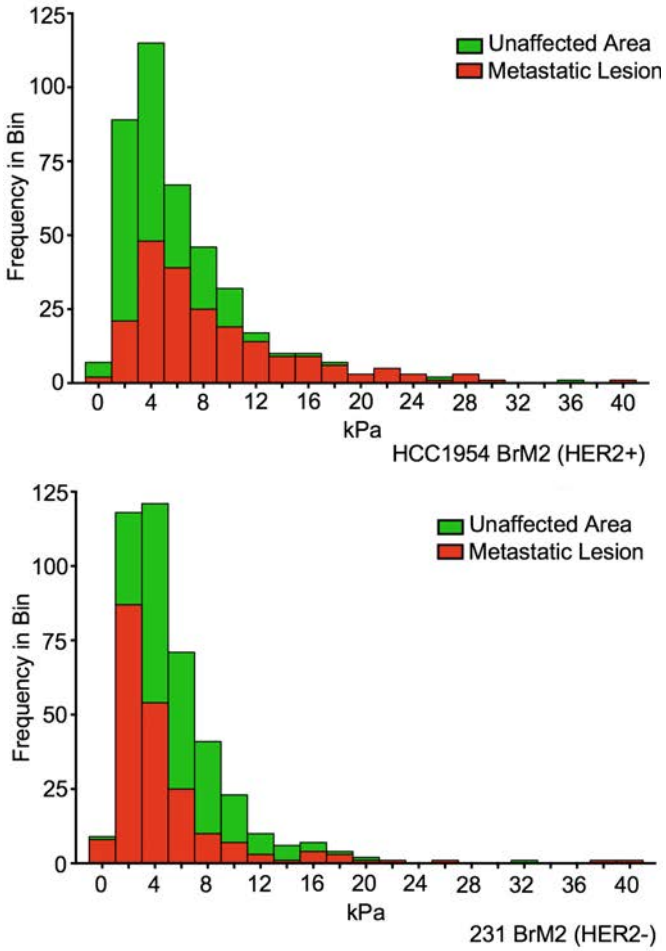

Figure 4-17. Atomic force microscopy analyses of the underlying brain parenchyma stiffness *in situ* surrounding HCC1954 BrM (HER2+) or 231 BrM (HER2-) metastatic lesions. Stiffness measurements were compared to an adjacent unaffected region 600 um away. n = 210 individual measurements per condition, with each bar representing a bin region of 2 kPa.

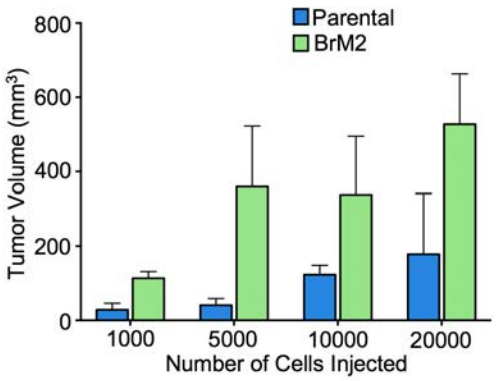

	Parental	BrM2
1,000	2/5	5/5
5,000	3/5	4/5
10,000	5/5	4/5
20,000	2/5	5/5
CSC	**1/9589**	**1/2600**

Figure 4-18. *In vivo* limiting dilution analyses of HCC1954 Parental vs BrM derivatives orthotopically injected into the mammary fat pad of athymic nude mice. Caliper measurements were 90 days post-injection.

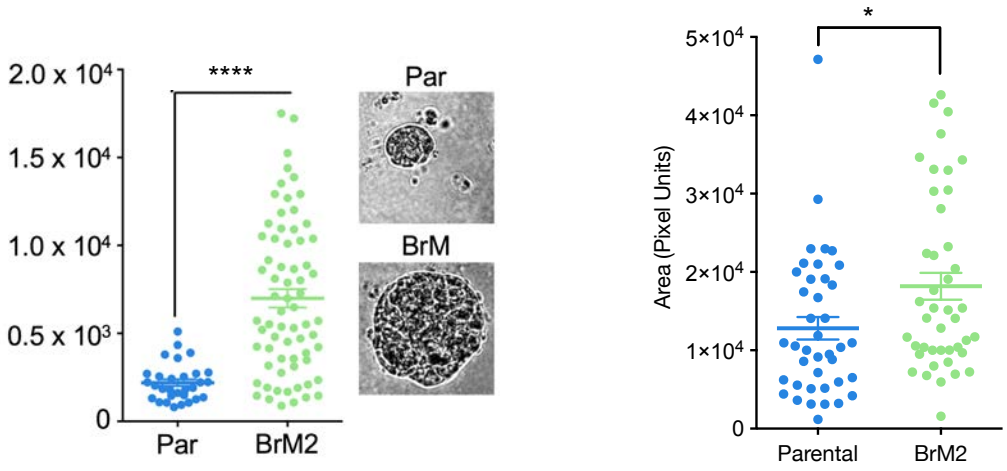

Figure 4-19. Left panel: 3D matrigel growth formation assay of HCC1954 Parental vs BrM derivatives. Cells were allowed to grow undisturbed for 9 days. n = 30 – 70 individual colonies per condition. **** $p < 0.001$
Right panel: Oncosphere growth formation assay of HCC1954 Parental vs BrM derivatives. Cells were allowed to grow undisturbed for 9 days. n = 40 - 45 individual colonies per condition. * $p < 0.019$

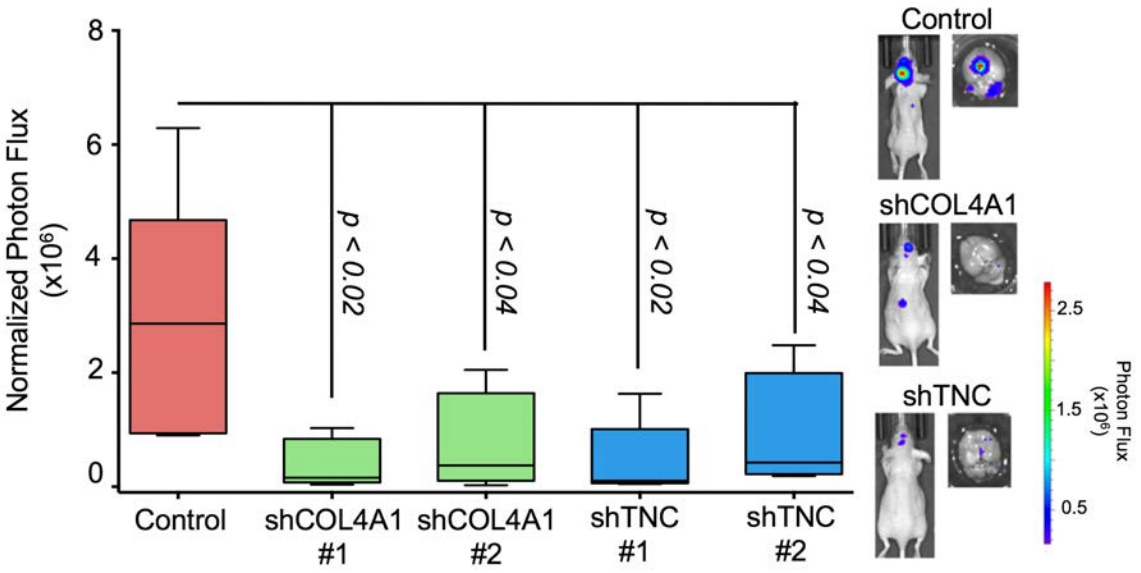

Figure 4-20. Knockdown of TNC or COL4A1 in HCC1954 BrM2 (HER2+) cells by shRNA. Cells were injected via intracardiac inoculation into athymic nude mice. Data are whole body photon flux at 1 month post injection, with whisker plots representing minimum and maximum values. n = 5 mice per group

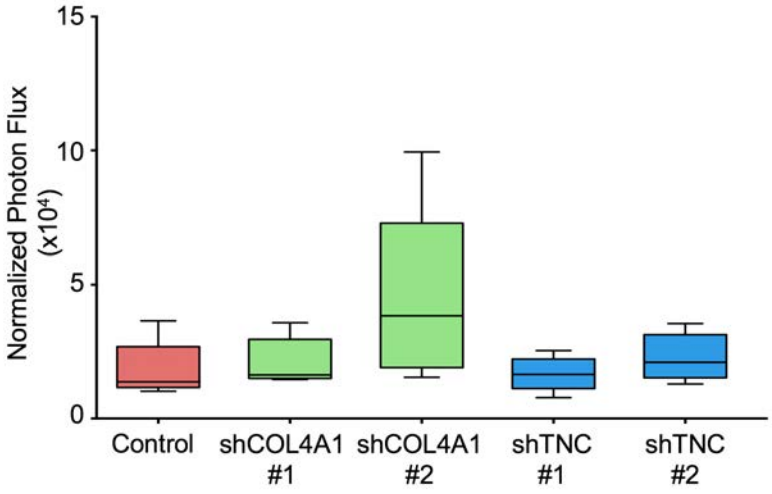

Figure 4-21. TNC or COL4A1 HCC1954 BrM knockdown cells in lung metastasis assays by tail-vein injection. Data are lung photon flux after 4 weeks post inoculation into athymic nude mice. Whisker plots represent minimum and maximum values.
n = 5 mice per group

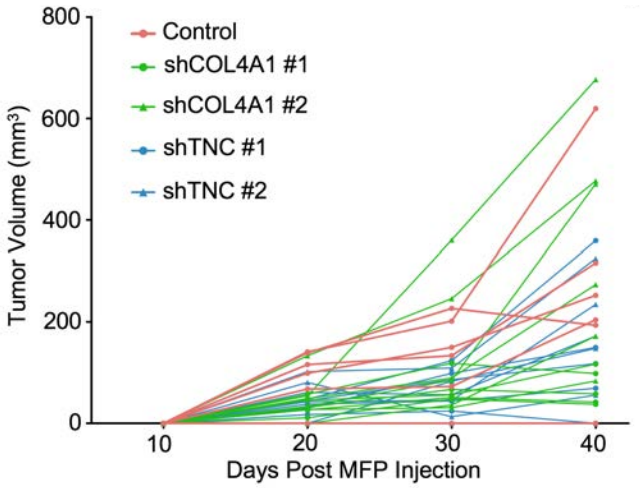

Figure 4-22. Orthotopic implantation of TNC and COL4A1 HCC1954 BrM knockdown cells into the mammary fat pad of athymic nude mice, and tracked by digital caliper measurement over the course of 40 days. No significant change in tumor growth was seen between control and TNC or COL4A1 knockdown tumors. n = 6 tumors per group.

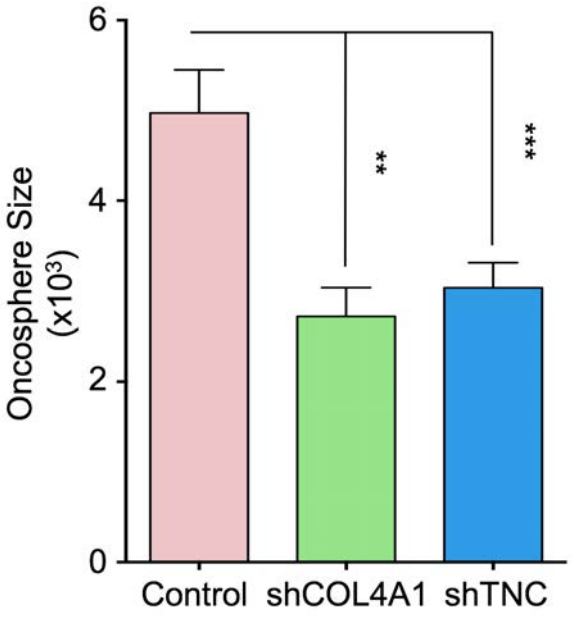

Figure 4-23. Oncosphere growth formation assay of HCC1954 BrM control cells, or those depleted of COL4A1 or TNC by shRNA. n = 100 colonies individually measured per group after 7 days of growth *in vitro*. ** $p < 0.01$, *** $p < 0.001$

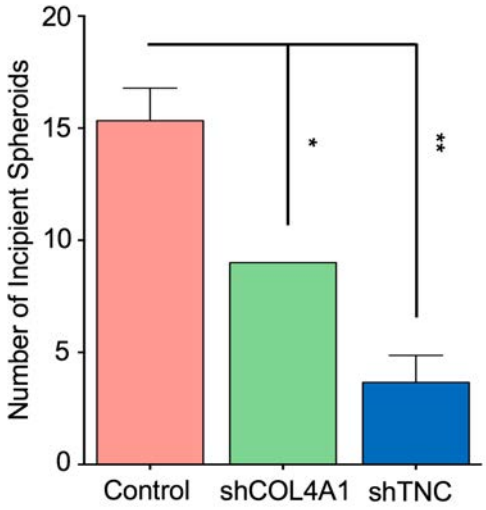

Figure 4-24. Quantification of incipient HER2+ spheroidal clusters 14 days post intracardiac injection into athymic nude mice. N = 3 mice, scoring representative serial sections of the brain for each mouse. * $p < 0.05$, ** $p < 0.01$

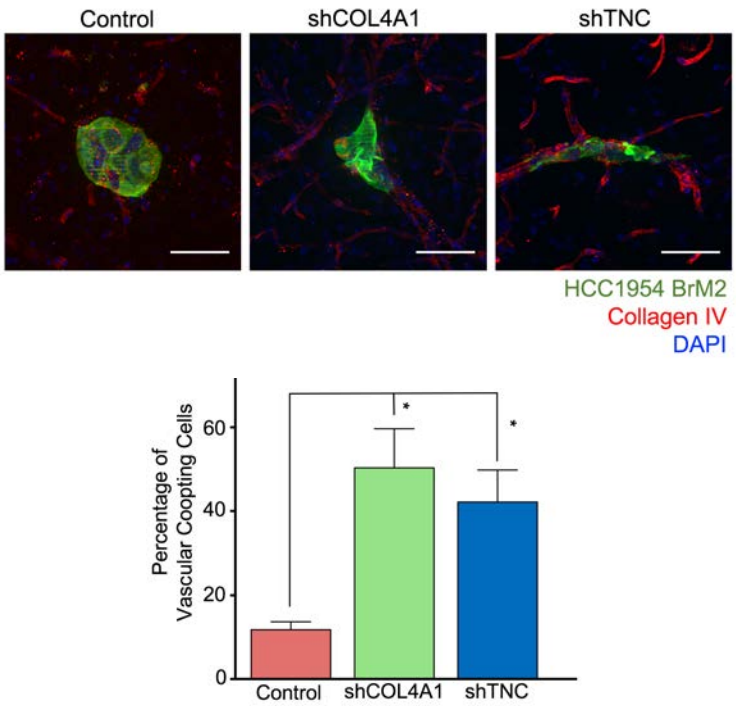

Figure 4-25. Top panel: Representative immunofluorescence micrographs of HCC1954 BrM2 control cells or those depleted of COL4A1 or TNC by shRNA after one week post intracardiac injection.
Bottom panel: Quantification of the percentage of vascular coopting cells in the brains of athymic nude mice injected with the indicated cell lines. N = 3 mice per group, scoring representative serial sections of the brain for each mouse. * $p < 0.05$, Student's t-test

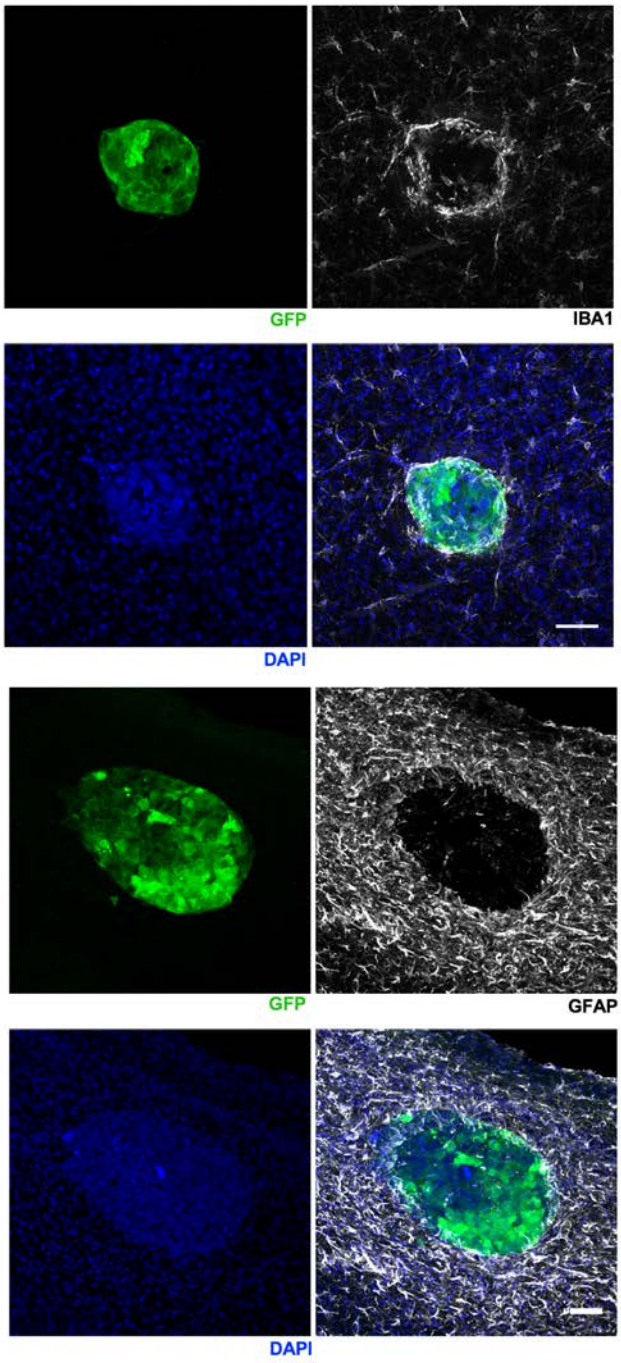

Figure 4-26. Exclusion of microglia (IBA1, top panel) or astrocytes (GFAP, bottom panel) from growing spheroidal clusters of HCC1954 BrM cells in the brain parenchyma of athymic nude mice. Both microglia and astrocytes are predominantly excluded from the growing metastatic lesion, and are restricted to the periphery of the cancer cells. Scale bar = 50 um

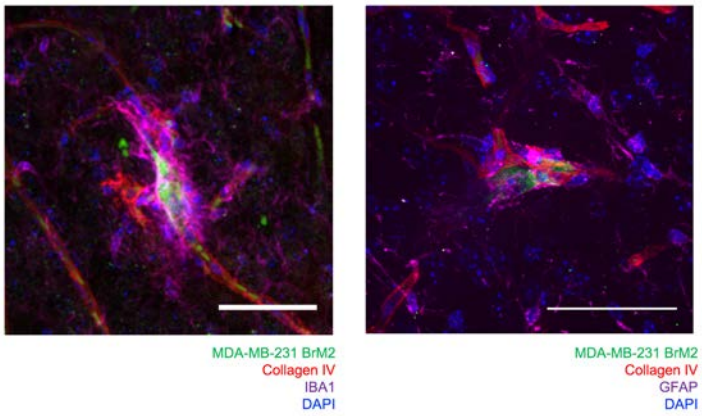

Figure 4-27. Intercalation of microglia (IBA1, Left panel) or astrocytes (GFAP, Right panel) with HER2- (MDA-MB-231 BrM2) vascular coopting cells in the parenchyma of an athymic nude mouse. Scale bars = 50 um

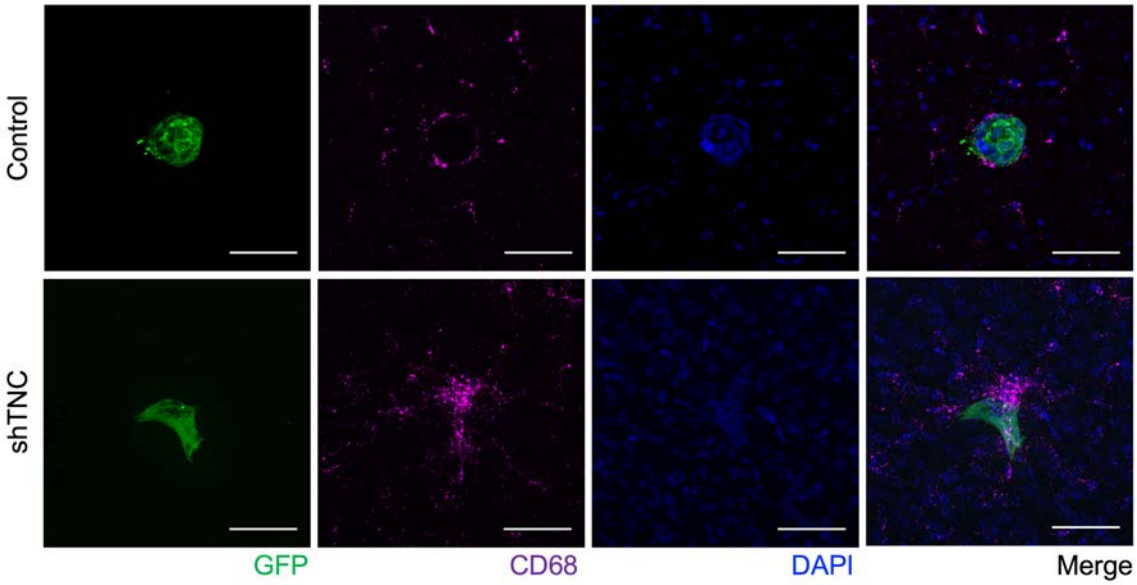

Figure 4-28. HCC1954 BrM2 cells that have attenuated TNC levels by shRNA show a marked increase in recognition and infiltration by CD68+ activated microglia Immunofluorescence micrographs are from sections of brains harvested 7 days post injection of indicated cell lines. Scale bars = 50 um

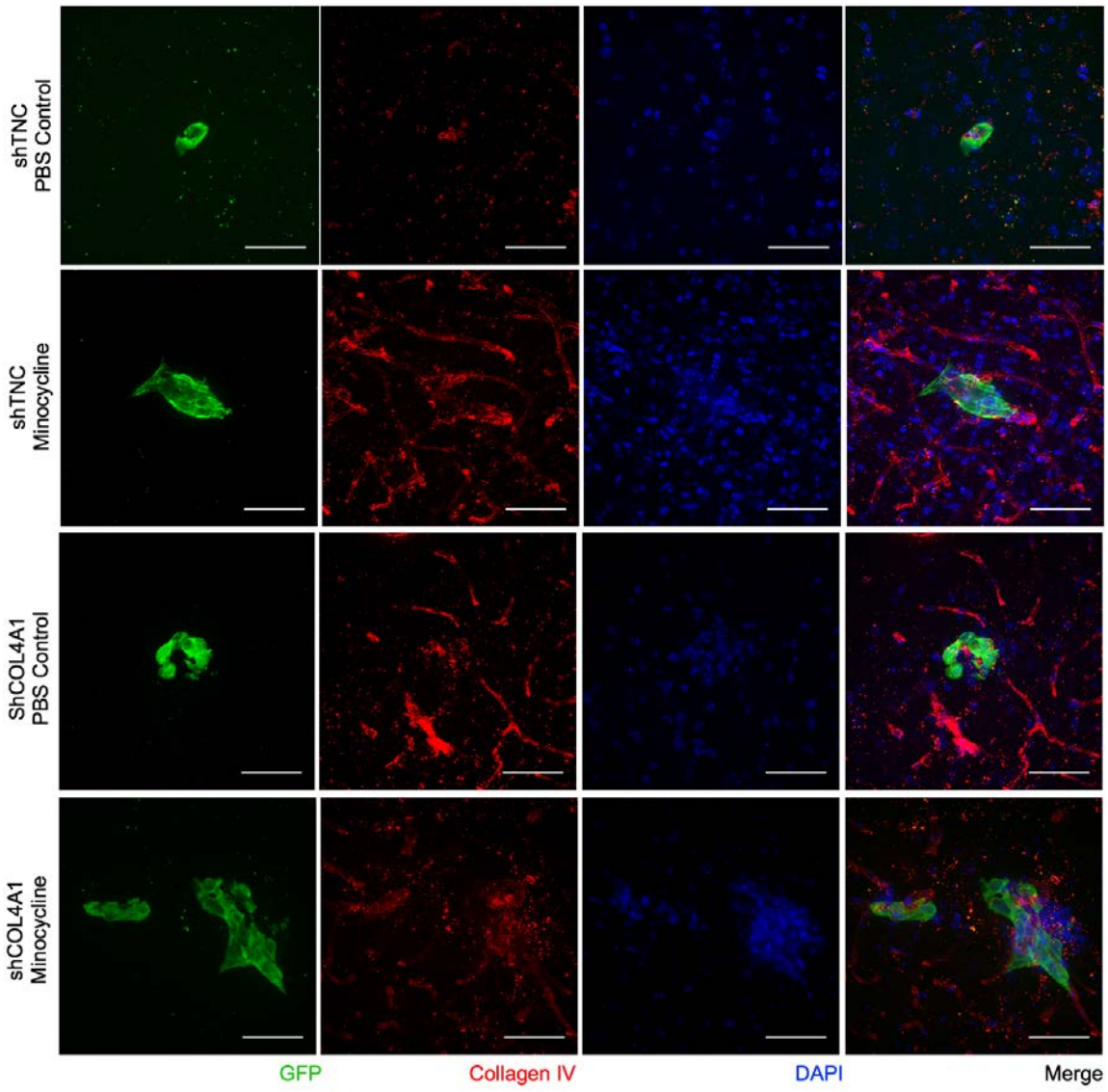

Figure 4-29. HCC1954 BrM cells depleted of either COL4A1 or TNC by shRNA were injected into mice treated with PBS control or minocycline treatment (50mg/kg i.p.) daily for 14 days. Immunofluorescence of cells *in situ* in the brain.
Vascular coopting sheaths were detected in minocycline-treated animals.

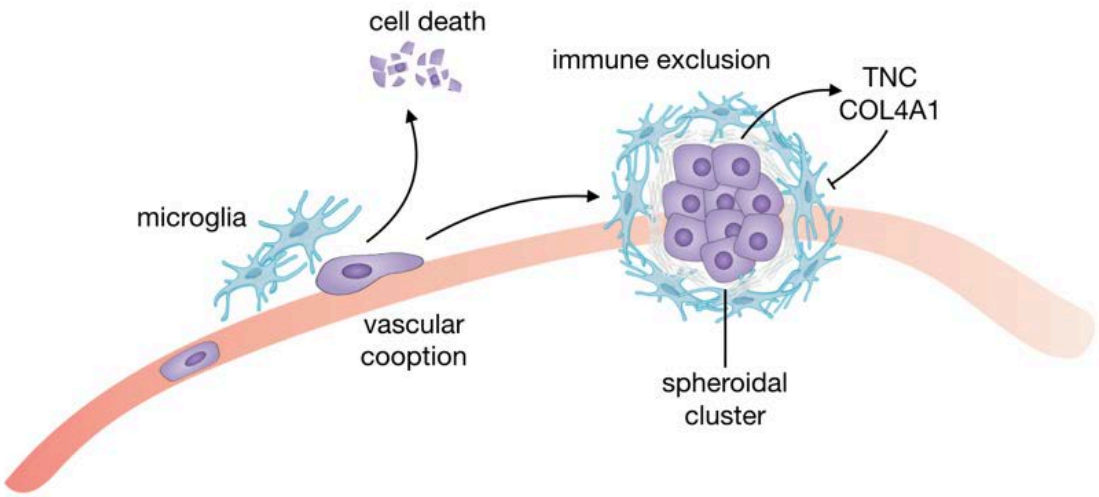

Figure 4-30. A model summarizing HER2+ mediated breast cancer brain metastases. As HER2 BrM+ cells extravasate into the circulation, initial vascular cooption is rapidly supplanted by spheroidal growth, generating cell clusters *in vivo*. Spheroidal clusters are generally anchored to the vasculature, but contain cells that are agnostic to direct contact with the vasculature. This protective configuration preferentially excludes reactive stroma from engaging with growing metastatic lesions, facilitating their outgrowth. Extracellular matrix deposition of TNC and COL4A1 promotes spheroidal growth, and attenuation of tumor-cell deposition of these factors results in prolonged vascular cooption. In the context of HER2+ cancer cells, prolonged vascular cooption is recognized by activated microglia, and leads to the death of cancer cells. Inhibition of microglial activation by minocycline permits the growth of vascular-coopting HER2+ cancer cells.

Aceto, N., Bardia, A., Miyamoto, D.T., Donaldson, M.C., Ben S Wittner, Spencer, J.A., Yu, M., Pely, A., Engstrom, A., Zhu, H., et al. (2014). Circulating Tumor Cell Clusters Are Oligoclonal Precursors of Breast Cancer Metastasis. Cell *158*, 1110–1122.

Al-Hajj, M., and Wicha, M.S. (2003). Prospective identification of tumorigenic breast cancer cells.

Alimandi, M., Romano, A., Curia, M.C., Muraro, R., Fedi, P., Aaronson, S.A., Di Fiore, P.P., and Kraus, M.H. (1995). Cooperative signaling of ErbB3 and ErbB2 in neoplastic transformation and human mammary carcinomas. Oncogene *10*, 1813–1821.

Anders, S., Pyl, P.T., and Huber, W. (2015). HTSeq--a Python framework to work with high-throughput sequencing data. Bioinformatics *31*, 166–169.

Arnold, K., Sarkar, A., Yram, M.A., Polo, J.M., Bronson, R., Sengupta, S., Seandel, M., Geijsen, N., and Hochedlinger, K. (2011). Sox2(+) adult stem and progenitor cells are important for tissue regeneration and survival of mice. Cell Stem Cell *9*, 317–329.

Aslakson, C.J., and Miller, F.R. (1992). Selective events in the metastatic process defined by analysis of the sequential dissemination of subpopulations of a mouse mammary tumor. Cancer Research *52*, 1399–1405.

Austin, C.D., De Mazière, A.M., Pisacane, P.I., van Dijk, S.M., Eigenbrot, C., Sliwkowski, M.X., Klumperman, J., and Scheller, R.H. (2004). Endocytosis and sorting of ErbB2 and the site of action of cancer therapeutics trastuzumab and geldanamycin. Mol. Biol. Cell *15*, 5268–5282.

Azim, H.A., and Azim, H.A., Jr (2012). Systemic treatment of brain metastases in HER2-positive breast cancer: current status and future directions. Future Oncology *8*, 135–144.

Bang, Y.-J., Van Cutsem, E., Feyereislova, A., Chung, H.C., Shen, L., Sawaki, A., Lordick, F., Ohtsu, A., Omuro, Y., Satoh, T., et al. (2010). Trastuzumab in combination with chemotherapy versus chemotherapy alone for treatment of HER2-positive advanced gastric or gastro-oesophageal junction cancer (ToGA): a phase 3, open-label, randomised controlled trial. Lancet *376*, 687–697.

Barok, M., Isola, J., Pályi-Krekk, Z., Nagy, P., Juhász, I., Kauraniemi, P., Kapanen, A., Tanner, M., Vereb, G., and Szöllösi, J. (2007). Trastuzumab causes antibody-dependent cellular cytotoxicity-mediated growth inhibition of submacroscopic JIMT-1 breast cancer xenografts despite intrinsic drug resistance. Molecular Cancer Therapeutics *6*, 2065–2072.

Baselga, J., Norton, L., Albanell, J., Kim, Y.M., and Mendelsohn, J. (1998). Recombinant humanized anti-HER2 antibody (Herceptin) enhances the antitumor

activity of paclitaxel and doxorubicin against HER2/neu overexpressing human breast cancer xenografts. Cancer Research *58*, 2825–2831.

Baselga, J., and Swain, S.M. (2009). Novel anticancer targets: revisiting ERBB2 and discovering ERBB3. Nature Publishing Group *9*, 463–475.

Bild, A.H., Yao, G., Chang, J.T., Wang, Q., Potti, A., Chasse, D., Joshi, M.-B., Harpole, D., Lancaster, J.M., Berchuck, A., et al. (2005). Oncogenic pathway signatures in human cancers as a guide to targeted therapies. Nature *439*, 353–357.

Boire, A., Zou, Y., Shieh, J., Macalinao, D.G., Pentsova, E., and Massagué, J. (2017). Complement Component 3 Adapts the Cerebrospinal Fluid for Leptomeningeal Metastasis. Cell *168*, 1101–1113.e1113.

Bos, P.D., Zhang, X.H.F., Nadal, C., Shu, W., Gomis, R.R., Nguyen, D.X., Minn, A.J., van de Vijver, M.J., Gerald, W.L., Foekens, J.A., et al. (2009). Genes that mediate breast cancer metastasis to the brain. Nature *459*, 1005–1009.

Bradley, M., Zeytun, A., Rafi-Janajreh, A., Nagarkatti, P.S., and Nagarkatti, M. (1998). Role of spontaneous and interleukin-2-induced natural killer cell activity in the cytotoxicity and rejection of Fas+ and Fas- tumor cells. Blood *92*, 4248–4255.

Bragado, P., Estrada, Y., Parikh, F., Krause, S., Capobianco, C., Farina, H.G., Schewe, D.M., and Aguirre-Ghiso, J.A. (2013). TGF-β2 dictates disseminated tumour cell fate in target organs through TGF-β-RIII and p38α/β signalling. Nat Cell Biol *15*, 1351–1361.

Braun, S., Vogl, F.D., Naume, B., Janni, W., Osborne, M.P., Coombes, R.C., Schlimok, G., Diel, I.J., Gerber, B., Gebauer, G., et al. (2005). A pooled analysis of bone marrow micrometastasis in breast cancer. N. Engl. J. Med. *353*, 793–802.

Brufsky, A.M., Mayer, M., Rugo, H.S., Kaufman, P.A., Tan-Chiu, E., Tripathy, D., Tudor, I.C., Wang, L.I., Brammer, M.G., Shing, M., et al. (2011a). Central Nervous System Metastases in Patients with HER2-Positive Metastatic Breast Cancer: Incidence, Treatment, and Survival in Patients from registHER. Clinical Cancer Research *17*, 4834–4843.

Brufsky, A.M., Mayer, M., Rugo, H.S., Kaufman, P.A., Tan-Chiu, E., Tripathy, D., Tudor, I.C., Wang, L.I., Brammer, M.G., Shing, M., et al. (2011b). Central nervous system metastases in patients with HER2-positive metastatic breast cancer: incidence, treatment, and survival in patients from registHER. Clin. Cancer Res. *17*, 4834–4843.

Capelan, M., Pugliano, L., De Azambuja, E., Bozovic, I., Saini, K.S., Sotiriou, C., Loi, S., and Piccart-Gebhart, M.J. (2013). Pertuzumab: new hope for patients with HER2-positive breast cancer. Ann. Oncol. *24*, 273–282.

Carey, L.A., Perou, C.M., Livasy, C.A., Dressler, L.G., Cowan, D., Conway, K., Karaca, G., Troester, M.A., Tse, C.K., Edmiston, S., et al. (2006). Race, breast cancer subtypes, and survival in the Carolina Breast Cancer Study. Jama *295*, 2492–2502.

Chen, E.J., Novakofski, J., Jenkins, W.K., and O'Brien, W.D. (1996). Young's modulus measurements of soft tissues with application to elasticity imaging. IEEE Transactions on Ultrasonics, Ferroelectrics and Frequency Control *43*, 191–194.

Chen, Q., Boire, A., Jin, X., Valiente, M., Er, E.E., Lopez-Soto, A., Jacob, L.S., Patwa, R., Shah, H., Xu, K., et al. (2016). Carcinoma–astrocyte gap junctions promote brain metastasis by cGAMP transfer. Nature *533*, 493–498.

Clark, S.E., Warwick, J., Carpenter, R., Bowen, R.L., Duffy, S.W., and Jones, J.L. (2011). Molecular subtyping of DCIS: heterogeneity of breast cancer reflected in pre-invasive disease. British Journal of Cancer *104*, 120–127.

Cleator, S., Heller, W., and Coombes, R.C. (2007). Triple-negative breast cancer: therapeutic options. Lancet Oncol. *8*, 235–244.

Cristofanilli, M., Budd, G.T., Ellis, M.J., Stopeck, A., Matera, J., Miller, M.C., Reuben, J.M., Doyle, G.V., Allard, W.J., Terstappen, L.W.M.M., et al. (2004). Circulating tumor cells, disease progression, and survival in metastatic breast cancer. N. Engl. J. Med. *351*, 781–791.

Crone, S.A., Zhao, Y.-Y., Fan, L., Gu, Y., Minamisawa, S., Liu, Y., Peterson, K.L., Chen, J., Kahn, R., Condorelli, G., et al. (2002). ErbB2 is essential in the prevention of dilated cardiomyopathy. Nature Medicine *8*, 459–465.

Demicheli, R., Miceli, R., Moliterni, A., Zambetti, M., Hrushesky, W.J.M., Retsky, M.W., Valagussa, P., and Bonadonna, G. (2005). Breast cancer recurrence dynamics following adjuvant CMF is consistent with tumor dormancy and mastectomy-driven acceleration of the metastatic process. Annals of Oncology *16*, 1449–1457.

Dontu, G., Abdallah, W.M., Foley, J.M., Jackson, K.W., Clarke, M.F., Kawamura, M.J., and Wicha, M.S. (2003). In vitro propagation and transcriptional profiling of human mammary stem/progenitor cells. Genes & Development *17*, 1253–1270.

Duchnowska, R., Dziadziuszko, R., Czartoryska-Arłukowicz, B., Radecka, B., Szostakiewicz, B., Sosińska-Mielcarek, K., Karpińska, A., Starosławska, E., Kubiatowski, T., and Szczylik, C. (2009). Risk factors for brain relapse in HER2-positive metastatic breast cancer patients. Breast Cancer Res. Treat. *117*, 297–303.

Dunn, G.P., Old, L.J., and Schreiber, R.D. (2004). The immunobiology of cancer immunosurveillance and immunoediting. Immunity *21*, 137–148.

Eyles, J., Puaux, A.-L., Wang, X., Toh, B., Prakash, C., Hong, M., Tan, T.G., Zheng, L., Ong, L.C., Jin, Y., et al. (2010). Tumor cells disseminate early, but immunosurveillance limits metastatic outgrowth, in a mouse model of melanoma. J. Clin. Invest. *120*, 2030–2039.

Fan, R., Xu, F., Previti, M.L., Davis, J., Grande, A.M., Robinson, J.K., and Van Nostrand, W.E. (2007). Minocycline reduces microglial activation and improves behavioral deficits in a transgenic model of cerebral microvascular amyloid. J. Neurosci. *27*, 3057–3063.

Fellmann, C., Hoffmann, T., Sridhar, V., Hopfgartner, B., Muhar, M., Roth, M., Lai, D.Y., Barbosa, I.A.M., Kwon, J.S., Guan, Y., et al. (2013). An optimized microRNA backbone for effective single-copy RNAi. Cell Rep *5*, 1704–1713.

Fidler, I.J. (1970). Metastasis: quantitative analysis of distribution and fate of tumor emboli labeled with 125I-5-iodo-2′-deoxyuridine. J. Natl. Cancer Inst. *45*, 773–782.

Finak, G., Bertos, N., Pepin, F., Sadekova, S., Souleimanova, M., Zhao, H., Chen, H., Omeroglu, G., Meterissian, S., Omeroglu, A., et al. (2008). Stromal gene expression predicts clinical outcome in breast cancer. Nature Medicine *14*, 518–527.

Fisher, B., Dignam, J., Bryant, J., DeCillis, A., Wickerham, D.L., Wolmark, N., Costantino, J., Redmond, C., Fisher, E.R., Bowman, D.M., et al. (1996). Five versus more than five years of tamoxifen therapy for breast cancer patients with negative lymph nodes and estrogen receptor-positive tumors. J. Natl. Cancer Inst. *88*, 1529–1542.

Fu, R., Shen, Q., Xu, P., Luo, J.J., and Tang, Y. (2014). Phagocytosis of microglia in the central nervous system diseases. Mol. Neurobiol. *49*, 1422–1434.

Gao, H., Chakraborty, G., Lee-Lim, A.P., Mo, Q., Decker, M., Vonica, A., Shen, R., Brogi, E., Brivanlou, A.H., and Giancotti, F.G. (2012). The BMP inhibitor Coco reactivates breast cancer cells at lung metastatic sites. Cell *150*, 764–779.

Garratt, A.N., Voiculescu, O., Topilko, P., Charnay, P., and Birchmeier, C. (2000). A dual role of erbB2 in myelination and in expansion of the schwann cell precursor pool. The Journal of Cell Biology *148*, 1035–1046.

Garrett, T.P.J., McKern, N.M., Lou, M., Elleman, T.C., Adams, T.E., Lovrecz, G.O., Kofler, M., Jorissen, R.N., Nice, E.C., Burgess, A.W., et al. (2003). The crystal structure of a truncated ErbB2 ectodomain reveals an active conformation, poised to interact with other ErbB receptors. Mol. Cell *11*, 495–505.

Gatza, M.L., Lucas, J.E., Barry, W.T., Kim, J.W., Wang, Q., Crawford, M.D.,

Datto, M.B., Kelley, M., Mathey-Prevot, B., Potti, A., et al. (2010). A pathway-based classification of human breast cancer. Proc. Natl. Acad. Sci. U.S.A. *107*, 6994–6999.

Gazdar, A.F., and Minna, J.D. (1996). NCI series of cell lines: an historical perspective. J. Cell. Biochem. Suppl. *24*, 1–11.

Gazdar, A.F., Kurvari, V., Virmani, A., Gollahon, L., Sakaguchi, M., Westerfield, M., Kodagoda, D., Stasny, V., Cunningham, H.T., and Wistuba, I.I. (1998). Characterization of paired tumor and non-tumor cell lines established from patients with breast cancer. Int. J. Cancer *78*, 766–774.

Geyer, C.E., Forster, J., Lindquist, D., Chan, S., Romieu, C.G., Pienkowski, T., Jagiello-Gruszfeld, A., Crown, J., Chan, A., Kaufman, B., et al. (2006). Lapatinib plus capecitabine for HER2-positive advanced breast cancer. N. Engl. J. Med. *355*, 2733–2743.

Ghajar, C.M., Peinado, H., Mori, H., Matei, I.R., Evason, K.J., Brazier, H., Almeida, D., Koller, A., Hajjar, K.A., Stainier, D.Y.R., et al. (2013). The perivascular niche regulates breast tumour dormancy. Nat Cell Biol *15*, 807–817.

Goss, P.E., and Chambers, A.F. (2010). Does tumour dormancy offer a therapeutic target? Nature Publishing Group *10*, 871–877.

Goss, P.E., Ingle, J.N., Martino, S., Robert, N.J., Muss, H.B., Piccart, M.J., Castiglione, M., Tu, D., Shepherd, L.E., Pritchard, K.I., et al. (2003). A randomized trial of letrozole in postmenopausal women after five years of tamoxifen therapy for early-stage breast cancer. N. Engl. J. Med. *349*, 1793–1802.

Goss, P.E., Ingle, J.N., Pritchard, K.I., Robert, N.J., Muss, H., Gralow, J., Gelmon, K., Whelan, T., Strasser-Weippl, K., Rubin, S., et al. (2016). Extending Aromatase-Inhibitor Adjuvant Therapy to 10 Years. N. Engl. J. Med. *375*, 209–219.

Gravalos, C., and Jimeno, A. (2008). HER2 in gastric cancer: a new prognostic factor and a novel therapeutic target. Ann. Oncol. *19*, 1523–1529.

Guo, W., Keckesova, Z., Donaher, J.L., Shibue, T., Tischler, V., Reinhardt, F., Itzkovitz, S., Noske, A., Zürrer-Härdi, U., Bell, G., et al. (2012). Slug and Sox9 Cooperatively Determine the Mammary Stem Cell State. Cell *148*, 1015–1028.

Gupta, G.P., and Massagué, J. (2006). Cancer Metastasis: Building a Framework. Cell *127*, 679–695.

Hänzelmann, S., Castelo, R., and Guinney, J. (2013). GSVA: gene set variation analysis for microarray and RNA-seq data. BMC Bioinformatics *14*, 7.

Hecht, J.R., Bang, Y.J., Qin, S.K., and Chung, H.C. (2015). Lapatinib in combination with capecitabine plus oxaliplatin (CapeOx) in HER2-positive advanced or metastatic gastric, esophageal, or gastroesophageal adenocarcinoma (AC): The TRIO-013/LOGiC Trial. Journal of Clinical Oncology 31, 18.

Huang, D.W., Sherman, B.T., and Lempicki, R.A. (2009a). Bioinformatics enrichment tools: paths toward the comprehensive functional analysis of large gene lists. Nucleic Acids Res. *37*, 1–13.

Huang, D.W., Sherman, B.T., and Lempicki, R.A. (2009b). Systematic and integrative analysis of large gene lists using DAVID bioinformatics resources. Nature Protocols *4*, 44–57.

Hudis, C.A. (2007). Trastuzumab--mechanism of action and use in clinical practice. N. Engl. J. Med. *357*, 39–51.

Hudziak, R.M., Lewis, G.D., Winget, M., Fendly, B.M., Shepard, H.M., and Ullrich, A. (1989). p185HER2 monoclonal antibody has antiproliferative effects in vitro and sensitizes human breast tumor cells to tumor necrosis factor. Mol. Cell. Biol. *9*, 1165–1172.

Hynes, N.E., and Lane, H.A. (2005). ERBB receptors and cancer: the complexity of targeted inhibitors. Nat Rev Cancer *5*, 341–354.

International Early Lung Cancer Action Program Investigators, Henschke, C.I., Yankelevitz, D.F., Libby, D.M., Pasmantier, M.W., Smith, J.P., and Miettinen, O.S. (2006). Survival of patients with stage I lung cancer detected on CT screening. N. Engl. J. Med. *355*, 1763–1771.

Inwald, E.C., Koller, M., Klinkhammer-Schalke, M., Zeman, F., Hofstädter, F., Gerstenhauer, M., Brockhoff, G., and Ortmann, O. (2015). 4-IHC classification of breast cancer subtypes in a large cohort of a clinical cancer registry: use in clinical routine for therapeutic decisions and its effect on survival. Breast Cancer Res. Treat. *153*, 647–658.

Jin, S., Deng, Y., Hao, J.-W., Li, Y., Liu, B., Yu, Y., Shi, F.-D., and Zhou, Q.-H. (2014). NK cell phenotypic modulation in lung cancer environment. PLoS ONE *9*, e109976.

Junttila, T.T., Akita, R.W., Parsons, K., Fields, C., Phillips, G.D.L., Friedman, L.S., Sampath, D., and Sliwkowski, M.X. (2009). Ligand-Independent HER2/HER3/PI3K Complex Is Disrupted by Trastuzumab and Is Effectively Inhibited by the PI3K Inhibitor GDC-0941. Cancer Cell *15*, 429–440.

Kobayashi, A., Okuda, H., Xing, F., Pandey, P.R., Watabe, M., Hirota, S., Pai, S.K., Liu, W., Fukuda, K., Chambers, C., et al. (2011). Bone morphogenetic protein 7 in dormancy and metastasis of prostate cancer stem-like cells in bone.

J. Exp. Med. *208*, 2641–2655.

Kobayashi, K., Imagama, S., Ohgomori, T., Hirano, K., Uchimura, K., Sakamoto, K., Hirakawa, A., Takeuchi, H., Suzumura, A., Ishiguro, N., et al. (2013). Minocycline selectively inhibits M1 polarization of microglia. Cell Death Dis *4*, e525.

Koebel, C.M., Vermi, W., Swann, J.B., Zerafa, N., Rodig, S.J., Old, L.J., Smyth, M.J., and Schreiber, R.D. (2007). Adaptive immunity maintains occult cancer in an equilibrium state. Nature *450*, 903–907.

Kozlowski, J.M., Fidler, I.J., Campbell, D., Xu, Z.L., Kaighn, M.E., and Hart, I.R. (1984). Metastatic behavior of human tumor cell lines grown in the nude mouse. Cancer Research *44*, 3522–3529.

Kute, T.E., Savage, L., Stehle, J.R., Kim-Shapiro, J.W., Blanks, M.J., Wood, J., and Vaughn, J.P. (2009). Breast tumor cells isolated from in vitro resistance to trastuzumab remain sensitive to trastuzumab anti-tumor effects in vivo and to ADCC killing. Cancer Immunol. Immunother. *58*, 1887–1896.

Langmead, B., and Salzberg, S.L. (2012). Fast gapped-read alignment with Bowtie 2. Nat Meth *9*, 357–359.

Lanier, L.L. (2015). NKG2D Receptor and Its Ligands in Host Defense. Cancer Immunol Res *3*, 575–582.

Lánczky, A., Nagy, Á., Bottai, G., Munkácsy, G., Szabó, A., Santarpia, L., and Győrffy, B. (2016). miRpower: a web-tool to validate survival-associated miRNAs utilizing expression data from 2178 breast cancer patients. Breast Cancer Res. Treat. *160*, 439–446.

Lee, K.F., Simon, H., Chen, H., Bates, B., Hung, M.C., and Hauser, C. (1995). Requirement for neuregulin receptor erbB2 in neural and cardiac development. Nature *378*, 394–398.

Lemmon, M.A., and Schlessinger, J. (2010). Cell signaling by receptor tyrosine kinases. Cell *141*, 1117–1134.

Lesurf, R., Aure, M.R., Mørk, H.H., Vitelli, V., Oslo Breast Cancer Research Consortium (OSBREAC), Lundgren, S., Børresen-Dale, A.-L., Kristensen, V., Wärnberg, F., Hallett, M., et al. (2016). Molecular Features of Subtype-Specific Progression from Ductal Carcinoma In Situ to Invasive Breast Cancer. Cell Rep *16*, 1166–1179.

Leyland-Jones, B. (2009). Human epidermal growth factor receptor 2–positive breast cancer and central nervous system metastases. Journal of Clinical Oncology.

Lim, E., Wu, D., Pal, B., Bouras, T., Asselin-Labat, M.-L., Vaillant, F., Yagita, H., Lindeman, G.J., Smyth, G.K., and Visvader, J.E. (2010). Transcriptome analyses of mouse and human mammary cell subpopulations reveal multiple conserved genes and pathways. Breast Cancer Res. *12*, R21.

Lin, N.U., and Winer, E.P. (2007). Brain Metastases: The HER2 Paradigm. Clinical Cancer Research *13*, 1648–1655.

Liu, P., Erez, A., Nagamani, S.C.S., Dhar, S.U., Kołodziejska, K.E., Dharmadhikari, A.V., Cooper, M.L., Wiszniewska, J., Zhang, F., Withers, M.A., et al. (2011). Chromosome Catastrophes Involve Replication Mechanisms Generating Complex Genomic Rearrangements. Cell *146*, 889–903.

Liu, S., Cong, Y., Wang, D., Sun, Y., Deng, L., Liu, Y., Martin-Trevino, R., Shang, L., McDermott, S.P., Landis, M.D., et al. (2014). Breast cancer stem cells transition between epithelial and mesenchymal states reflective of their normal counterparts. Stem Cell Reports *2*, 78–91.

Liu, Y., Kosaka, A., Ikeura, M., Kohanbash, G., Fellows-Mayle, W., Snyder, L.A., and Okada, H. (2013). Premetastatic soil and prevention of breast cancer brain metastasis. Neuro-Oncology *15*, 891–903.

Ljunggren, H.-G., and Malmberg, K.-J. (2007). Prospects for the use of NK cells in immunotherapy of human cancer. Nat. Rev. Immunol. *7*, 329–339.

Love, M.I., Huber, W., and Anders, S. (2014). Moderated estimation of fold change and dispersion for RNA-seq data with DESeq2. Genome Biol. *15*, 550.

Luzzi, K.J., MacDonald, I.C., Schmidt, E.E., Kerkvliet, N., Morris, V.L., Chambers, A.F., and Groom, A.C. (1998). Multistep nature of metastatic inefficiency: dormancy of solitary cells after successful extravasation and limited survival of early micrometastases. The American Journal of Pathology *153*, 865–873.

MacKie, R.M., Reid, R., and Junor, B. (2003). Fatal melanoma transferred in a donated kidney 16 years after melanoma surgery. N. Engl. J. Med. *348*, 567–568.

Maeda, R., Yoshida, J., Ishii, G., Aokage, K., Hishida, T., Nishimura, M., Nishiwaki, Y., and Nagai, K. (2010). Long-term outcome and late recurrence in patients with completely resected stage IA non-small cell lung cancer. J Thorac Oncol *5*, 1246–1250.

Malanchi, I., Santamaria-Martínez, A., Susanto, E., Peng, H., Lehr, H.-A., Delaloye, J.-F., and Huelsken, J. (2011). Interactions between cancer stem cells and their niche govern metastatic colonization. Nature *481*, 85–89.

Martinet, L., and Smyth, M.J. (2015). Balancing natural killer cell activation

through paired receptors. Nature Publishing Group *15*, 243–254.

Massagué, J., and Obenauf, A.C. (2016). Metastatic colonization by circulating tumour cells. Nature *529*, 298–306.

Meng, S., Tripathy, D., Frenkel, E.P., Shete, S., Naftalis, E.Z., Huth, J.F., Beitsch, P.D., Leitch, M., Hoover, S., Euhus, D., et al. (2004). Circulating tumor cells in patients with breast cancer dormancy. Clin. Cancer Res. *10*, 8152–8162.

Meyaard, L. (2008). The inhibitory collagen receptor LAIR-1 (CD305). J. Leukoc. Biol. *83*, 799–803.

Miroshnikova, Y.A., Mouw, J.K., Barnes, J.M., Pickup, M.W., Lakins, J.N., Kim, Y., Lobo, K., Persson, A.I., Reis, G.F., McKnight, T.R., et al. (2016). Tissue mechanics promote IDH1-dependent HIF1α–tenascin C feedback to regulate glioblastoma aggression. Nat Cell Biol *18*, 1336–1345.

Moasser, M.M. (2007). The oncogene HER2: its signaling and transforming functions and its role in human cancer pathogenesis. Oncogene *26*, 6469–6487.

Moody, S.E., Sarkisian, C.J., Hahn, K.T., Gunther, E.J., Pickup, S., Dugan, K.D., Innocent, N., Cardiff, R.D., Schnall, M.D., and Chodosh, L.A. (2002). Conditional activation of Neu in the mammary epithelium of transgenic mice results in reversible pulmonary metastasis. Cancer Cell *2*, 451–461.

Morikawa, A., Peereboom, D.M., and Thorsheim, H.R. (2014). Capecitabine and lapatinib uptake in surgically resected brain metastases from metastatic breast cancer patients: a prospective study. Neuro- ….

Muggerud, A.A., Hallett, M., Johnsen, H., Kleivi, K., Zhou, W., Tahmasebpoor, S., Amini, R.-M., Botling, J., Børresen-Dale, A.-L., Sørlie, T., et al. (2010). Molecular diversity in ductal carcinoma in situ (DCIS) and early invasive breast cancer. Mol Oncol *4*, 357–368.

Muller, W.J., Sinn, E., Pattengale, P.K., Wallace, R., and Leder, P. (1988). Single-step induction of mammary adenocarcinoma in transgenic mice bearing the activated c-neu oncogene. Cell *54*, 105–115.

Naba, A., Clauser, K.R., Hoersch, S., Liu, H., Carr, S.A., and Hynes, R.O. (2012). The matrisome: in silico definition and in vivo characterization by proteomics of normal and tumor extracellular matrices. Mol. Cell Proteomics *11*, M111.014647.

Nguyen, D.X., Chiang, A.C., Zhang, X.H.F., Kim, J.Y., Kris, M.G., Ladanyi, M., Gerald, W.L., and Massagué, J. (2009). WNT/TCF Signaling through LEF1 and HOXB9 Mediates Lung Adenocarcinoma Metastasis. Cell *138*, 51–62.

Noh, S.H., Park, S.R., Yang, H.-K., Chung, H.C., Chung, I.-J., Kim, S.-W., Kim, H.-H., Choi, J.-H., Kim, H.-K., Yu, W., et al. (2014). Adjuvant capecitabine plus

oxaliplatin for gastric cancer after D2 gastrectomy (CLASSIC): 5-year follow-up of an open-label, randomised phase 3 trial. Lancet Oncol. *15*, 1389–1396.

Obenauf, A.C., and Massagué, J. (2015). Surviving at a Distance: Organ-Specific Metastasis. Trends in Cancer *1*, 76–91.

Onitilo, A.A., Engel, J.M., Greenlee, R.T., and Mukesh, B.N. (2009). Breast cancer subtypes based on ER/PR and Her2 expression: comparison of clinicopathologic features and survival. Clin Med Res *7*, 4–13.

Oskarsson, T., Acharyya, S., Zhang, X.H.F., Vanharanta, S., Tavazoie, S.F., Morris, P.G., Downey, R.J., Manova-Todorova, K., Brogi, E., and eacute, J.M. (2011). Breast cancer cells produce tenascin C as a metastatic niche component to colonize the lungs. Nature Medicine *17*, 867–874.

Oskarsson, T., Batlle, E., and Massagué, J. (2014). Metastatic Stem Cells: Sources, Niches, and Vital Pathways. Stem Cell 1–16.

Pagliarini, R., Shao, W., and Sellers, W.R. (2015). Oncogene addiction: pathways of therapeutic response, resistance, and road maps toward a cure. EMBO Rep. *16*, 280–296.

Perou, C.M., Sørlie, T., Eisen, M.B., van de Rijn, M., Jeffrey, S.S., Rees, C.A., Pollack, J.R., Ross, D.T., Johnsen, H., and Akslen, L.A. (2000). Molecular portraits of human breast tumours. Nature *406*, 747–752.

Peters, S., and Zimmermann, S. (2014). Targeted therapy in NSCLC driven by HER2 insertions. Transl Lung Cancer Res *3*, 84–88.

Pickup, M.W., Mouw, J.K., and Weaver, V.M. (2014). The extracellular matrix modulates the hallmarks of cancer. EMBO Rep. *15*, 1243–1253.

Polleux, F., and Ghosh, A. (2002). The slice overlay assay: a versatile tool to study the influence of extracellular signals on neuronal development. Sci. STKE *2002*, pl9–pl9.

Ponomarev, V., Doubrovin, M., Serganova, I., Vider, J., Shavrin, A., Beresten, T., Ivanova, A., Ageyeva, L., Tourkova, V., Balatoni, J., et al. (2004). A novel triple-modality reporter gene for whole-body fluorescent, bioluminescent, and nuclear noninvasive imaging. Eur. J. Nucl. Med. Mol. Imaging *31*, 740–751.

Quail, D.F., and Joyce, J.A. (2017). The Microenvironmental Landscape of Brain Tumors. Cancer Cell *31*, 326–341.

Roskoski, R. (2014). The ErbB/HER family of protein-tyrosine kinases and cancer. Pharmacol. Res. *79*, 34–74.

Schreiber, R.D., Old, L.J., and Smyth, M.J. (2011). Cancer Immunoediting:

Integrating Immunity's Roles in Cancer Suppression and Promotion. Science *331*, 1565–1570.

Sevenich, L., Bowman, R.L., Mason, S.D., Quail, D.F., Rapaport, F., Elie, B.T., Brogi, E., Brastianos, P.K., Hahn, W.C., Holsinger, L.J., et al. (2014). Analysis of tumour- and stroma-supplied proteolytic networks reveals a brain-metastasis-promoting role for cathepsin S. Nat Cell Biol *16*, 876–888.

Shibue, T., Brooks, M.W., Inan, M.F., Reinhardt, F., and Weinberg, R.A. (2012). The outgrowth of micrometastases is enabled by the formation of filopodium-like protrusions. Cancer Discovery *2*, 706–721.

Shultz, L.D., Lyons, B.L., Burzenski, L.M., Gott, B., Chen, X., Chaleff, S., Kotb, M., Gillies, S.D., King, M., Mangada, J., et al. (2005). Human lymphoid and myeloid cell development in NOD/LtSz-scid IL2R gamma null mice engrafted with mobilized human hemopoietic stem cells. J. Immunol. *174*, 6477–6489.

Siegel, R.L., Miller, K.D., and Jemal, A. (2016). Cancer statistics, 2016. CA: a Cancer Journal for Clinicians *66*, 7–30.

Siegel, R.L., Miller, K.D., and Jemal, A. (2017). Cancer Statistics, 2017. CA: a Cancer Journal for Clinicians *67*, 7–30.

Slamon, D.J., Leyland-Jones, B., Shak, S., Fuchs, H., Paton, V., Bajamonde, A., Fleming, T., Eiermann, W., Wolter, J., and Pegram, M. (2001). Use of chemotherapy plus a monoclonal antibody against HER2 for metastatic breast cancer that overexpresses HER2. N Engl J Med *344*, 783–792.

Slamon, D., Eiermann, W., Robert, N., Pienkowski, T., Martín, M., Press, M., Mackey, J., Glaspy, J., Chan, A., Pawlicki, M., et al. (2011). Adjuvant trastuzumab in HER2-positive breast cancer. N. Engl. J. Med. *365*, 1273–1283.

Sosa, M.S., Bragado, P., and Aguirre-Ghiso, J.A. (2014). Mechanisms of disseminated cancer cell dormancy: an awakening field. Nature Publishing Group *14*, 611–622.

Sun, J.C., and Lanier, L.L. (2008). Cutting edge: viral infection breaks NK cell tolerance to "missing self". The Journal of Immunology *181*, 7453–7457.

Swain, S.M., Baselga, J., Kim, S.-B., Ro, J., Semiglazov, V., Campone, M., Ciruelos, E., Ferrero, J.-M., Schneeweiss, A., Heeson, S., et al. (2015). Pertuzumab, trastuzumab, and docetaxel in HER2-positive metastatic breast cancer. N. Engl. J. Med. *372*, 724–734.

Sørlie, T. (2004). Molecular portraits of breast cancer: tumour subtypes as distinct disease entities. European Journal of Cancer *40*, 2667–2675.

Tadashi Yamamoto, M.S.K.K.A.D.A.M.S.T.T.A.M.O., and Semba, K. (2011).

ErbB2/HER2: Its Contribution to Basic Cancer Biology and the Development of Molecular Targeted Therapy. In Breast Cancer - Carcinogenesis, Cell Growth and Signalling Pathways, (InTech).

Takeda, K., Smyth, M.J., Cretney, E., Hayakawa, Y., Yamaguchi, N., Yagita, H., and Okumura, K. (2001). Involvement of tumor necrosis factor-related apoptosis-inducing ligand in NK cell-mediated and IFN-gamma-dependent suppression of subcutaneous tumor growth. Cell. Immunol. *214*, 194–200.

Tammela, T., Sanchez-Rivera, F.J., Cetinbas, N.M., Wu, K., Joshi, N.S., Helenius, K., Park, Y., Azimi, R., Kerper, N.R., Wesselhoeft, R.A., et al. (2017). A Wnt-producing niche drives proliferative potential and progression in lung adenocarcinoma. Nature *545*, 355–359.

Taskar, K.S., Rudraraju, V., Mittapalli, R.K., Samala, R., Thorsheim, H.R., Lockman, J., Gril, B., Hua, E., Palmieri, D., Polli, J.W., et al. (2011). Lapatinib Distribution in HER2 Overexpressing Experimental Brain Metastases of Breast Cancer. Pharm Res *29*, 770–781.

Valiente, M., Obenauf, A.C., Jin, X., Chen, Q., Zhang, X.H.F., Lee, D.J., Chaft, J.E., Kris, M.G., Huse, J.T., Brogi, E., et al. (2014). Serpins Promote Cancer Cell Survival and Vascular Co-Option in Brain Metastasis. Cell *156*, 1002–1016.

Vert, J.-P., Foveau, N., Lajaunie, C., and Vandenbrouck, Y. (2006). An accurate and interpretable model for siRNA efficacy prediction. BMC Bioinformatics *7*, 520.

Vesely, M.D., Kershaw, M.H., Schreiber, R.D., and Smyth, M.J. (2011). Natural innate and adaptive immunity to cancer. Annu. Rev. Immunol. *29*, 235–271.

Villegas, F.R., Coca, S., Villarrubia, V.G., Jiménez, R., Chillón, M.J., Jareño, J., Zuil, M., and Callol, L. (2002). Prognostic significance of tumor infiltrating natural killer cells subset CD57 in patients with squamous cell lung cancer. Lung Cancer *35*, 23–28.

Walker, D.G., and Lue, L.-F. (2015). Immune phenotypes of microglia in human neurodegenerative disease: challenges to detecting microglial polarization in human brains. Alzheimers Res Ther *7*, 56.

Wallasch, C., Weiss, F.U., Niederfellner, G., Jallal, B., Issing, W., and Ullrich, A. (1995). Heregulin-dependent regulation of HER2/neu oncogenic signaling by heterodimerization with HER3. Embo J. *14*, 4267–4275.

Wieduwilt, M.J., and Moasser, M.M. (2008). The epidermal growth factor receptor family: biology driving targeted therapeutics. Cell. Mol. Life Sci. *65*, 1566–1584.

Wilson, K.J., Gilmore, J.L., Foley, J., Lemmon, M.A., and Riese, D.J. (2009). Functional selectivity of EGF family peptide growth factors: implications for

cancer. Pharmacol. Ther. *122*, 1–8.

Winslow, M.M., Dayton, T.L., Verhaak, R.G.W., Kim-Kiselak, C., Snyder, E.L., Feldser, D.M., Hubbard, D.D., DuPage, M.J., Whittaker, C.A., Hoersch, S., et al. (2011). Suppression of lung adenocarcinoma progression by Nkx2-1. Nature *473*, 101–104.

Wu, J., and Lanier, L.L. (2003). Natural killer cells and cancer. Adv. Cancer Res. *90*, 127–156.

Xiao, D., Craig, J.C., Chapman, J.R., Dominguez-Gil, B., Tong, A., and Wong, G. (2013). Donor cancer transmission in kidney transplantation: a systematic review. Am. J. Transplant. *13*, 2645–2652.

Yarden, Y., and Sliwkowski, M.X. (2001). Untangling the ErbB signalling network. Nat Rev Mol Cell Biol *2*, 127–137.

Yarden, Y., and Pines, G. (2012). The ERBB network: at last, cancer therapy meets systems biology. Nature Publishing Group *12*, 553–563.

Yrjänheikki, J., Keinänen, R., Pellikka, M., Hökfelt, T., and Koistinaho, J. (1998). Tetracyclines inhibit microglial activation and are neuroprotective in global brain ischemia. Proc. Natl. Acad. Sci. U.S.a. *95*, 15769–15774.

Zhang, X.H.F., Jin, X., Malladi, S., Zou, Y., Wen, Y.H., Brogi, E., Smid, M., Foekens, J.A., and Massagué, J. (2013). Selection of bone metastasis seeds by mesenchymal signals in the primary tumor stroma. Cell *154*, 1060–1073.